

***Thermal Modeling of the TN-32B
Cask for the High Burnup Spent
Fuel Data Project***

Spent Fuel and Waste Disposition

***Prepared for
U.S. Department of Energy
Spent Fuel and Waste Science and
Technology***

***JA Fort
DJ Richmond
JM Cuta
SR Suffield***

July 30, 2019

PNNL-28915

DISCLAIMER

This information was prepared as an account of work sponsored by an agency of the U.S. Government. Neither the U.S. Government nor any agency thereof, nor any of their employees, makes any warranty, expressed or implied, or assumes any legal liability or responsibility for the accuracy, completeness, or usefulness, of any information, apparatus, product, or process disclosed, or represents that its use would not infringe privately owned rights. References herein to any specific commercial product, process, or service by trade name, trade mark, manufacturer, or otherwise, does not necessarily constitute or imply its endorsement, recommendation, or favoring by the U.S. Government or any agency thereof. The views and opinions of authors expressed herein do not necessarily state or reflect those of the U.S. Government or any agency thereof.

SUMMARY

This report describes thermal modeling done for the High Burnup Spent Fuel Data Project that is being performed by the U.S. Department of Energy's Spent Fuel and Waste Science and Technology (SFWST) research and development (R&D) program. The purpose of this project is to investigate the performance of high-burnup spent nuclear fuel in dry storage. Part of this project is a demonstration test being performed with a storage module in the North Anna Nuclear Power Station's Independent Spent Fuel Storage Installation (ISFSI). The storage module selected for this demonstration is an Orano TN-32B High Burnup cask (Figure S-1) which has been loaded with fuel assemblies from the North Anna spent fuel pool. The main goals of this test are to provide confirmatory data for model validation and potential improvement, support license renewals and new licenses for ISFSIs, and support transportation licensing for high burnup spent nuclear fuel (EPRI 2014).

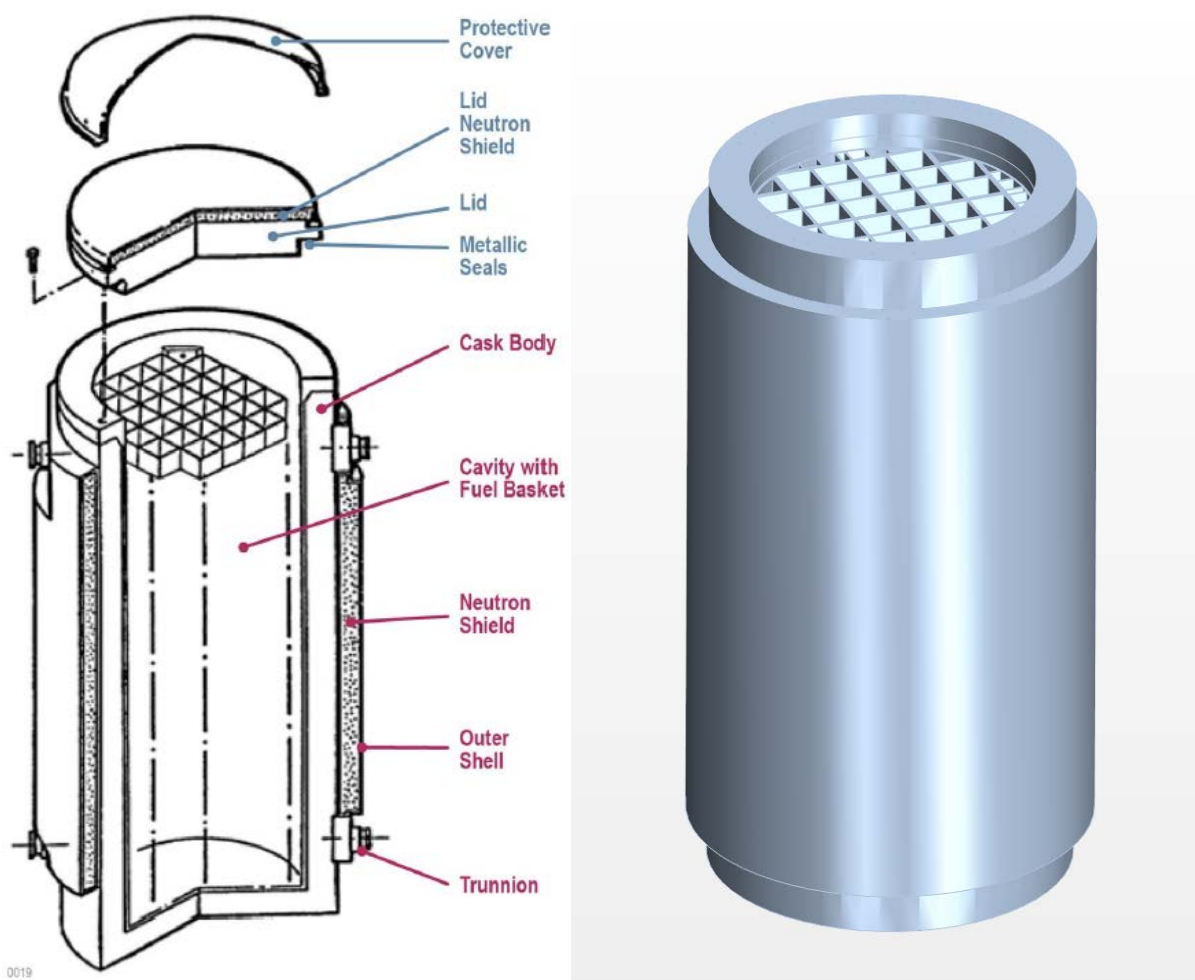


Figure S-1. Diagram and geometry model^a for Orano TN-32B dry storage cask.

^a In the diagram, support rails between the fuel basket and cask inner wall are omitted for clarity. The protective cover, lid neutron shield, and the cask lid are shown removed from the geometry model; support rails are visible in this image.

July 30, 2019

The TN-32B cask was modified for this demonstration test by installing thermocouple lances in single control rod positions in seven of the fuel assemblies (Figure S-2). While this did not allow direct measurement of the fuel cladding temperature, the selected control rod position near the center of the fuel assembly provides a good estimate of the peak fuel cladding temperature at that axial position of the thermocouple. A total of nine thermocouples in each lance provides a distribution of fuel temperatures over the active length of the fuel rods.

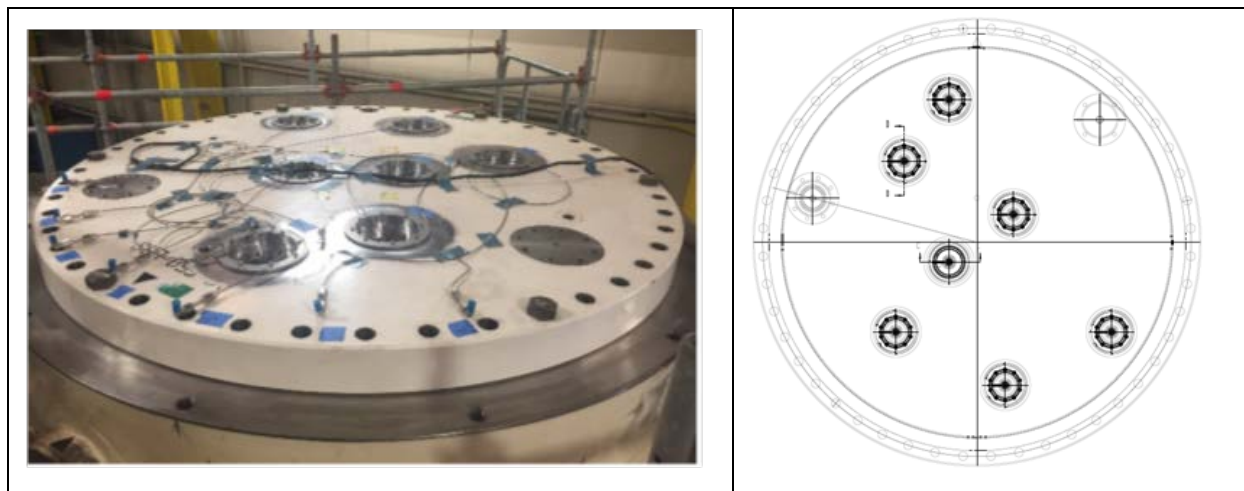


Figure S-2. Thermocouple lance locations^b in TN-32B lid – the drain and vent ports are also visible.

The plan for the Demonstration test was to begin dry storage with a loading of high-burnup fuel that would produce fuel temperatures as close as possible to the allowable peak cladding temperature (PCT) regulatory guidance limit of 400°C (752°F), as specified in Interim Staff Guidance 11, Revision 3 (NRC 2003) and the Standard Review Plan, Revision 1 (NRC 2010), without exceeding temperature limits in other cask components. Reaching this temperature range was important to investigate effects of hydride orientation in the fuel cladding. However, this fuel temperature goal was not possible in the demonstration cask because the planned loading was limited by temperatures of the lid neutron shield.

The loading date used for planning and associated estimates of peak fuel temperature was July of 2017. The actual loading of the demonstration cask was completed on November 15, 2017 and the cask was kept in the fuel handling building at North Anna for a period of two weeks for monitoring tests and to reach an equilibrium temperature. Measured temperatures during this “thermal soak” were the basis for comparison with “blind” model predictions by Pacific Northwest National Laboratory (PNNL), which are described in this report, and by other modeling teams^c.

The measured fuel temperatures were low compared to the PCT limit of 400°C (752°F), but this was expected due to the limited total decay heat. However, measured values were below the model predictions by an unexpected amount. Model input sensitivity tests described in this report explain the cause of these differences. While fuel temperatures are well below initial goals of the project, the demonstration is proving beneficial for model validation and for helping to illuminate the modest level of fuel temperatures under current utility loading practice.

^b Specific thermocouple lance locations are shown in App. B, Figure B-8. Axial position of thermocouples are shown in Figure B-9 and tabulated with elevations in Table B-2.

^c A report is in preparation at the Electric Power Research Institute (EPRI) that will present results of this “Round Robin” modeling exercise.

The demonstration cask was moved to the North Anna ISFSI on November 31, 2017 and will be monitored for a 10-year storage period. Fuel removal and inspection at the end of this storage period is planned.

SFWST tasked PNNL with performing thermal analyses^d in support of the Demonstration project for two purposes:

1. To help the project team assess proposed loading patterns with respect to obtaining desired material's performance data, specifically for PCTs near 400°C for multiple cladding types, and
2. To obtain "best estimate" temperatures, especially for the cladding, for use in the storage and transportation programs performed by the SFWST.

This report is a comprehensive description of PNNL's thermal modeling in support of this project. It presents the evolution of inputs and model predictions from test planning through loading of the cask. Initial models provided fuel cladding temperature estimates for the planned loading of fuel assemblies. These models were based on cask geometry from the storage system safety analysis, publicly available fuel data, and conservative decay heat estimates provided by the utility. The models were then updated with best estimate decay heat values for the fuel assemblies and fuel geometry provided under separate Non-Disclosure Agreements (NDAs) with the fuel vendors, cask manufacturer, and site operator (Dominion). Finally, the cask models were adapted to reflect conditions following loading with the fuel assemblies to provide comparisons of blind model predictions of steady state fuel temperatures against the thermocouple measurements made after reaching thermal equilibrium during the two-week thermal soak. Sensitivity analyses are included for model input parameters to explain differences between the blind predictions and measurements.

Simulation results are presented for relevant points in the planning and execution of the Demonstration test:

- Assembly load planning
- Pre-loading estimates of fuel temperatures
- Blind test predictions
- Post-loading sensitivity runs.

Two different models were developed for the TN-32B cask, one using COBRA-SFS and the second using STAR-CCM+. Table S-1 summarizes the evolution in models, inputs, and estimates of PCTs over the course of this project. The models have changed only slightly, but the inputs have reflected improved accuracy in representing the actual system. The principal change in model inputs is the decay heat estimates for each assembly. Initial values were conservative estimates provided by Dominion. Subsequent best estimate decay heats from Oak Ridge National Laboratory (ORNL) were much lower. The final column in Table S-1 is for fuel temperature measurements obtained after the initial loading and a two-week thermal soak. The ambient temperature for the test is lower than the value used in the earlier estimates, but only by 14 °C. The difference in predicted peak fuel temperature between the test and the previous storage model prediction (271 - 259 = 12 °C) is, in part, due to the configuration of the cask in the decontamination pit and is nearly equal to the ambient temperature change. However, as shown in this table, the measured maximum temperature was far below this model prediction. Note that the thermocouple lance does not provide the peak fuel temperature for that hottest assembly, but based on COBRA-SFS model estimates, it is within 2 °C of the PCT.

^d This analysis supports the SFWST R&D program. Independent thermal analyses by Dominion and Orano were used in the License Amendment Request for the demonstration cask.

Table S-1. Changing decay heat estimates and associated peak fuel temperature predictions.

Model Date	Ambient, °C (°F)	Decay heat, kW	Predicted PCT with COBRA- SFS, °C	Estimated PCT from TC Measurement, °C
9/15	37.8 (100)	36.8 ^a	315	-
9/16	37.8 (100)	30.6 ^b	271	-
12/17	23.9 (75)	30.4 ^c	259	229

^a Utility estimate for planned July 2017 loading date.

^b ORIGEN calculation for planned July 2017 loading date.

^c ORIGEN calculation for actual November 2017 loading date.

Figure S-3 shows the unexpectedly large conservatism of the best estimate models in blind predictions of temperatures measured at thermocouple locations. With this difference between predictions and measured temperatures, sensitivity studies identified the most likely cause as an inappropriately specified gap resistance between the basket and rails. The Updated Final Safety Analysis Report (UFSAR) gave a gap distance defined as in thermal equilibrium, but as-built drawings showed that this value was more likely correct for assembled conditions and at thermal equilibrium it would be much smaller. Figure S-4 shows COBRA-SFS simulation results with this gap thickness reduced to a more realistic value, based on the drawings.

The continuous stream of thermocouple data from the TN-32B fuel assemblies has been extremely beneficial. It has opened new insight into thermal behavior in the cask and has allowed refinement of model accuracy, which can then be used to more confidently predict other situations for this cask and related spent fuel storage systems.

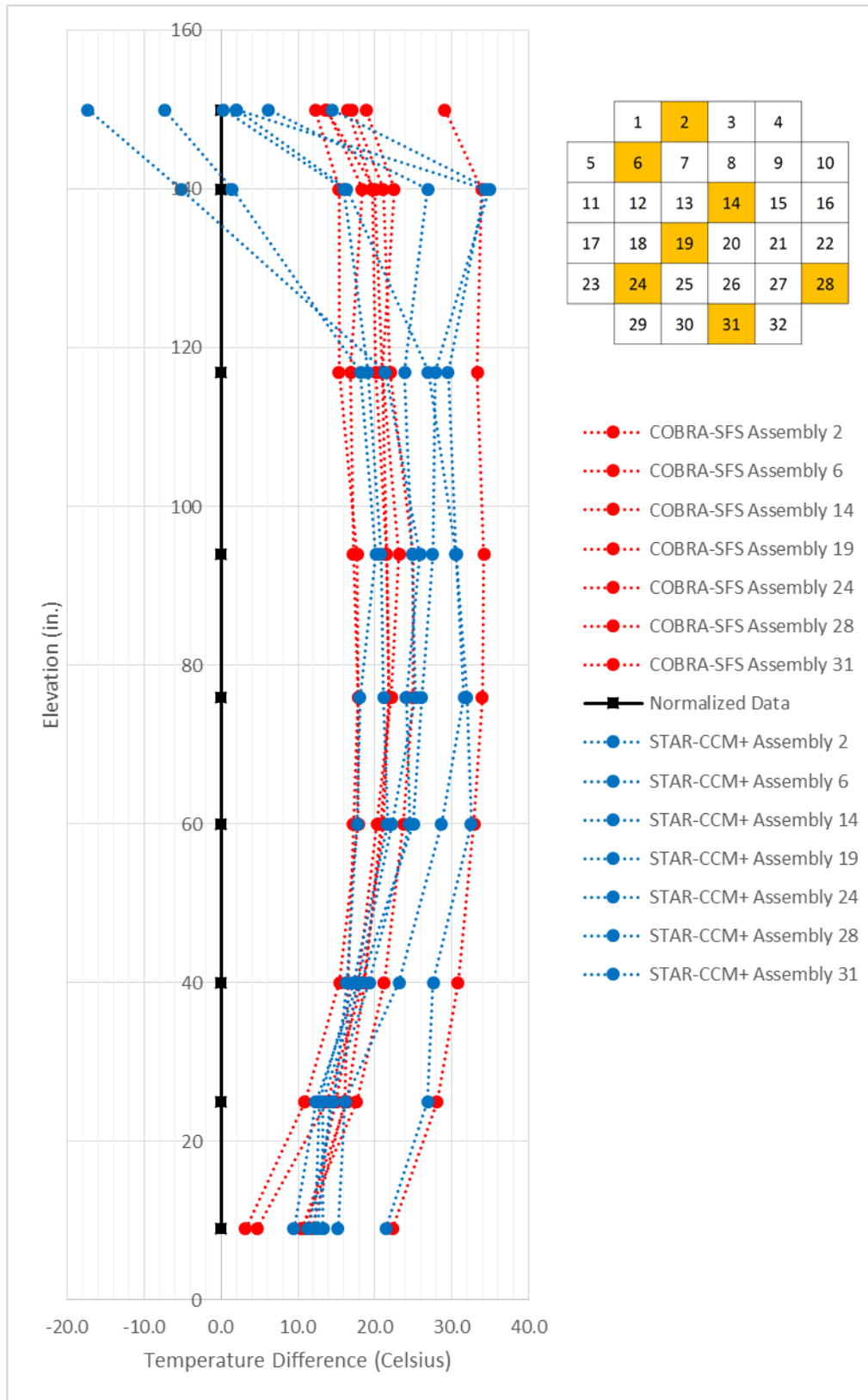


Figure S-3. Comparison of measurements with blind predictions at thermocouple locations.

July 30, 2019

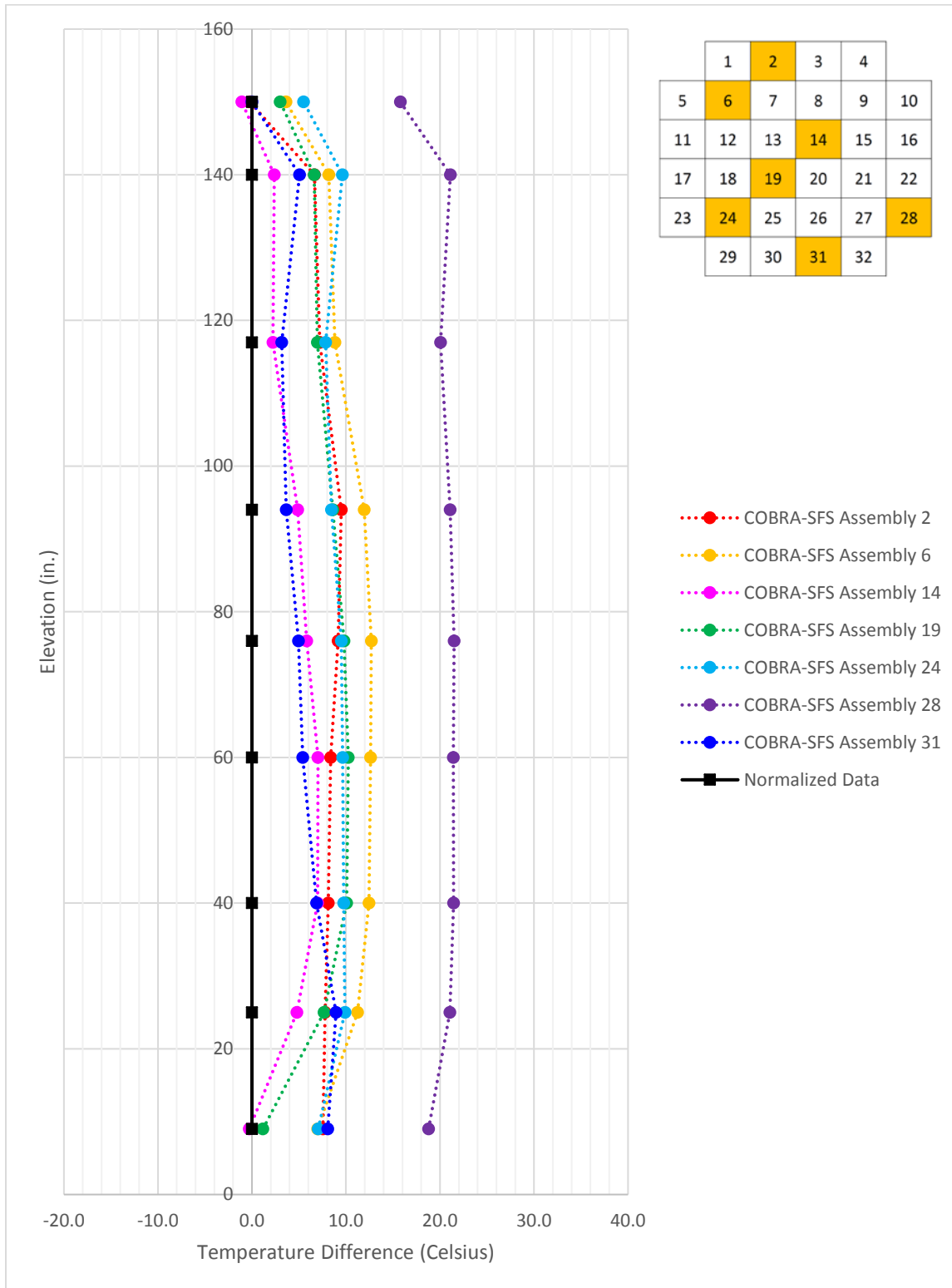


Figure S-4. Comparison of measurements with adjusted predictions at thermocouple locations.

ACKNOWLEDGEMENTS

PNNL wishes to thank EPRI for coordinating the High Burnup Demonstration at North Anna, and in particular Keith Waldrop. We thank the Demonstration team of Dominion Energy, Orano Federal Services (formerly AREVA Federal Services), Orano TN (formerly AREVA TN), Framatome (previously AREVA), and Westinghouse Fuels, for the input and data received. ORNL calculated the decay heats for the final loading cases. Their contribution to this work was significant and is appreciated.

Finally, the authors would like to thank Colleen Winters and Susan Tackett, for helping us achieve a clear and concise presentation of our work through multiple revisions of this report.

This page is intentionally left blank.

CONTENTS

SUMMARY	iii
ACKNOWLEDGEMENTS	ix
ACRONYMS	xix
1. INTRODUCTION	1
2. PRELIMINARY MODELING IN SUPPORT OF PRE-TEST PLANNING	5
2.1 COBRA-SFS Model Description	5
2.1.1 Representation of TN-32B Cask for COBRA-SFS	5
2.1.2 Representation of Fuel Assemblies and Internal Convection in COBRA-SFS Model of TN-32B	11
2.1.3 Boundary Conditions	14
2.2 STAR-CCM+ Model Description	14
2.2.1 Cask Geometry	15
2.2.2 Computational Mesh	17
2.2.3 Material Properties	19
2.2.4 Fuel Effective Conductivity	19
2.2.5 External Boundaries	20
2.2.5.1 Concrete Base	21
2.2.5.2 External Convection Boundaries	21
2.2.6 Thermal Gap Resistances	21
2.2.7 Thermal Radiation Model	22
2.2.8 Fluid Models	22
2.3 Fuel Loading Map, Decay Heats and Axial Power Profile	22
2.4 COBRA-SFS Results	26
2.4.1 Initial Storage	27
2.4.2 Vacuum Drying Conditions	30
2.4.3 Storage Conditions after 10 Years	31
2.4.4 Recirculation within the TN-32B Basket	32
2.4.5 Summary of Clad Temperature Distribution	33
2.5 STAR-CCM+ Results	36
2.5.1 Initial Storage	36
2.5.2 Sensitivity of Results to Solar Heat Loading	37
3. BEST ESTIMATE UPDATES TO PLANNING MODELS	39
3.1 Fuel Assembly Geometry and Decay Heats	39
3.2 Axial Decay Heat Distribution	41
3.3 Additional Model Updates	43
3.4 COBRA-SFS Thermal Modeling Results	44
3.4.1 Initial Storage Conditions	44
3.4.2 Axial Temperature Profiles for Option 1 Thermocouple Locations	47
3.4.3 Vacuum Drying Conditions	50
3.4.4 Storage Conditions after 10 Years	53

3.4.5	Summary of Clad Temperature Distribution.....	53
3.4.6	Effect of Changes in Input and Boundary Conditions	55
3.5	Model Results: STAR-CCM+.....	57
3.5.1	STAR-CCM+ Results for Initial Storage Conditions	57
3.5.2	Effect of Changes in Input and Boundary Conditions	63
4.	PRE-LOADING TEMPERATURE ESTIMATES	65
5.	ROUND ROBIN MODELING OF THE CASK LOADING.....	67
5.1	Model Descriptions	67
5.1.1	COBRA-SFS Model	67
5.1.1.1	Geometry.....	68
5.1.1.2	Boundary Conditions	69
5.1.2	STAR-CCM+ Model	69
5.1.2.1	Geometry.....	70
5.1.2.2	Boundary Conditions	70
5.1.2.3	Gap Resistances	70
5.1.2.4	Fuel Region.....	71
5.1.2.5	Mesh.....	71
5.2	Blind Predictions of Temperature at End of Two-Week Thermal Soak	72
5.2.1	Blind Modeling Results Using Convective Correlations as Boundary Conditions	72
5.2.2	Blind Model Results Using Measured Surface Temperature as Boundary Conditions	79
5.3	Non-Blind Sensitivity Runs	85
5.4	Adjusted Best Estimate Case	88
6.	CONCLUSIONS AND RECOMMENDATIONS	91
6.1	Conclusions	91
6.2	Recommendations	91
7.	REFERENCES	93
Appendix A	A-1
Appendix B	B-1

LIST OF FIGURES

Figure S-1. Diagram and geometry model for Orano TN-32B dry storage cask.	iii
Figure S-2. Thermocouple lance locations in TN-32B lid – the drain and vent ports are also visible.....	iv
Figure S-3. Comparison of measurements with blind predictions at thermocouple locations.....	vii
Figure S-4. Comparison of measurements with adjusted predictions at thermocouple locations.....	viii
Figure 1-1. Diagram and geometry model for Orano TN-32B dry storage cask.	2
Figure 2-1. COBRA-SFS model regions for the TN-32B cask (NOTE: model image not to scale).	7
Figure 2-2. Diagram of 3-D COBRA-SFS model of TN-32B basket – rails in purple, fuel compartments in blue, and aluminum structures in grey (NOTE: diagram not to scale; node thicknesses greatly exaggerated for clarity).....	8
Figure 2-3. Diagram of 3-D COBRA-SFS model of TN-32B cask cross-section illustrating nodalization of cask body, neutron shield, and exterior surface (NOTE: diagram not to scale; node thicknesses greatly exaggerated for clarity).....	9
Figure 2-4. Rod-and-subchannel array diagram for COBRA-SFS model of 17×17 fuel assembly within basket cells of TN-32B (NOTE: diagram is not to scale).....	12
Figure 2-5. Laminar and turbulent formulations for Nusselt number.	13
Figure 2-6. External view of TN-32B model CAD geometry.	15
Figure 2-7. Axial cross-section of TN-32B model geometry.	16
Figure 2-8. Axial cross-section of upper half of TN-32B model geometry.....	16
Figure 2-9. Radial cross-section of TN-32B model geometry.	17
Figure 2-10. Planar slice through axial centerline showing volume mesh of the STAR-CCM+ model.	18
Figure 2-11. Planar slice through mid-line showing volume mesh of the STAR-CCM+ model – fuel regions, basket, liners, and rails highlighted.	19
Figure 2-12. PNNL developed transverse thermal conductivity used in STAR-CCM+ model.....	20
Figure 2-13. Final loading map proposed for Demonstration project (with assembly decay heat estimates provided by Dominion for 7/1/17 and 1/1/27). Note that M5® and ZIRLO® are registered trademarks.	24
Figure 2-14. Bounding low-burnup axial decay heat profile from DOE/RW-0472 compared to preliminary axial burnup profile data obtained for one candidate fuel assembly in the Demonstration project.	26
Figure 2-15. Assembly PCTs (°C) estimated with COBRA-SFS for conservative decay heats and initial storage conditions (total decay heat load 36.8 kW, as of 7/1/2017).....	27
Figure 2-16. Assembly minimum cladding temperatures (°C) estimated with COBRA-SFS for conservative decay heats and initial storage conditions (total decay heat load 36.8 kW, as of 7/1/2017).....	27
Figure 2-17. Radial distribution of system component temperatures at the axial location of PCT for initial storage conditions (conservative decay heats, as of July 2017).....	28

Figure 2-18. Axial distribution of temperature on hottest and coolest rods in the hottest assembly (57A) for initial storage conditions (conservative decay heats, as of July 2017).....	29
Figure 2-19. Axial temperature distributions on main components of TN-32B cask for initial storage conditions (conservative decay heats, as of July 2017).....	30
Figure 2-20. PCT as a function of time, calculated with COBRA-SFS model for bounding vacuum drying transient (conservative decay heats, as of July 2017).....	31
Figure 2-21. Assembly PCTs (°C) estimated using conservative decay heats at end of 10 years in storage (with F52, as of January 2027).....	32
Figure 2-22. Assembly minimum cladding temperatures (°C) estimated using conservative decay heats at end of 10 years in storage (with F52, as of January 2027).....	32
Figure 2-23. Helium gas velocities in TN-32B basket for initial storage conditions, predicted with COBRA-SFS model using rod-and-subchannel representation of fuel assemblies (based on 36.8 kW total decay heat load, as of 7/1/2017).....	33
Figure 2-24. Temperature distribution ranges in the hottest assembly (57a in cell #14), from cladding temperatures predicted with COBRA-SFS model for conservative decay heats and initial loading conditions (as of 7/1/2017)	34
Figure 2-25. Temperature distribution ranges in the hottest assembly (57a in cell #14) after 10 years (1/1/2027), from cladding temperatures predicted with COBRA-SFS model using conservative decay heats.....	35
Figure 2-26. Temperature distribution ranges for all fuel assemblies in the TN-32B basket, from cladding temperatures predicted with COBRA-SFS model for initial loading conditions (with F40, as of 7/1/2017).	36
Figure 2-27. Assembly PCTs (°C) estimated with STAR-CCM+ for conservative decay heats and initial storage conditions (total decay heat load 36.8 kW, as of 7/1/2017).....	37
Figure 3-1. Final loading map proposed for Demonstration project.....	40
Figure 3-2. Axial decay heat profiles per assembly, from detailed pin-by-pin decay heat calculations, compared to bounding low-burnup axial decay heat profile from DOE/RW-0472.	42
Figure 3-3. Maximum, minimum, and average axial decay heat profiles per assembly, from detailed pin-by-pin decay heat calculations.....	43
Figure 3-4. Assembly PCT (°C) estimated for initial storage conditions (as of 7/31/2017).....	44
Figure 3-5. Assembly minimum cladding temperatures (°C) estimated for initial storage conditions (as of 7/31/2017).....	44
Figure 3-6. Radial distribution of system component temperatures at the axial location of PCT for initial storage conditions (as of 7/31/2017).....	45
Figure 3-7. Axial distribution of temperature on hottest and coolest rods in the hottest assembly (57A) for initial storage conditions (as of 7/31/2017).....	46
Figure 3-8. Axial temperature distributions on main components of TN-32B cask for initial storage conditions (as of 7/31/2017).....	47
Figure 3-9. Proposed TC lance insertion locations for instrumented assemblies in the cask (Option 1 was adopted for demonstration test).....	48

Figure 3-10. Axial temperature distribution on guide tube rod at proposed Option 1 locations for instrumented assemblies in the cask, predicted with COBRA-SFS model for initial loading conditions (decay heat as of 7/31/2017).	49
Figure 3-11. Axial temperature distribution on hottest rod in each instrumented assembly in the cask, predicted with COBRA-SFS model for initial loading conditions (decay heat as of 7/31/2017).	50
Figure 3-12. PCT as a function of time, calculated with COBRA-SFS model for bounding vacuum drying transient (30.6 kW decay heat total, as of 7/31/2017).	51
Figure 3-13. Estimated PCT as a function of time for extended transient in decontamination pit after helium backfill (30.6 kW decay heat total, as of 7/31/2017).	52
Figure 3-14. Assembly PCTs (°C) estimated for end of 10 years in storage (as of 1/1/2027).	53
Figure 3-15. Assembly minimum cladding temperatures (°C) estimated for end of 10 years in storage (as of 1/1/2027).	53
Figure 3-16. Temperature distribution ranges for all 32 assemblies in the cask, from cladding temperatures predicted with COBRA-SFS model for initial loading conditions (as of 7/31/2017).	54
Figure 3-17. Temperature distribution ranges in the hottest assembly (#14) at initial loading (7/31/2017) and after 10 years (1/1/2027), for cladding temperatures predicted with COBRA-SFS model.	55
Figure 3-18. Transient PCT calculated with COBRA-SFS for 30.6 kW total decay heat compared to preliminary result with conservative (36.8 kW) total decay heat.	57
Figure 3-19. Assembly PCTs (°C) estimated with STAR-CCM+ for initial storage conditions (as of 7/31/2017).	57
Figure 3-20. Differences (STAR-CCM+ minus COBRA-SFS) between model estimates of assembly PCTs (°C) for initial storage conditions (as of 7/31/2017).	58
Figure 3-21. Axial section view of component temperatures.	59
Figure 3-22. Radial section view of component temperatures at level of PCT.	59
Figure 3-23. Temperature distribution on external surfaces of the cask.	60
Figure 3-24. Axial section view showing vertical component of gas velocities.	61
Figure 3-25. Radial section view showing vertical component of backfill gas velocity.	62
Figure 3-26. Velocity magnitude of fill gas at level of drain holes at bottom of basket.	62
Figure 5-1. Updated loading map for November 2017 loading.	68
Figure 5-2. Air temperature in the decontamination pit (ambient TC) and above the work platform (logger 1 & 2 TC).	69
Figure 5-3. Estimated peak fuel cladding estimates – Convective Boundary Condition.	73
Figure 5-4. Cask surface measurement locations.	77
Figure 5-5. Normalized surface temperature predictions relative to measured data.	79
Figure 5-6. Estimated peak fuel cladding temperatures – measured temperature boundary condition.	80

Figure 5-7. Normalized comparisons of temperatures at all thermocouple locations.....	83
Figure 5-8. Normalized comparisons of temperatures at central thermocouple locations (40-117 in.).....	84
Figure 5-9. Gas vertical velocity across basket at axial level of maximum fuel temperature.....	85
Figure 5-10. Adjusted best estimate results for thermocouple locations from COBRA-SFS model.	89
Figure 5-11. Adjusted best estimate peak cladding temperatures from COBRA-SFS model.	90
Figure 5-12. Adjusted best estimate cladding surface temperature distribution from COBRA-SFS model.....	90
Figure A-1. Location of thermocouple lance penetrations. Note drain port, upper right, and vent port, middle left, are visible.....	A-5
Figure A-2. Schematic of a Westinghouse 17×17 fuel bundle (PNL-2575).....	A-6
Figure A-3. Loading map.....	A-7
Figure A-4. Sister rods removed from Assembly 30A (in red, guide/instrument tubes in black). Rods replaced with stainless-steel rods.	A-8
Figure A-5. Sister rods removed from Assembly 5K7 (in red, guide/instrument tubes in black). Rods replaced with stainless-steel rods.	A-8
Figure A-6. Average of all 32 assembly normalized decay heats with 1 on the x axis near the bottom of the fuel rod and 32 being near the top of the fuel rod.	A-9
Figure A-7. Location of poison rod assemblies inserted into guide tubes in cells 8, 13, 15, 18, 20, and 23.	A-10
Figure A-8. Location of thermocouple lances (colored triangle) in guide tube.	A-11
Figure A-9. Axial location of thermocouples in each lance (note that distance is from bottom of the lower nozzle, i.e., from the inner side of the cask bottom).....	A-12
Figure A-10. Temporary neutron shield ring prior to placement around cask. Note also the large roll-up door leading outside to transfer cask out to pad. The cask and work platform level are behind the camera.	A-13
Figure A-11. Looking down on cask to see work platform in place.....	A-14
Figure A-12. Looking from below up to work platform.	A-15
Figure A-13. View of cask in decon pit.	A-16
Figure A-14. View of cask in decon pit.	A-16
Figure A-15. View of cask on leveling pad.	A-17
Figure A-16. View of cask on leveling pad.	A-17
Figure A-17. Dimensions from cask to walls above the work platform.	A-18
Figure A-18. Approximate dimensions below the work platform.	A-18
Figure A-19. Ambient temperature in the decontamination pit.	A-19
Figure A-20. Location of cask wall IR measurements.....	A-21

Figure A-21. Lead blankets and temporary neutron shield ring in place.	A-22
Figure A-22. Dimensions of lead blanket.	A-23
Figure B-1. Basket cell numbers (orange cells denote assemblies with thermocouple lances).	B-3
Figure B-2. Assembly identification numbers.	B-4
Figure B-3. Comparison of measured and predicted temperatures – Cell 2 (Assembly 3K7).	B-5
Figure B-4. Comparison of measured and predicted temperatures – Cell 6 (Assembly 30A).	B-6
Figure B-5. Comparison of measured and predicted temperatures – Cell 14 (Assembly 57A).	B-7
Figure B-6. Comparison of measured and predicted temperatures – Cell 19 (Assembly 3U9).	B-8
Figure B-7. Comparison of measured and predicted temperatures – Cell 24 (Assembly 3U4).	B-9
Figure B-8. Comparison of measured and predicted temperatures – Cell 28 (Assembly 3U6).	B-10
Figure B-9. Comparison of measured and predicted temperatures – Cell 31 (Assembly 5T9).	B-11

LIST OF TABLES

Table S-1. Changing decay heat estimates and associated peak fuel temperature predictions.	vi
Table 2-1. Emissivity values for radiation heat transfer.	22
Table 2-2. Summary of assembly loading map and projected decay heat values.	25
Table 2-3. Peak neutrons Shield temperature with and without regulatory solar insolation.	37
Table 3-1. Summary of assembly loading map and projected decay heat values.	40
Table 3-2. Updated emissivity values for radiation heat transfer.	43
Table 3-3. Split of heat loss through external boundaries.	60
Table 3-4. Peak neutron shield temperature with and without regulatory solar insolation.	63
Table 4-1. Pre-loading estimates of peak fuel cladding temperature.	65
Table 5-1. Grid convergence test data.	71
Table 5-2. Grid convergence index.	72
Table 5-3. Measured temperatures at thermocouple lance positions at end of thermal soak.	74
Table 5-4. Model results for temperatures at thermocouple locations – Convective Boundary Condition.	75
Table 5-5. Differences between model predictions and measured temperatures at thermocouple positions – Convective Boundary Condition.	75
Table 5-6. Comparison of model predictions with measured surface temperatures (°F).	78
Table 5-7. Model results for temperatures at thermocouple locations – measured temperatures as surface boundary condition.	82
Table 5-8. Differences between model predictions and measured temperatures at thermocouple positions – measured temperatures as surface boundary condition.	82
Table 5-9. Sensitivity results with COBRA-SFS model.	86

Table 5-10. Sensitivity results with STAR-CCM+ model..... 87
Table A-1. Average normalized axial decay heat profile.A-9
Table A-2. Thermocouple locations.....A-12

ACRONYMS

CAD	Computer Aided Design
CFD	Computational Fluid Dynamics
DOE	U.S. Department of Energy
EPRI	Electric Power Research Institute
FSAR	Final Safety Analysis Report
GCI	Grid Convergence Index
GWd/MTU	gigawatt days per metric ton uranium (measure of burnup)
IR	infrared
ISFSI	Independent Spent Fuel Storage Installation
NDA	Non-Disclosure Agreement
NRC	U.S. Nuclear Regulatory Commission
OD	outside diameter
OFA	Optimized Fuel Assembly
ORNL	Oak Ridge National Laboratory
PCT	Peak Cladding Temperature
PNNL	Pacific Northwest National Laboratory
PRA	Poison Rod Assemblies
PWR	Pressurized Water Reactor
R&D	research and development
SAR	Safety Analysis Report
SFWST	Spent Fuel and Waste Science and Technology (formerly Used Fuel Disposition Campaign)
TC	thermocouple
UFSAR	Updated Final Safety Analysis Report
WE	Westinghouse Electric

REGISTRATIONS AND TRADEMARKS

M5 [®]	A trademark of Framatome (formerly AREVA) registered in the USA and in other countries.
ZIRLO [®]	A registered trademark of Westinghouse Electric Company LLC in the United States and other countries.

This page is intentionally left blank.

THERMAL MODELING OF THE TN-32B CASK FOR THE HIGH BURNUP SPENT FUEL DATA PROJECT

1. INTRODUCTION

The Spent Fuel and Waste Science and Technology (SFWST) research and development (R&D) program of the U.S. Department of Energy (DOE) is conducting a high-burnup fuel demonstration at the North Anna Nuclear Power Station's Independent Spent Fuel Storage Installation (ISFSI). The storage system selected for this demonstration is a TN-32B cask (Figure 1-1). The main goals of this test are to provide confirmatory data for model validation and potential improvement, support license renewals and new licenses for ISFSIs, and support transportation licensing for high-burnup spent nuclear fuel (EPRI 2014). The focus of the High Burnup Spent Fuel Data Project (aka Demonstration project) is the performance of the high-burnup fuel.

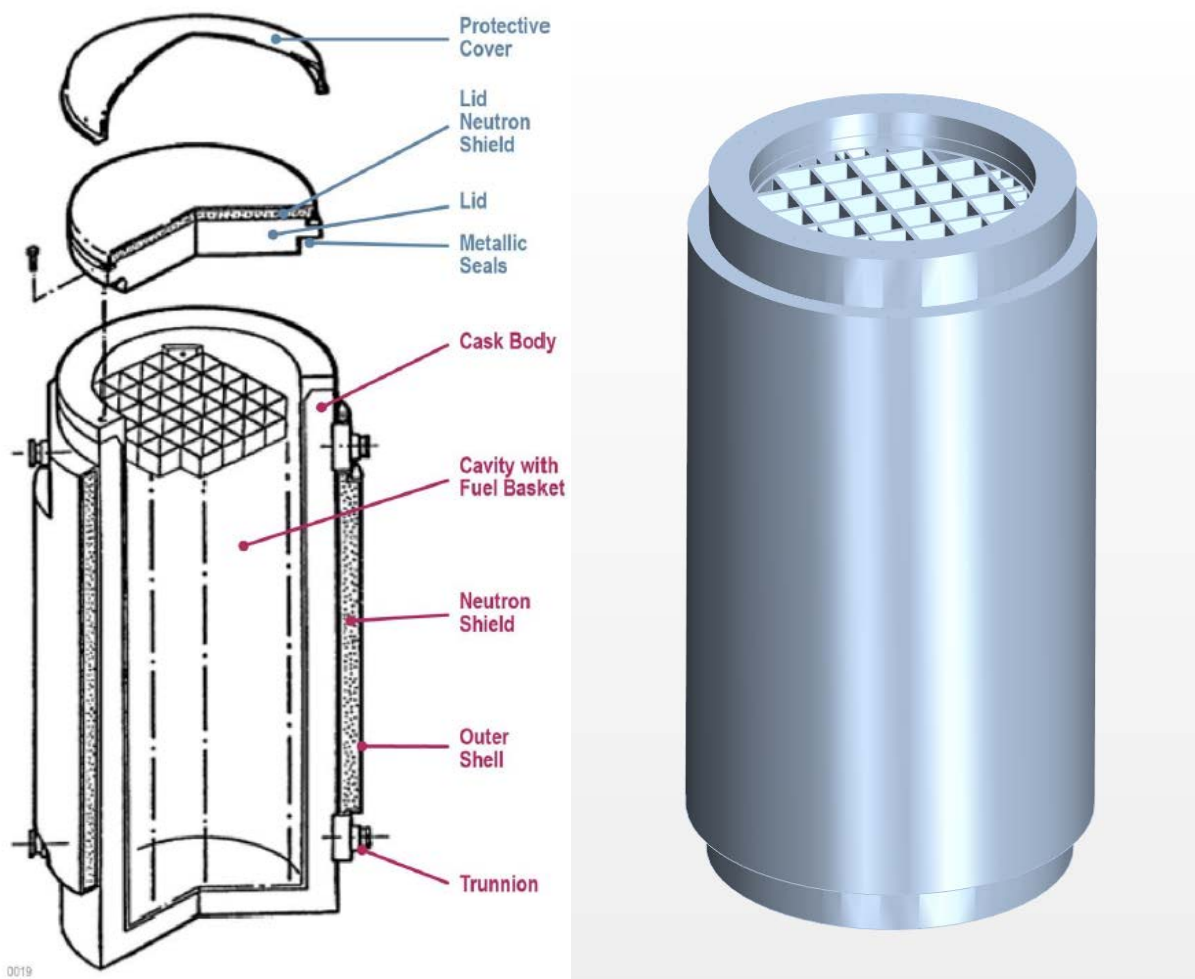


Figure 1-1. Diagram and geometry model⁵ for Orano TN-32B dry storage cask.

The TN-32B storage cask is a vertical module designed as a dual-purpose dry storage and transportation system for used nuclear fuel. The specific module used in the Cask Demonstration project is the TN-32B configuration, which is identical to the standard TN-32 cask, except that the top lifting trunnions are designed as single failure proof. The only modification to the cask design for the Demonstration project consists of penetrations through the lid, to accommodate the thermocouple lances to obtain temperature measurements within selected fuel assemblies in the basket.

The demonstration test plan was to begin dry storage with a loading of high-burnup fuel and cask decay heat that produced fuel temperatures approaching the peak cladding temperature (PCT) regulatory guidance limit for normal storage (400°C [752°F]) as specified in Interim Staff Guidance 11, Revision 3 (NRC 2003) and the Standard Review Plan, Revision 1 (NRC 2010), and monitor conditions during a 10-year storage period.

The purpose of the thermal analysis documented in this report is to support the Demonstration project in two primary areas:

⁵ In the diagram, rails between the fuel basket and cask inner wall are omitted for clarity. The protective cover, lid neutron shield, and the cask lid are shown removed from the geometry model; the rails are visible in this image.

1. To help the project team assess proposed loading patterns with respect to obtaining desired material's performance data, specifically for PCTs near 400°C for multiple cladding types, and
2. To obtain "best estimate" temperatures, especially for the cladding, for use in the SFWST storage and transportation programs.

This analysis supports the SFWST R&D program; independent thermal analyses by Dominion Energy and Orano TN were used in the License Amendment Request for the demonstration cask.

Estimates of fuel cladding temperatures were of primary interest, including the maximum temperature reached during the vacuum drying procedure and the range of temperatures expected at the beginning and end of the 10-year test period. To produce these estimates for storage conditions, detailed models of the TN-32B storage cask were developed using two codes, COBRA-SFS (Michener et al. 1995; Michener et al. 2017) and STAR-CCM+ (Siemens PLM 2016). The models developed for both codes represent the entire cask, but the capabilities of each code are exploited to capture detailed evaluations of different portions of the system.

COBRA-SFS models the fuel and basket region in detail, and provides accurate representation of heat transfer by radiation, convection, and conduction in the radial direction from the fuel to external ambient. Heat transfer paths through the base and top of the cask, which are by design of much lesser significance compared to radial heat removal, are treated in a more simplistic manner.

STAR-CCM+ is used to model the solid structures of the basket and cask body in detail, including the base and lid regions, but approximates the backfill gas and fuel assemblies within the basket as a porous media, and utilizes an effective thermal conductivity model to capture fuel cladding temperatures.

With consistent material specifications and the same boundary conditions, these two models are complementary and provide an effective consistency check to verify that the models are appropriately capturing the physical behavior of the system. This provides confidence that the results of the thermal evaluations accurately represent the temperatures achieved in the demonstration testing, within the uncertainty in the various input parameters provided.

The models and inputs produced for this study have been developed with the goal of obtaining "best estimate" representations of the Demonstration cask. They omit many of the conservatism and bounding assumptions normally used in design-basis and safety-basis calculations for spent fuel storage systems. They have also evolved over the course of the project, as more detailed and project-specific information became available to support more realistic modeling. Preliminary model inputs for load planning used non-proprietary fuel geometry and conservative estimates of decay heat. These inputs were updated to reflect fuel geometry provided by the fuel vendors under Non-Disclosure Agreement (NDA), as well as axial decay heat profiles and assembly pin-by-pin decay heat values based on burnup data provided by Dominion, also under NDA. For blind predictions of the actual loading, decay heats were adjusted for loading date and for removal of sister rods. In addition, cask geometry and external boundary conditions were updated to correspond to conditions of the cask in the decontamination pit. While initial estimates of storage temperatures for the initially planned summer 2017 loading were calculated assuming a conservatively hot ambient of 38°C (100°F), predictions of the cask temperatures following actual loading used measured room temperatures or measured cask surface temperatures to define external boundary conditions.

Estimates of cladding temperature during the vacuum drying process were also of interest; in particular, the PCT that could potentially occur during the vacuum drying process, for comparison to PCT under storage conditions once the cask is placed in the ISFSI. Preliminary models for the vacuum drying transient used typical bounding assumptions for Final Safety Analysis Report calculations for vacuum drying. In future work, these models will be rerun using actual conditions following the cask loading and vacuum drying procedure and results will be compared with measured temperatures in the fuel.

Preliminary models constructed for pre-test planning are described in Section 2. Updates to these models once NDAs were completed with the utility and fuel vendors are described in Section 3. Pre-loading estimates of fuel temperatures are provided in Section 4. Changes to these models for the blind test predictions are described in Section 5. Section 6 summarizes the main conclusions and recommendations from this work. Section 7 contains the list of references cited.

2. PRELIMINARY MODELING IN SUPPORT OF PRE-TEST PLANNING

Model development for the TN-32B cask began in early 2014. Two models proceeded in parallel, one using COBRA-SFS and the other using STAR-CCM+. The purpose of these models was to provide fuel cladding and cask component temperature estimates for the assembly loadings under consideration. This initial work was documented in Fort et al. (2015) and significant accomplishments are described in this section.

These preliminary models were built primarily using information from the system Updated Final Safety Analysis Report (UFSAR 2012). The assumptions and system details in the UFSAR are intended to produce conservative safety limit predictions, and therefore may not produce appropriately realistic estimates for evaluation of the performance of the cask in the Demonstration project. One assumption in the UFSAR thermal analysis neglects any contribution of thermal convection in the basket region. In an early set of models for this project it was assumed that the actual system would have significant convection, assuming the rails were supported off the bottom of the canister so that helium could flow upward through the fuel assemblies and return downward through the open sections in the extruded aluminum rails. The UFSAR drawings did not have sufficient detail to indicate otherwise.

When detailed drawings were received showing no gap between the rails and canister floor, and only very small drain holes at the bottom of the basket assembly fuel compartments, the geometry model was corrected to eliminate the flow path through the rails. With this flow path eliminated, the overall recirculation of fill gas is also eliminated, leaving only relatively small exchanges between individual assemblies due to their differing temperatures. By including this minor buoyant exchange, the models developed for this work are more realistic than the UFSAR assumption of no convection, but this effect is small for this cask design.

2.1 COBRA-SFS Model Description

This section describes the basic model of the TN-32B developed for thermal analysis with the COBRA-SFS code. Section 2.1.1 describes the representation of the solid material components of the system, and Section 2.1.2 presents a detailed discussion of the rod-and-subchannel representation of the fuel assemblies within the basket.

The fuel stored in the TN-32B cask in the Demonstration project is high burnup 17×17 Pressurized Water Reactor (PWR) fuel from the North Anna reactor. Section 2.3 contains a detailed discussion of the significant characteristics of the fuel assemblies that were selected for loading into the cask, as they relate to thermal modeling considerations.

2.1.1 Representation of TN-32B Cask for COBRA-SFS

The TN-32B cask consists of an internal basket structure composed of thin stainless-steel sheets, which form liners or fuel compartments for each basket cell, with thick aluminum plates sandwiched between them. These are arranged in a square grid, forming cells to accommodate 32 PWR fuel assemblies. The basket grid fits inside a thick-walled cask body of circular cross-section. The outer faces of the basket are supported within the “square-peg-in-round-hole” arrangement by extruded aluminum rails with a truss-like cross-section, flat on the side facing the basket plates and curved on the side facing the cask wall. The base of the cask is a thick plate of carbon steel, designed to sit directly on the concrete pad of the ISFSI. The top of the cask is a multi-layer bolted lid with metallic seals, and consists of a thick steel top shield plate, a thinner outer lid, and a resin neutron shield disc enclosed in carbon steel sheathing. The system also includes an additional outer lid, covering the bolted and sealed cask lid, forming a dome space that contains an overpressure tank and pressure monitoring system connected to the interspace between the double metallic O-ring seals in the cask lid. This is a redundant safety feature on the lid bolts and seals, to ensure that any seal leakage would be into rather than out of the cavity. Decrease in the

pressure of the overpressure system is signaled to a monitoring system that verifies the integrity of the cask lid seals throughout the storage lifetime of a given cask.

A basic diagram of the COBRA-SFS model of the TN-32B cask is shown in Figure 2-1. The major path of heat removal from the fuel assemblies in the TN-32B cask (and dry storage systems in general) is in the radial direction, by conduction and thermal radiation. (Convection can also be a significant mode of radial transport of heat, by means of a natural convection thermo-siphon through the basket and support structures of the cask internal cavity, but the geometry of the TN-32B basket and support rails does not allow this recirculation to occur.) Heat is removed from the cask exterior surface by natural convection to the essentially infinite heat sink of the ambient air. Heat can also leave the system through the lid structures and base of the cask, mainly by conduction, but this is generally an insignificant path compared to the radial path to convection from the outer wall of the cask cylinder.

Consistent with the significant heat transfer paths in the system, the COBRA-SFS modeling approach provides a detailed, highly resolved representation of the fuel assemblies, basket plates, support rails, cask body, and neutron shield over the axial length of the basket. This allows the model to represent heat transfer appropriately by conduction, convection, and thermal radiation in the region of most significant heat removal, to obtain accurate and physically meaningful predictions of local component temperatures, including detailed temperatures and temperature distributions for the fuel rods within the assemblies^f. Axial heat transfer paths from the system, which in most configurations consists of conduction through layered solid structures, is represented with one-dimensional heat transfer paths, using appropriate material properties and contact resistances for the layered components.

^f While this approach and model framework is appropriate for modeling this cask, accurate results require accurate estimates of parameters such as thermal gap resistances. See the discussion later in this section for how these were estimated or assumed when accurate values were not available.

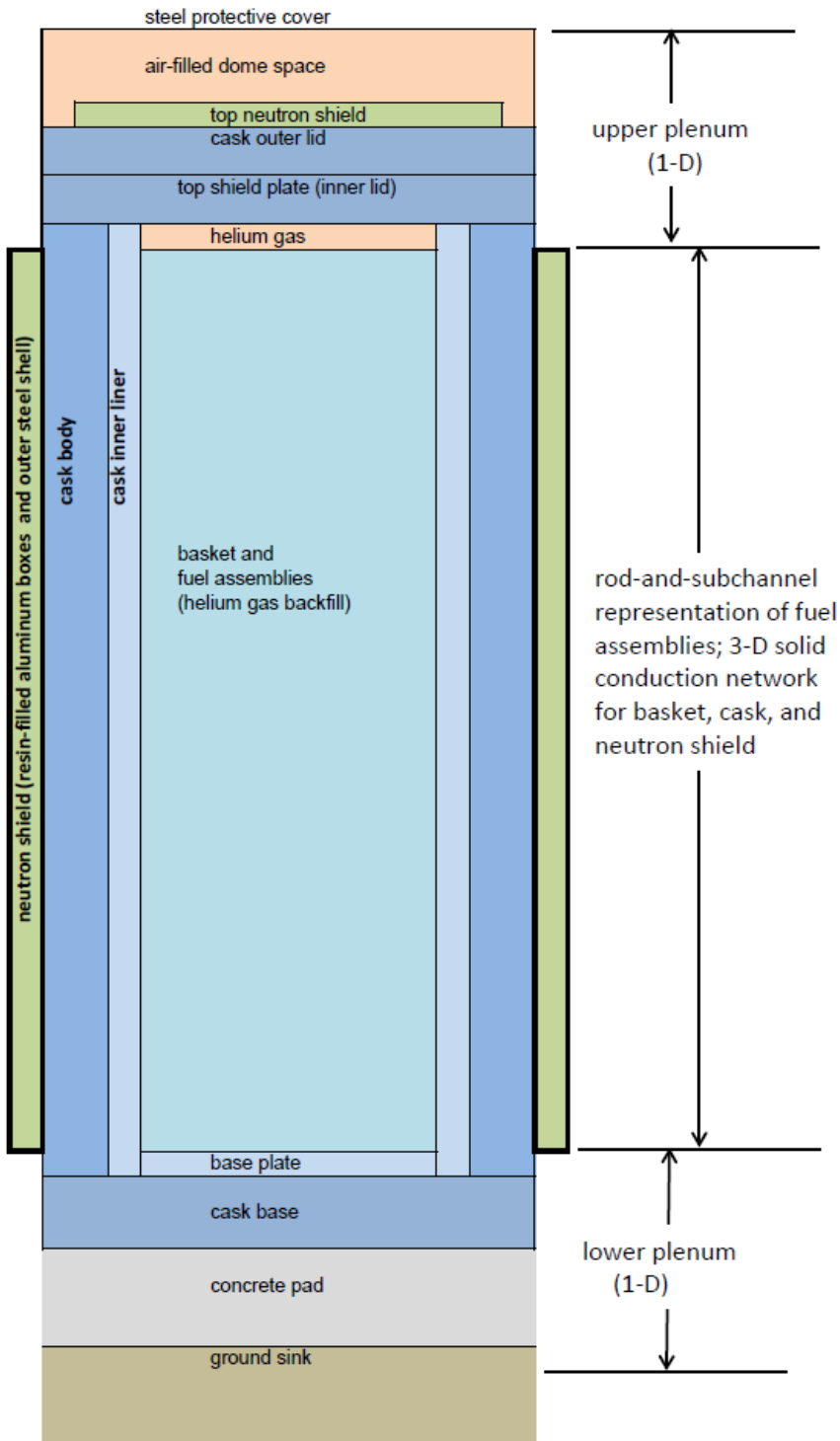


Figure 2-1. COBRA-SFS model regions for the TN-32B cask (NOTE: model image not to scale).

Diagrams illustrating the detailed 3-D solid conduction network for the COBRA-SFS model representation of the basket, support rails, cask body, and neutron shield are shown in Figure 2-2 and

Figure 2-3. These diagrams are not to scale, with nodal thicknesses greatly exaggerated for clarity. This portion of the model description focuses on the representation of the radial heat transfer paths through the basket, support rails, and cask shell, to ambient. The basket cells are formed by thin stainless-steel sheets (shown in light turquoise in the diagram in Figure 2-2), with stainless-steel sheets on the outer faces of the basket structure. Much thicker aluminum alloy plates are sandwiched between the stainless-steel plates, with double-thickness aluminum plates forming the central “cross” of the basket. Some of these aluminum plates include a very thin layer of borated aluminum in the sandwich, but the thermal properties of this material are identical to that of the structural plates, and therefore they are not explicitly modeled in this representation of the basket.

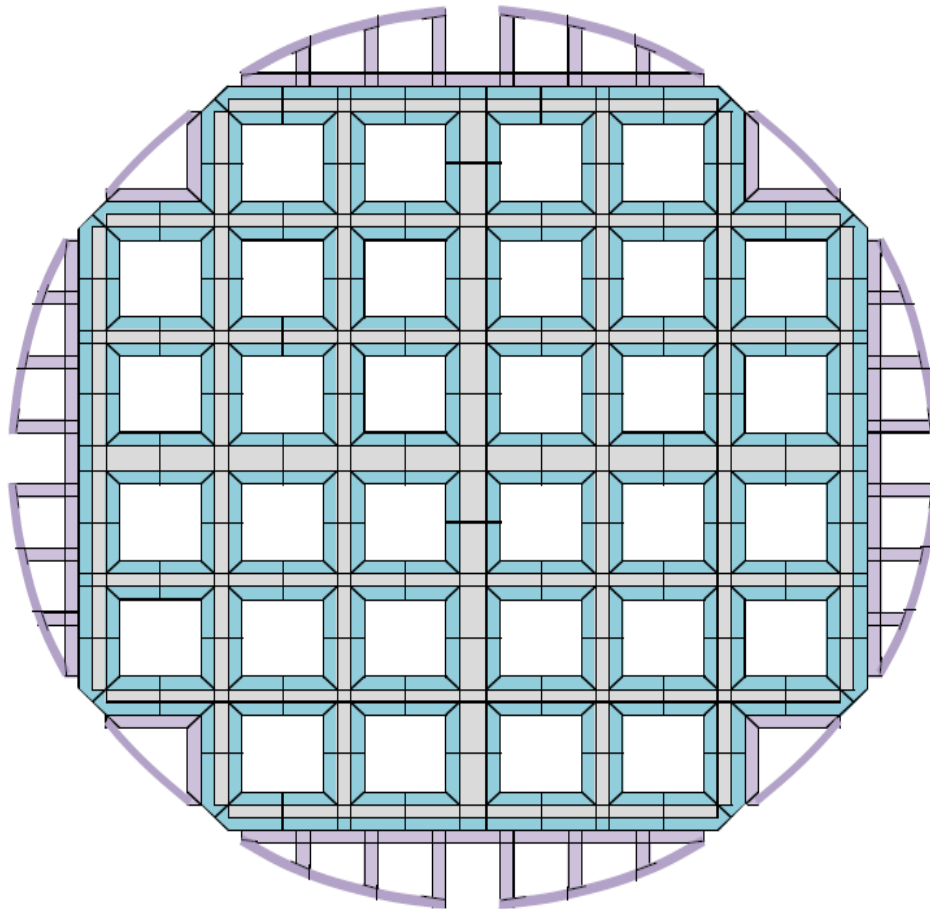


Figure 2-2. Diagram of 3-D COBRA-SFS model of TN-32B basket – rails in purple, fuel compartments in blue, and aluminum structures in grey (NOTE: diagram not to scale; node thicknesses greatly exaggerated for clarity).

The layers of plates comprising the basket are fastened together by stainless-steel plugs that pass-through holes in the aluminum alloy plates and are fusion welded to the enclosing steel plates. As a bounding conservatism, the model of the TN-32B basket in the UFSAR (2012) specifies the thermal conductivity of the aluminum regions at a value reduced by 10%, to account for any effect the stainless-steel plugs might have on conduction heat transfer radially in the basket. This is an unrealistic conservatism, since the steel plugs comprise less than 5% of the total area of the basket plates and would have a negligible effect on conduction heat transfer rates through the basket. As a convenient and realistic simplification, the

stainless-steel plugs are neglected in the COBRA-SFS model. Only the layers of aluminum and thin sheet steel are represented, as illustrated in Figure 2-2.

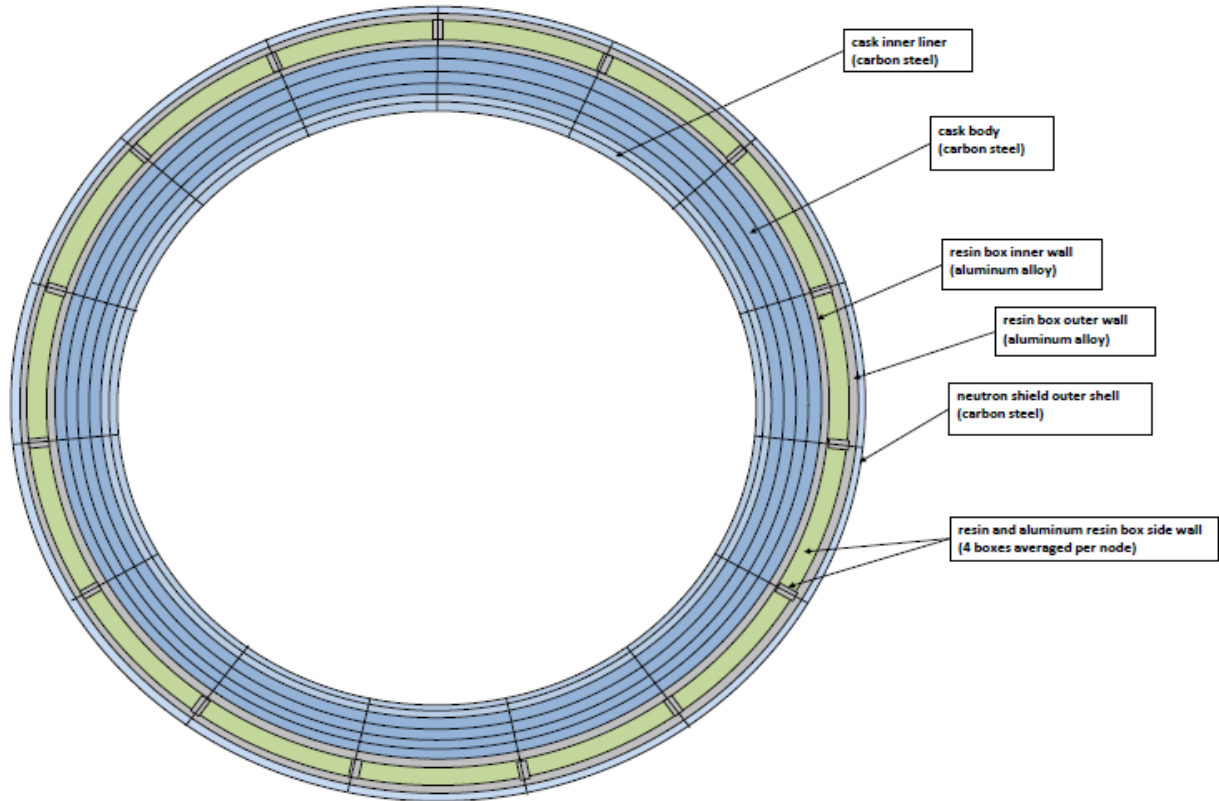


Figure 2-3. Diagram of 3-D COBRA-SFS model of TN-32B cask cross-section illustrating nodalization of cask body, neutron shield, and exterior surface (NOTE: diagram not to scale; node thicknesses greatly exaggerated for clarity).

A more realistic modeling concern is the imperfect contact between adjacent steel and aluminum alloy plates, and the consequent effect on contact conductance, since the plates are fastened together only at intermittent points, and the two materials have different coefficients of thermal expansion. The UFSAR model of the TN-32B basket uses a reasonable value based on fabrication tolerances and thermal expansion coefficients for the dissimilar materials to represent the gap between plates. The COBRA-SFS model also utilized this same value. Heat transfer across the gap is assumed to consist of conduction through helium gas filling the gap, and thermal radiation between the adjacent flat plates.

The aluminum alloy support rails between the flat outer faces of the basket and the inner liner of the cask cavity are modeled as shown in Figure 2-2. In the COBRA-SFS model, the basket-and-rails noding mesh illustrated in Figure 2-2 is contiguous with the noding mesh for the cask shell, shown in Figure 2-3. The two regions of the model are shown separately in these two figures simply for clarity, as this is a large and complicated mesh. In the TN-32B cask, the support rails are fastened to the inner liner of the cask cavity with bolts at intermittent locations along the axial length of the basket. As with the basket plate structures, the intermittent fastener design and the differing coefficients of thermal expansion for the aluminum alloy rails and carbon steel shell would create imperfect and non-uniform contact between the rails and the shell, along the axial length of the rails. Since the actual contact lengths are unknown (and in effect unknowable), the intermittent contact is modeled with a uniform gap based on a reasonable

engineering estimate of the average gap that might be seen in such a structure. The UFSAR model assumes a small, relatively realistic gap to represent the contact conductance between these structures. This same value was used in the COBRA-SFS modeling, after verifying that it was a reasonable approximation, based on fabrication tolerances and thermal expansion coefficients for the two materials involved.

The inner flat sides of the support rails are not directly fastened to the facing flat outer surfaces of the basket plates in the TN-32B cask, as a design feature to minimize mechanical stresses in the basket due to expansion and contraction in response to temperature changes and temperature gradients through the basket. The UFSAR thermal model of the cask represents the potential gap between the basket outer plates and the inner face of the support rail with a uniform width on all faces, estimated from fabrication tolerances and thermal expansion evaluations for the design-basis decay heat load. The approach used to estimate this gap is conservative, but without more detailed information on the as-built dimensions of the actual cask to be used in the Demonstration project, there is no reasonable basis for justifying a smaller gap. The value from the UFSAR modeling is therefore used for this gap in the COBRA-SFS model.

As shown by the diagram in Figure 2-3, the noding for the COBRA-SFS model becomes much simpler for the cask body, in keeping with the much simpler geometry and direct radial heat transfer paths through the layered steel shells of the cask. The noding for the cask shell is divided into segments encompassing 24° of arc, which provides a reasonable interface with the detailed modeling of the cask internal structure, as illustrated in Figure 2-2. The somewhat less detailed azimuthal resolution of the cask shell in the modeling captures the modest asymmetry in the fuel loading pattern currently specified for the cask (see discussion in Section 2.3). The thin carbon steel inner liner is represented with a thickness of two nodes, to capture the cavity inner surface temperature. The thick carbon steel layer comprising the cask gamma shield is represented with four layers of nodes. Comparison with temperature gradients obtained in the more detailed mesh of the STAR-CCM+ model show that this is more than sufficient to capture the radial and circumferential gradients in the thick metal layers of the cask structure. To account for fabrication uncertainties, a small contact gap is assumed between the inner liner and the gamma shield. This is consistent with treatment of this interface in the UFSAR.

The neutron shield for the TN-32B cask consists of a ring of 60 long thin aluminum alloy boxes filled with a polyester resin, which are attached directly to the outer surface of the thick carbon steel gamma shield. The UFSAR does not state specifically how these boxes are attached to the curved outer steel wall of the gamma shield layer. The thermal model in the UFSAR assumes a small gap between these structures, to account for incomplete contact, and for simplicity, this same value was used in the COBRA-SFS modeling. It is assumed that thermal expansion will result in tight side-to-side contact between adjacent boxes, but because there is no significant circumferential temperature gradient around the neutron shield for this geometry and anticipated decay heat load, this has no effect on results. In the COBRA-SFS model, the resin boxes are averaged to represent the equivalent of four boxes per node, in keeping with the circumferential resolution of 24° of arc for the shell of the cask in the model (see Figure 2-3). This approach preserves the radial thickness of the heat transfer path, but simplifies the circumferential distribution of material, which has essentially no effect on temperature gradients in the system.

The aluminum boxes forming the neutron shield are enclosed in a thin sheet of carbon steel, which is exposed to ambient air. The UFSAR does not describe how this steel sheet is attached to the neutron shield, but the design-basis thermal modeling assumes a small contact gap between the steel outer sheathing and the outer faces of the aluminum boxes. For simplicity, and lacking any other information, this gap was also assumed in the COBRA-SFS modeling.

2.1.2 Representation of Fuel Assemblies and Internal Convection in COBRA-SFS Model of TN-32B

The fuel assemblies within each of the 32 cells in the TN-32B basket are represented in the COBRA-SFS model using rod-and-subchannel modeling of the actual assembly geometry. This approach uses a representation of the fluid flow and heat transfer paths within the rod array that was originally developed for analysis of core hydrodynamics in operating reactors and is still in use today in reactor core and primary system modeling software. The original reactor core code was later expanded and extended to be applicable to computational fluid and thermal analysis of spent fuel assemblies in dry storage casks, primarily by adding a detailed rod-to-rod and rod-to-wall thermal radiation modeling capability (see the COBRA-SFS documentation[§], Michener et al. 1995 and Michener et al. 2017, for full details).

A diagram of the basic rod-and-subchannel array for a 17×17 assembly is shown in Figure 2-4. (This diagram is not to scale; the gaps between the rods are greatly exaggerated for clarity.) This diagram is a generic illustration of the rod-and-subchannel modeling for a fuel assembly of this type and does not show local variations due to guide tubes, instrument tube(s), or burnable poison rods. However, the COBRA-SFS model is capable of taking into account these individual variations in specific fuel assembly designs, and the variations in the specific assemblies (of three different types) to be loaded into the demonstration cask.

Since NDAs with the fuel vendors were not yet available at this early point in the model development, the COBRA-SFS model used the geometry of Westinghouse (WE) 17×17 LOPAR and WE 17×17 V5H from the discontinued OCRWM database (DOE/RW 1987) to represent the WE fuel at North Anna. WE B&W Mark BW was used to represent the Framatome AMBW fuel assemblies.

A unique feature of the COBRA-SFS code is the detailed modeling of the flow field within the fuel assemblies within the individual basket cells, accounting for local heat transfer by conduction and convection. Thermal radiation is also calculated directly, using grey-body view factors (rod-to-rod and rod-to-wall) for all rods in the array. This representation of the fuel assembly allows for a much more accurate resolution of the local gas temperatures and velocities, fuel cladding surface temperatures, and rod internal temperatures, compared to the typical approach used in Computational Fluid Dynamics (CFD) and finite element analysis codes. In CFD codes, the assembly is typically modeled as a porous medium, and in both CFD and finite element analysis codes, thermal radiation and conduction heat transfer within the fuel assembly is typically represented as a homogeneous block, using an effective conductivity model.

[§] Cycle 4 of the COBRA-SFS code, which was used for the work reported here, was released to the Radiation Safety Information Computational Center (RSICC) as of October 2015. Cycle 4a was released in November 2017. It is available to the public (at rsicc.ornl.gov/codes/psr/psr6/psr-614.html), and includes complete documentation in electronic format.

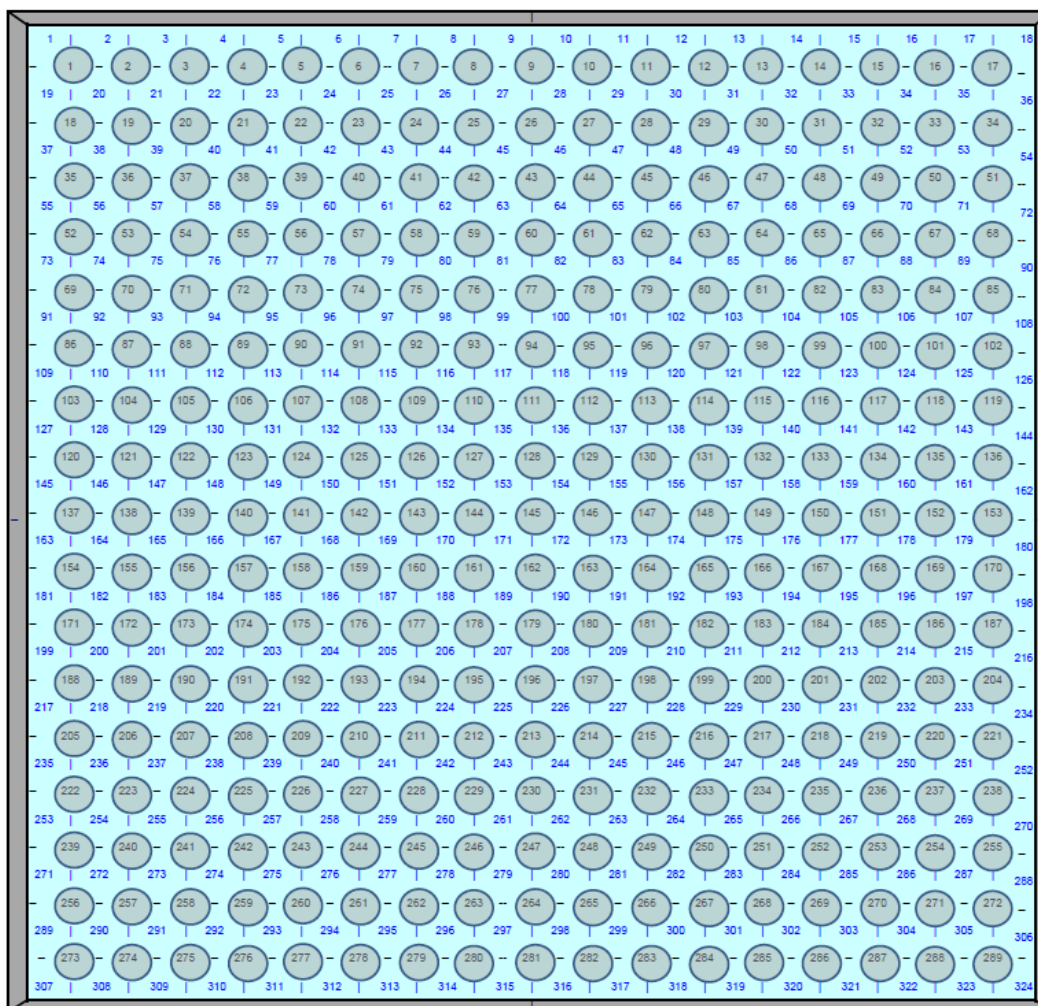


Figure 2-4. Rod-and-subchannel array diagram for COBRA-SFS model of 17×17 fuel assembly within basket cells of TN-32B (NOTE: diagram is not to scale).

For fluid convection within the system, heat transfer is represented with a user-specified heat transfer correlation. Based on validation of the COBRA-SFS code in Michener et al. (2017) with experimental data from horizontal and vertical test systems and canisters loaded with actual spent fuel^h, convection is represented with the venerable Dittus-Boelter heat transfer correlation for turbulent flow,

$$Nu = 0.023(Re^{0.8})(Pr^{0.4})$$

where

Nu = Nusselt number

Re = Reynolds number, based on subchannel hydraulic diameter

Pr = Prandtl number for the backfill gas

For laminar flow conditions, a Nusselt number of 3.66 has been verified as applicable to spent fuel rod arrays (Lombardo et al. 1986; Michener et al. 1995; Rector and Michener 1989). In the COBRA-SFS code, the local heat transfer coefficient is defined as the maximum of the values calculated from the

^h See, in particular, the validation and verification section of Michener et al. 2017.

laminar and turbulent correlations specified by user input. Figure 2-5 illustrates the convenient mathematical behavior of these correlations as a function of Reynolds number.

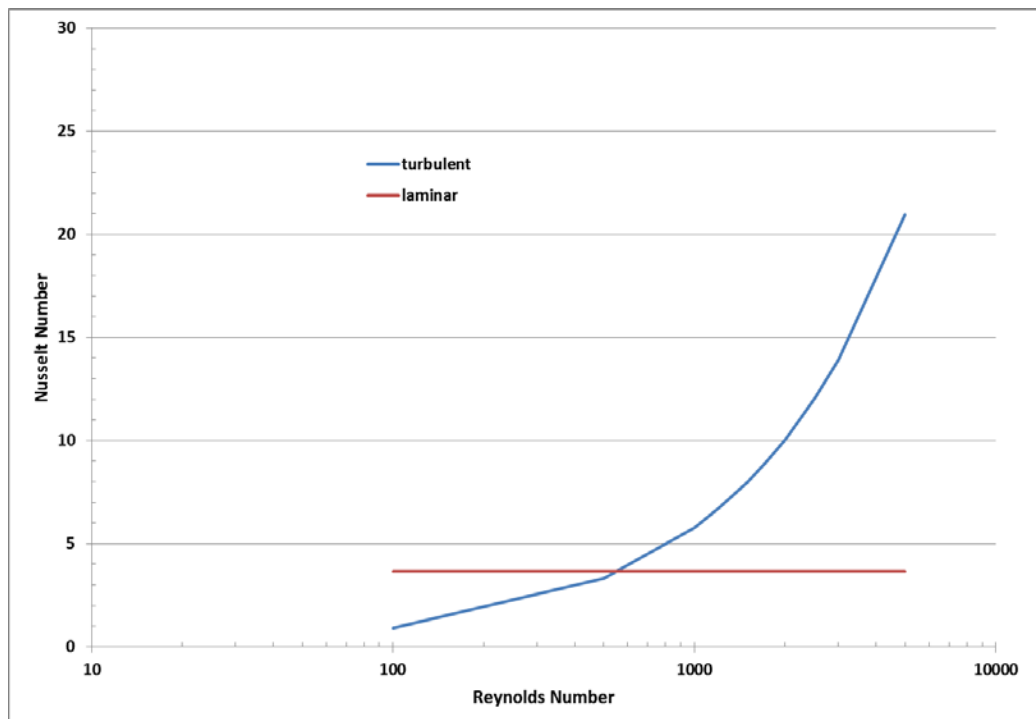


Figure 2-5. Laminar and turbulent formulations for Nusselt number.

For thermal radiation heat transfer, surface emissivity values of the channel boxes, basket, and canister wall were estimated from standard material propertiesⁱ. Steel components were specified with emissivity 0.45, aluminum components were specified with emissivity 0.2. The external shell of the cask, which is painted carbon steel, was specified with an emissivity of 0.9 for thermal radiation to the environment. The fuel rod cladding surface emissivity was assumed to be 0.8, which is a typical realistic estimate for spent fuel rods (Michener et al., 2017).

The open regions of the support rails, as illustrated in the diagram in Figure 2-2, are represented as gas flow channels that could, potentially, allow a thermo-siphon natural convection recirculation within the cavity, with helium gas rising through the fuel assemblies within the basket, absorbing heat from the fuel rods, then mixing in the narrow head space above the basket and sinking down the open channels in the support rails, as heat is transferred from the gas to the cooler steel wall of the cask. However, in the TN-32B, the extruded aluminum structures of the support rails sit directly on the floor of the cavity, and there is no “return path” for the cooled helium gas to reach the inlet to the fuel assemblies within the basket. The plates comprising the walls of individual basket cells have small openings on each cell face at the base of the basket, to facilitate draining of the cask during drying operations, but the support rails do not include such openings in this particular design. This feature essentially shuts down any possibility of significant convection heat transfer within this cask^j.

ⁱ See for example, Incropera (2007).

^j For the STAR-CCM+ model, Figures 3-24 and 3-25 show helium velocity distribution in the cask and Figure 3-26 interchange of the gas through the basket drainage holes. But the velocities in the fuel region are small because the flow path in the rails is a dead end. As a result, peak fuel temperatures differ little for this configuration if convection is enabled or not.

As the thermal analysis results in Section 2.4 show, this cask design efficiently transfers heat by conduction and thermal radiation, and does not require the added effect of convection to meet design-basis specifications. The COBRA-SFS modeling results show a minor recirculation within the basket itself, within the hotter fuel assemblies, at very low velocities. This has some effect on peak temperatures and temperature distributions within the system, as shown by comparisons between predicted temperatures for storage conditions and analyses of postulated vacuum drying conditions (see Section 2.4.2).

2.1.3 Boundary Conditions

The external ambient conditions for these preliminary thermal evaluations of the TN-32B cask assumed a uniform temperature of 38°C (100°F) in still air. This is a typical assumption for design-basis evaluations of normal conditions of storage and is generally bounding for nearly any ISFSI site in the United States. The TN-32B cask to be used in the Demonstration project will be stored in the ISFSI at Dominion's North Anna plant, located in central Virginia, northwest of Richmond. The North Anna Power Station is located on the North Anna River, on the 9,600-acre Lake Anna reservoir, created to provide cooling water for the station.

The weather at the ISFSI is governed by the typical central Virginia climate, with hot, humid summers and mild winters. The air temperature seldom, if ever, breaks 38°C (100°F), but the site experiences high winds and significant precipitation. Seasonal variation in ambient conditions, including air temperature variations, and possibly also the effects of severe weather conditions if they persist over more than a few days, can be expected to affect the thermal response of the fuel stored in the TN-32B over the life of the Demonstration project. However, thermal evaluations to quantify these effects, or determine reasonable bounds for them, would require projecting local weather conditions over a period of 10 years, when forecasters generally have difficulty projecting as far into the future as 10 days. The calculations presented in this report are for steady-state conditions, and a more reasonable approach would be to compare actual data from the Demonstration project, as it becomes available, to these steady-state predictions. This could provide a reasonable basis for assessing the uncertainty associated with temperature predictions determined for assumed steady-state modeling conditions, compared to actual temperatures experienced in the system over the duration of the project.

Solar heat loading on the exterior of the cask was ignored for these preliminary thermal evaluations. Sensitivity studies on this boundary condition show that it has negligible effect on PCT. However, solar heat load can have a significant effect on cask component temperatures, particularly on the lid structures and the exterior neutron shield. Some limited sensitivity calculations were completed near the end of this study and are included in the results (see Sections 2.5.2 and 3.5.2 for STAR-CCM+ sensitivity results and related COBRA-SFS testing with and without solar insolation in Section 3.4.6). But these evaluations would be most useful if performed for the final configuration of the TN-32B for the Demonstration project, and if possible, for solar heat loads typical of the North Anna site.

2.2 STAR-CCM+ Model Description

This section describes the basic model of the TN-32B cask developed for thermal analysis with the STAR-CCM+ code. Section 2.2.1 describes the representation of the cask geometry and several alternatives for the computational mesh. Sections 2.2.2 through 2.2.8 briefly discuss material properties, models and settings used for a generic application of the TN-32B. Model inputs that are specific to the use of the TN-32B in the Demonstration project are described in Section 2.3.

The STAR-CCM+ model of the TN-32B closely parallels that reported for the TN-24 cask by Brewster et al. (2012). The present model was initially developed using STAR-CCM+, version 9.02 and final modifications and runs were made with version 10.02.

The fuel assemblies are modeled as a homogenized porous medium, over the active length of the fuel rods only. The upper and lower portions of the assemblies (rods and nozzles) are ignored, modeling those regions with helium gas alone. Brewster et al. (2012) use porous media loss coefficients derived from a single detailed assembly flow model. They also include results for one single assembly modeled in detail, for comparison with the remainder modeled using the porous media representation. The initial approach for the TN-32B model was to do the detailed modeling of the assemblies using COBRA-SFS and use the results to set porous media loss coefficients in the STAR-CCM+ model. However, as described previously, the fact that there is no path for significant recirculation in the TN-32B made this modeling effort unnecessary.

2.2.1 Cask Geometry

The initial model of the TN-32B cask was created using the computer aided design (CAD) program SolidWorks® (Dassault Systems 2011) from drawings in the UFSAR (2012). The external view of the assembly model is shown in Figure 2-6. The axial cross-section of the cask geometry is shown in Figure 2-7 with a more detailed view of the upper half in Figure 2-8. A radial cross-section through the basket region is shown in Figure 2-9. The section in Figure 2-7 is through the axial centerline of the cask and between fuel channels in the basket (see Figure 2-9). The more detailed view in Figure 2-8 is offset from the centerline, passing through the adjacent row of fuel compartments. The horizontal line near the top of each fuel compartment in this image (Figure 2-8) marks the upper limit of the active fuel region.

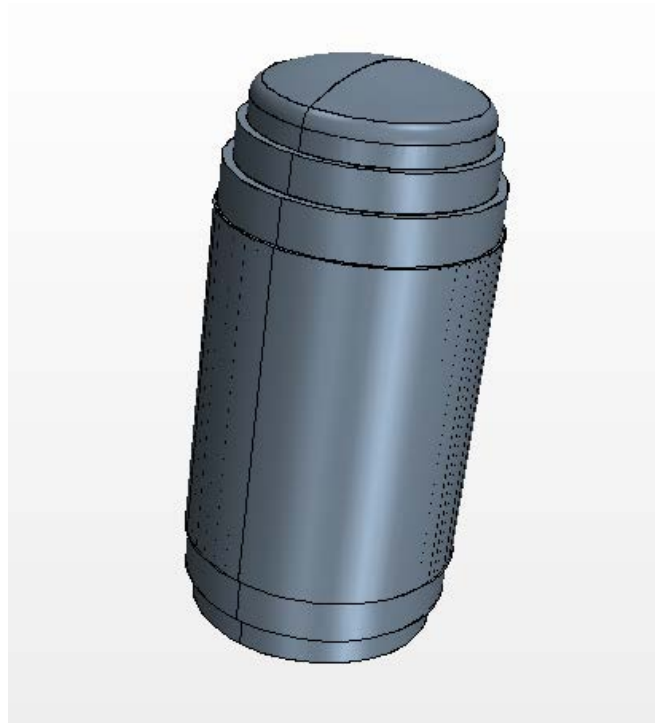


Figure 2-6. External view of TN-32B model CAD geometry.

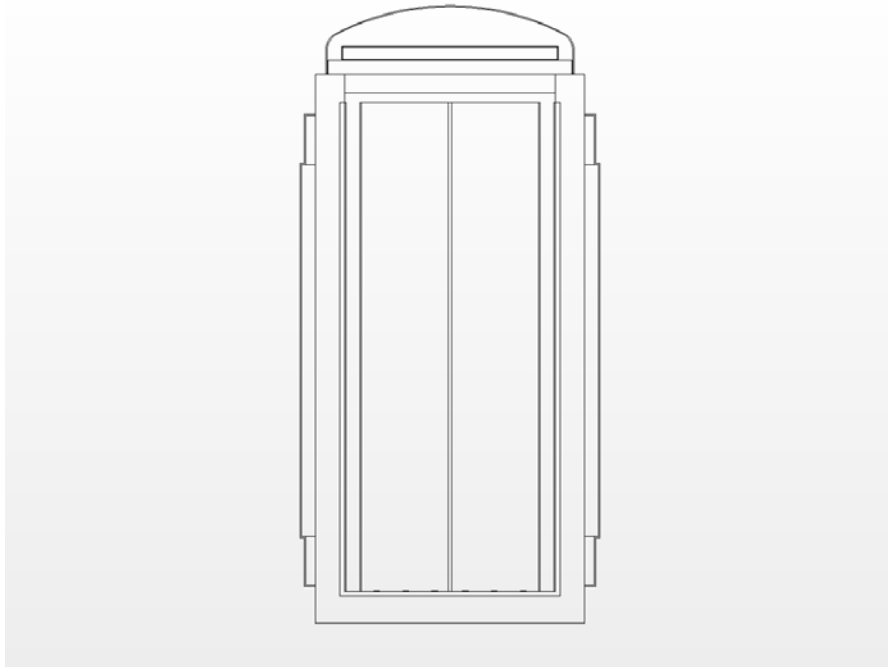


Figure 2-7. Axial cross-section of TN-32B model geometry.

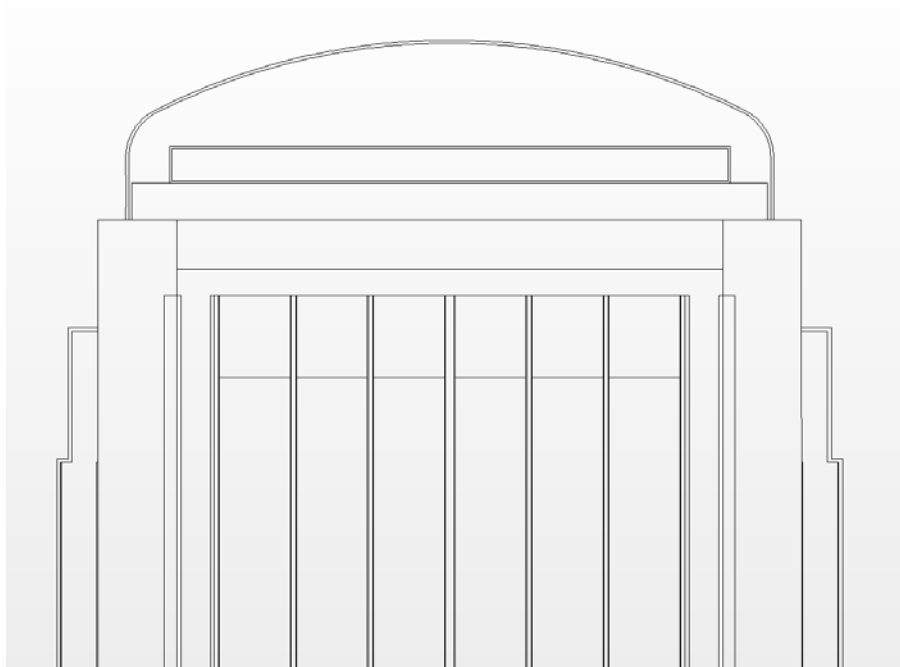


Figure 2-8. Axial cross-section of upper half of TN-32B model geometry.

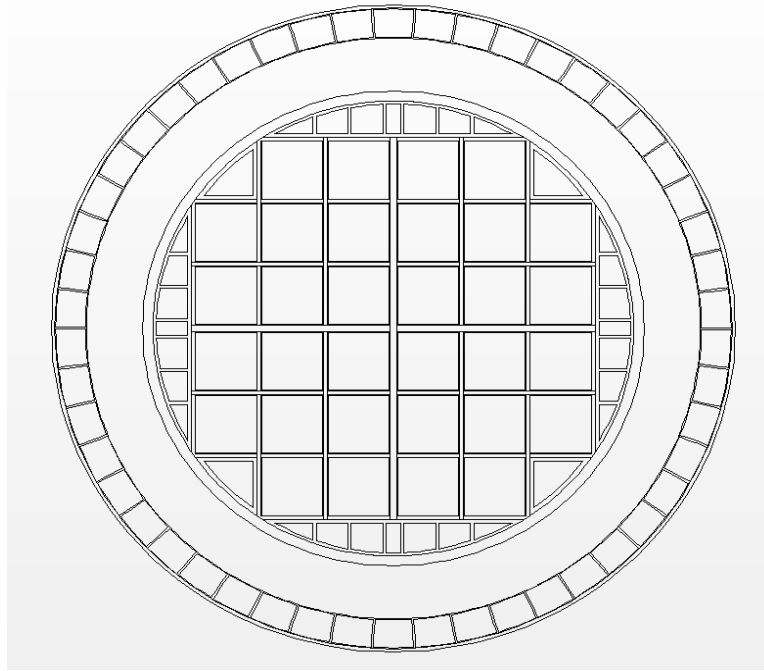


Figure 2-9. Radial cross-section of TN-32B model geometry.

2.2.2 Computational Mesh

The complete CAD assembly developed in SolidWorks® was imported into STAR-CCM+. The geometry was meshed into three different configurations, the first having a simplified treatment of thin section details in the basket and the other two using different cell types in the heated zone of the fuel assemblies. The purpose of this approach was to compare model accuracy and computational efficiency. The three configurations are defined as follows:

1. Simple – This mesh follows the same approach used in Brewster et al. (2012), with the basket modeled as uniform solid material, including the thickness of fuel compartments, and using a trim-cell^k mesh in the heated porous media modeled section of the fuel assemblies and polyhedral cells everywhere else. The total cell count for this model is 18 million.
2. Trim-cell – This is the same mesh as in the first case, except that the thickness of the fuel compartments is modeled using a separate layer of cells. Total cell count for this model is 22 million.
3. All-poly – This is the same as the trim-cell mesh, except that the entire mesh is comprised of polyhedral cells. Total cell count for this model is 31 million.

At the outset it was not certain that the thin fuel compartments could be effectively meshed and modeled, so the first mesh (Simple) was developed as an alternative, using an approach known to be successful in other similar applications. However, models using the second and third meshes (Trim-cell and All-poly) were able to run successfully. Since modeling the stainless-steel fuel compartments separate from the aluminum basket was the preferable approach, the simple mesh was not used and no results for that mesh are presented here.

^kAs opposed to arbitrarily shaped polyhedral cells used elsewhere in the model, the trim-cell mesh in the fuel region is comprised of structured hexahedral cells (having equal thickness and widths) with their edges trimmed as needed to match solid boundaries.

The all-polyhedral mesh (All-poly) was used for the final model because it is most easily produced and initial results showed no significant computational penalty for its use or difference in results from the trim-cell mesh. Along each wall/fluid interface, the polyhedral mesh contains a prism cell layer to improve the accuracy of the flow solution near the walls. The prism layer consists of orthogonal prismatic cells, two cells thick, adjacent to the wall boundaries. In addition, all interfaces between separate regions of the all-polyhedral mesh are conformal, whereas the interface between the trim-cell mesh for fuel region and polyhedral mesh on either end is non-conformal and requires averaging.

Figure 2-10 shows the polyhedral volume cell mesh (All-poly) of the TN-32B model using an axial slice through the central row of fuel baskets. Figure 2-11 shows a detailed view of the mesh for a transverse slice through the module near the middle of the axial length of the storage module.

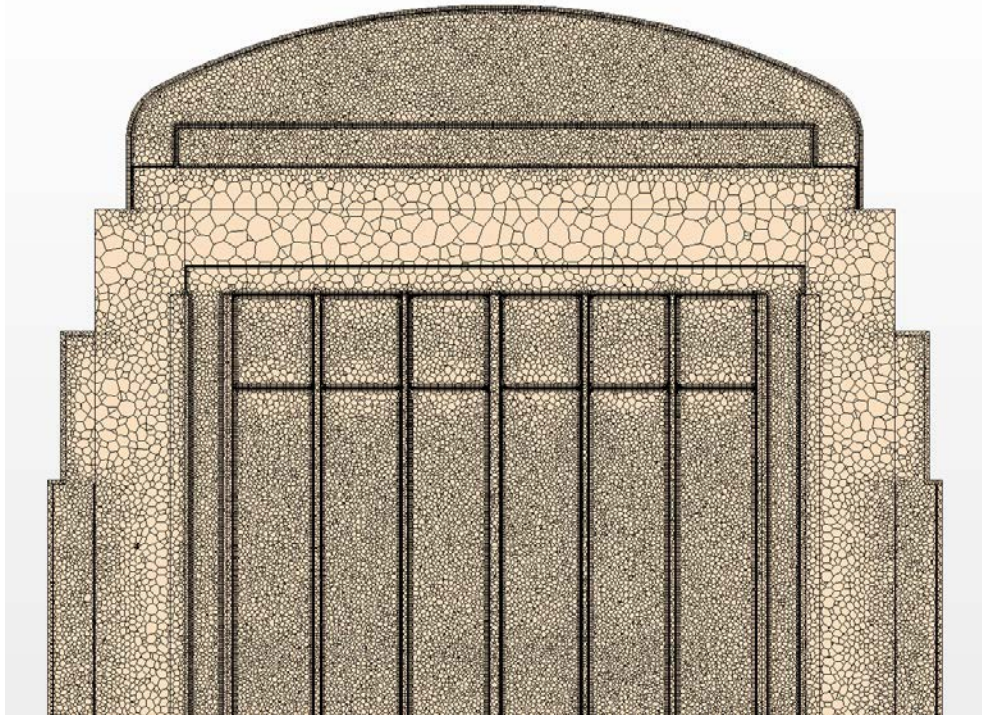


Figure 2-10. Planar slice through axial centerline showing volume mesh of the STAR-CCM+ model.

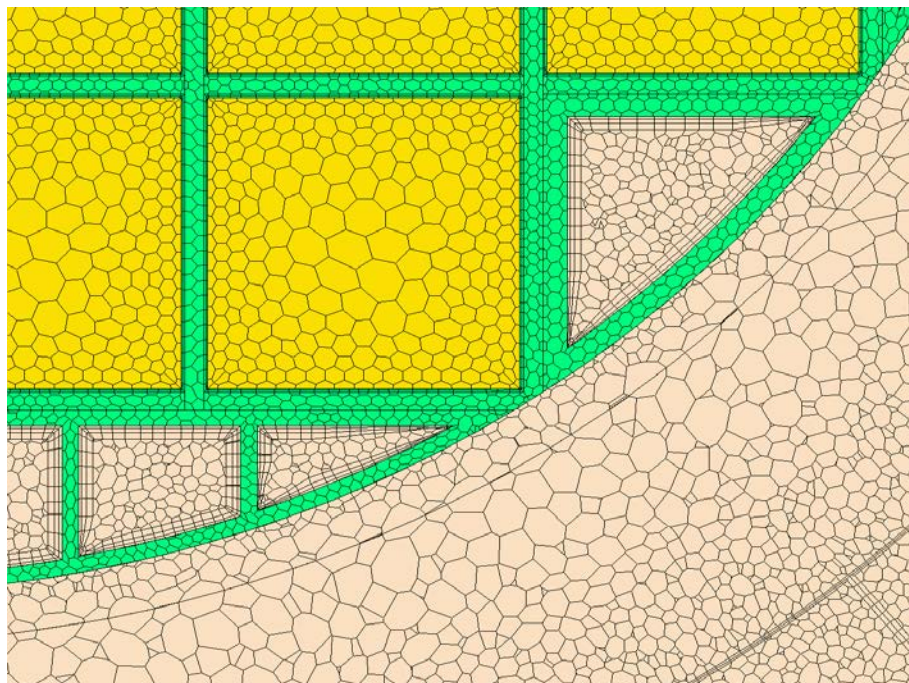


Figure 2-11. Planar slice through mid-line showing volume mesh of the STAR-CCM+ model – fuel regions, basket, liners, and rails highlighted.

2.2.3 Material Properties

Temperature dependent properties were used in the STAR-CCM+ model for all solids and for both gases (air and helium). For thermal conductivity and dynamic viscosity of air, this was accomplished with inputs to Sutherland's law, a generalized mathematical fit for these properties included as an option in STAR-CCM+. These material properties for helium (from Incropera et al. 2007) were included in the STAR-CCM+ model as user defined input tables. For the solids, temperature dependent tables for carbon steel and for Types 6061 and 6063 aluminum alloys were used directly from the TN-32B UFSAR after verifying them against independent reference values.

The fuel to be stored in the TN-32B cask in the Demonstration project is high burnup 17×17 PWR fuel from the North Anna reactor. Section 2.3 contains a detailed discussion of the significant characteristics of the fuel assemblies that have been selected for loading into the cask. The fuel assemblies were represented using a homogeneous k-effective model, as described in the Section 2.2.4.

2.2.4 Fuel Effective Conductivity

The appropriate fuel effective conductivity for a given application depends on the fuel assembly geometry, the assembly decay heat, and the geometry of the basket cell in which the fuel assembly resides (Bahney and Lotz 1996). The surface emissivity of the fuel rod cladding and the basket cell walls also need to be taken into account in developing an appropriate effective conductivity model for a particular application. Detailed information needed to independently develop effective conductivity models for the fuel proposed for insertion in the demonstration cask was not available at the beginning of this modeling effort. Therefore, to allow the thermal analysis work to go forward as project needs required, existing models were used instead. This included the axial effective conductivity model documented in the TN-32B UFSAR and a transverse effective conductivity model that had previously been developed by Pacific Northwest National Laboratory (PNNL) for WE 17×17 Optimized Fuel Assembly (OFA) fuel assemblies

at 0.6 kW. The calculated values and curve fit for the transverse effective conductivity model are shown graphically in Figure 2-12.

The transverse effective conductivity model for WE 17×17 OFA fuel assemblies provides a reasonable approximation of the effective conductivity of the actual fuel assembly types to be loaded into the TN-32B cask for the Demonstration project and was viewed as being adequate for use in final calculations. However, the effective conductivity model is intentionally conservative, and accuracy of predictions can be sensitive to the assumed decay heat of the assembly and assembly geometry. Since the actual fuel to be loaded in the TN-32B differs somewhat from the geometry of WE 17×17 OFA and is at different decay heat values than were assumed as the bounding value in the earlier analyses, this approach introduces some additional uncertainty into these preliminary thermal analyses for the Demonstration project.

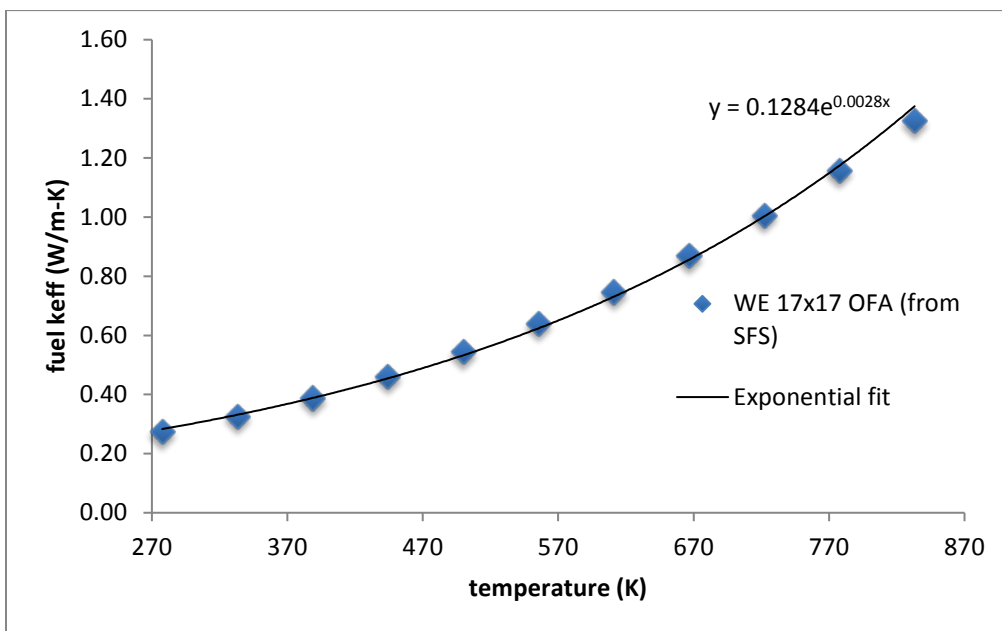


Figure 2-12. PNNL developed transverse thermal conductivity used in STAR-CCM+ model.

For the axial effective conductivity of the assembly, the approach used in the UFSAR is standard and reasonable for this application. It was therefore adopted in the STAR-CCM+ model. This approach neglects any contribution from thermal radiation and convection and defines the effective conductivity in the axial direction for the homogeneous block representing the fuel assembly by the area-weighted average of the conductivity of zircaloy cladding and helium backfill gas. Axial conductivity through the fuel pellets is neglected as insignificant relative to axial conduction in the cladding and backfill gas. A curve fit to the temperature dependent axial effective conductivity shown in the UFSAR was used in the STAR-CCM+ model.

2.2.5 External Boundaries

The external environment of the TN-32B model consists of the still, ambient air surrounding the cask, with contact at the base of the cask with a concrete pad. Since the TN-32B is not ventilated, the external boundary conditions are thermal only, including convection and radiation off the top surfaces and sides and conduction only through the base of the cask. Incident solar heat load was neglected in this model because it has a relatively modest impact on PCT, and that difference was judged small relative to the

other uncertainties in the planned test scenario. Use of a hot ambient air temperature was assumed to account for the contribution of solar insolation (see Section 2.5.2 for a further discussion).

2.2.5.1 Concrete Base

The conduction boundary condition at the external base of the TN-32B model includes thermal resistance equivalent to a 36-inch (0.91 m) thick concrete pad, to a representative uniform ground sink temperature. A ground temperature of 16°C (60°F) was assumed for this case.

2.2.5.2 External Convection Boundaries

Following the definition of external boundary conditions used in the COBRA-SFS model (see Section 2.1.3), convection boundaries were specified on the protective cover at the top of the cask and on the vertical cylindrical external surfaces. A heat transfer coefficient is defined at the convection boundaries, based on correlations for free convection from vertical flat plates and horizontal surfaces to surrounding still air (Table 7-2 in Holman 1997).

2.2.6 Thermal Gap Resistances

In the STAR-CCM+ model of the TN-32B, contact resistance boundaries were included consistent with the UFSAR and, where applicable, in the COBRA-SFS model. These included the following interfaces where helium properties were used to compute the gap resistance:

- Basket to rails
- Rails to inner confinement
- Basket to inner confinement
- Fuel compartments to basket plates
- Gaps between individual basket plates.

And the following interfaces where air properties were used:

- Cylindrical gamma shield to inner containment
- Base gamma shield to inner containment
- Protective cover attachment
- Lid inner and outer plates
- Shells to neutron shield aluminum containers.

The contact resistances at these interfaces were calculated based on the following equation (Incropera et al. 2007):

$$R = \frac{L}{k} \quad (2.1)$$

where

- R = contact resistance (m²-K/W)
- L = gap width (m)
- k = thermal conductivity of the fluid (W/m-K)

The gap width in each case was the value specified in the UFSAR. These gap widths appear reasonable given the component assembly, parts tolerances, and differences in thermal expansion (see the discussion of gap resistances for the COBRA-SFS model in Section 2.1.1).

2.2.7 Thermal Radiation Model

Surface-to-surface thermal radiation within the fuel basket region and thermal radiation from the external surfaces of the cask to the environment are included in the heat transfer evaluations with the STAR-CCM+ model. Table 2-1 lists the emissivity values for the solid surfaces in the model. The bulk of the interior surfaces are carbon steel that have been spray coated with aluminum. The stainless-steel sheets that form the fuel compartments are an exception to this, however. Apart from the active length of the fuel, which is treated by the effective thermal conductivity model (see Section 3.1), the surface properties only come into play in the short sections above and below the active length, where in the real system this space is occupied by the unheated ends of the fuel rods and the assembly end fittings.

Table 2-1. Emissivity values for radiation heat transfer.

Material	Emissivity
Carbon Steel	0.8
Exterior Painted Surfaces	0.9
Stainless Steel	0.3

Sensitivity studies on the effect of assumed emissivity values on temperatures and temperature distributions were not pursued in the initial modeling. However, variations were investigated in later work, since surface conditions of storage module components may differ from typical ranges, and also may change over the period of extended storage. This work is discussed in Section 2.5.2.

2.2.8 Fluid Models

There are two fluid continua in the STAR-CCM+ model, helium in the cask interior cavity and air contained between the top of the cask and the protective cover. Each is treated separately with independent flow model assumptions and properties. Since neither of the fluid regions communicate with an external pressure boundary, the gases were assigned a constant density and buoyancy forces were computed using the Boussinesq approximation (see Cuta et al. 2013, Section 3.4.1). Air density was computed using ambient temperature and atmospheric pressure. The helium density was computed assuming ambient temperature when filled and a 2230 mbar (223 kPa) initial pressure (UFSAR 2012).

The helium within the cask cavity is modeled assuming laminar flow, as was the air beneath the protective cover. Simulation results support these modeling assumptions.

2.3 Fuel Loading Map, Decay Heats and Axial Power Profile

From a list of 37 candidate fuel assemblies currently in the North Anna spent fuel pool with burnup values and other properties consistent with the needs of the Demonstration project, 32 fuel assemblies were ultimately selected for loading into the TN-32B cask. An iterative process was used that included various thermal analyses to support the cask loading plan. Figure 2-1 shows the proposed loading map for the basket, in a grid following the reference layout for the TN-32B cask. The map displays the assembly identification number (ID), based on the North Anna convention for tracking fuel assemblies in the spent fuel pool. Within each cell of the grid, the fuel cladding type is also identified, along with the assembly average burnup, initial fuel enrichment, and number of cycles in-core. The age of each assembly (in years since discharge) and the calculated decay heat values as of 7/31/2017 and 1/1/2027 are

also shown on the grid. These dates correspond to the assumed fuel loading date and the approximate end of the 10-year initial storage period. The loading map in Figure 2-1 includes the November 2014 modification where Assembly F40 was substituted for F52 (in basket cell #13), after it was determined that F52 was not a prototypic high burnup fuel assembly (i.e., it was a lead test assembly irradiated beyond normal operating conditions expected of typical high burnup fuel).

The values of decay heat shown in Figure 2-13 are the assembly decay heat estimates that were provided by Dominion for preliminary analyses. These are the values used by the utility in their operating procedures and are intentionally conservative. The estimated decay heat for assembly F40 was provided for initial loading (July 2017) only, as indicated in Figure 2-13, when this assembly was substituted for assembly F52. End of storage calculations used a scaled estimate of the F40 decay heat using the decrease in decay heat over the test period for assembly F52. The sum of decay heats for all assemblies is 36.8 kW for the July 2017 loading date and is estimated as 26 kW for the January 2027 end of test.

The assembly loading pattern and instrumentation layout was selected with the following goals:

1. Highest priority was to put assemblies with each of the four types of cladding in the four central cells of the basket to maximize clad temperature for each cladding (identified as basket cells 13, 14, 19, and 20)
2. Second priority was to put at least one assembly with M5[®] cladding, having higher burnup, shorter cooling time in a “middle corner” (i.e., basket cells 6, 9, 24, or 27) to maximize the range of storage temperatures over the test period
3. Assemblies arranged to yield a decay heat distribution pattern that is as symmetric as possible, given the limited number of fuel assemblies available and the constraints of items 1 and 2 above.

Thermocouple (TC) lance positions were selected such that two of the middle four assemblies and at least three peripheral assemblies are instrumented.

	1 6T0 Zirlo, 54.2 GWd 4.25%, 3cy, 11yr 1013/818W	2 (TC Lance) 3K7 M5, 53.4 GWd 4.55%, 3cy, 8yr 1167/837W	3 3T6 Zirlo, 54.3 GWd 4.25%, 3cy, 11yr 1015/820W	4 6F2 Zirlo, 51.9 GWd 4.25%, 3cy, 13yr 909/756W		
					DRAIN PORT	
5	3F6 Zirlo, 52.1 GWd 4.25%, 3cy, 13yr 914/761W	6 (TC Lance) 30A M5, 52.0 GWd 4.55%, 3cy, 6yr 1276/832W	7 22B M5, 51.2 GWd 4.55%, 3cy, 5 yr 1503/841W	8 20B M5, 50.5 GWd 4.55%, 3cy, 5 yr 1477/827W	9 5K6 M5, 53.3 GWd 4.55%, 3cy, 8yr 1163/834W	10 5D5 Zirlo, 55.5 GWd 4.2%, 3cy, 17yr 906/796W
11 Vent Port	5D9 Zirlo, 54.6 GWd 4.2%, 3cy, 17yr 885/778W	12 28B M5, 51.0 GWd 4.55%, 3cy, 5 yr 1496/837W	13 F40 Zirc-4, 50.6 GWd 3.59%, ?cy, 30yr 696W/not reported	14 (TC Lance) 57A M5, 52.2 GWd 4.55%, 3cy, 6yr 1281/834W	15 30B M5, 50.6 GWd 4.55%, 3cy, 5 yr 1482/830W	16 3K4 M5, 51.8 GWd 4.55%, 3cy, 8 yr 1120/803W
17	5K7 M5, 53.3 GWd 4.55%, 3cy, 8yr 1165/835W	18 50B M5, 50.9 GWd 4.55%, 3cy, 5 yr 1492/835W	19 (TC Lance) 3U9 Zirlo, 53.1 GWd 4.45%, 3cy, 10yr 1037/805W	20 0A4* Low-Sn Zy-4, 50 GWd 4.0%, 2cy, 22yr 725/664W	21 15B M5, 51.0 GWd 4.55%, 3cy, 5 yr 1496/837W	22 6K4 M5, 51.9 GWd 4.55%, 3cy, 8 yr 1121/804W
23	3T2 Zirlo, 55.1 GWd 4.25%, 3cy, 11yr 1036/837W	24 (TC Lance) 3U4 Zirlo, 52.9 GWd 4.45%, 3cy, 10yr 1031/801W	25 56B M5, 51.0 GWd 4.55%, 3cy, 5 yr 1495/837W	26 54B M5, 51.3 GWd 4.55%, 3cy, 5 yr 1511/846W	27 6V0 M5, 53.5 GWd 4.4%, 3cy, 8yrs 1178/843W	28 (TC Lance) 3U6 Zirlo, 53.0 GWd 4.45%, 3cy, 10yr 1035/803W
		29 4V4 M5, 51.2 GWd 4.40%, 3cy, 8yr 1073/787W	30 5K1 M5, 53.0 GWd 4.55%, 3cy, 8yr 1155/828W	31 (TC Lance) 5T9 Zirlo, 54.9 GWd 4.25%, 3cy, 11yr 1031/832W	32 4F1 Zirlo, 52.3 GWd 4.25%, 3cy, 13yr 918/764W	High Priority Assys

Figure 2-13. Final loading map proposed for Demonstration project (with assembly decay heat estimates provided by Dominion for 7/1/17 and 1/1/27). Note that M5[®] and ZIRLO[®] are registered trademarks.

Table 2-2 shows a summary of the final loading map, with TC lance locations indicated. This table repeats information shown in the grid in Figure 2-13, but also includes the calculated decay heat values as of January 2017, as well as the values for July 2017 and January 2027. The July 2017 decay heat values are significant, in that these values are assumed to correspond to the decay heat at the projected time of actual loading of the cask. These values are the main basis used for the thermal evaluations, the results of which are discussed in Sections 2.4 and 2.5.

Table 2-2. Summary of assembly loading map and projected decay heat values.

Cell #	TC Lance	Assembly ID	Cladding Type	Burnup [GWd/MTU]	Decay Heat [W], as of		
					January 2017	July 2017	January 2027
1		6T0	Zirlo	54.2	1033	1013	818
2	YES	3K7	M5	53.4	1210	1167	837
3		3T6	Zirlo	54.3	1035	1015	820
4		6F2	Zirlo	51.9	923	909	756
5		3F6	Zirlo	52.1	929	914	761
6	YES	30A	M5	52.0	1346	1276	832
7		22B	M5	51.2	1637	1503	841
8		20B	M5	50.5	1608	1477	827
9		5K6	M5	53.3	1206	1163	834
10		5D5	Zirlo	55.5	915	906	796
11		5D9	Zirlo	54.6	894	885	778
12		28B	M5	51.0	1629	1496	837
13 (as of 11/25/2014)		F40	Zirc-4	50.6	not provided	696	not provided
14	YES	57A	M5	52.2	1350	1281	834
15		30B	M5	50.6	1614	1482	830
16		3K4	M5	51.8	1162	1120	803
17		5K7	M5	53.3	1208	1165	835
18		50B	M5	50.9	1625	1492	835
19	YES	3U9	Zirlo	53.1	1063	1037	805
20		0A4	Low-Sn Zirc-4	50.0	729	725	664
21		15B	M5	51.0	1629	1496	837
22		6K4	M5	51.9	1162	1121	804
23		3T2	Zirlo	55.1	1056	1036	837
24	YES	3U4	Zirlo	52.9	1057	1031	801
25		56B	M5	51.0	1628	1495	837
26		54B	M5	51.3	1645	1511	846
27		6V0	M5	53.5	1221	1178	843
28	YES	3U6	Zirlo	53.0	1060	1035	803
29		4V4	M5	51.2	1109	1073	787
30		5K1	M5	53.0	1198	1155	828
31	YES	5T9	Zirlo	54.9	1051	1031	832
32		4F1	Zirlo	52.3	933	918	764

color coding:
 red font == assemblies in central 4 cells of basket
 blue font == assemblies on periphery of basket (16 cells)
 green font == assemblies in central 4x4 grid of basket, not including central 4 cells

Prior to receiving and completing the analysis of the detailed burnup data, the bounding axial decay heat profile for low-burnup fuel (DOE/RW-0472 1998) was used to define the axial decay heat profile for fuel assemblies loaded in the demonstration cask. In August 2014, a preliminary plot of end-of-life burnup from one assembly was provided for one of the assemblies that will be instrumented within the demonstration cask. Figure 2-14 shows this example profile, compared to the bounding profile from DOE/RW-0472. This comparison shows that the low-burnup profile is very similar to the measured profile from this high burnup assembly, except near the ends of the active fuel length. This suggests that using the low-burnup profile in these preliminary thermal evaluations probably does not have much effect on predicted PCTs for the fuel to be loaded into the TN-32B for the Demonstration project. However, the much larger differences near the ends of the rods, where the high-burnup profile is two to three times hotter than the low-burnup profile, show that temperatures predicted near the ends of the rods, and axial temperature distributions in basket components in general, have a much greater uncertainty in these analyses.

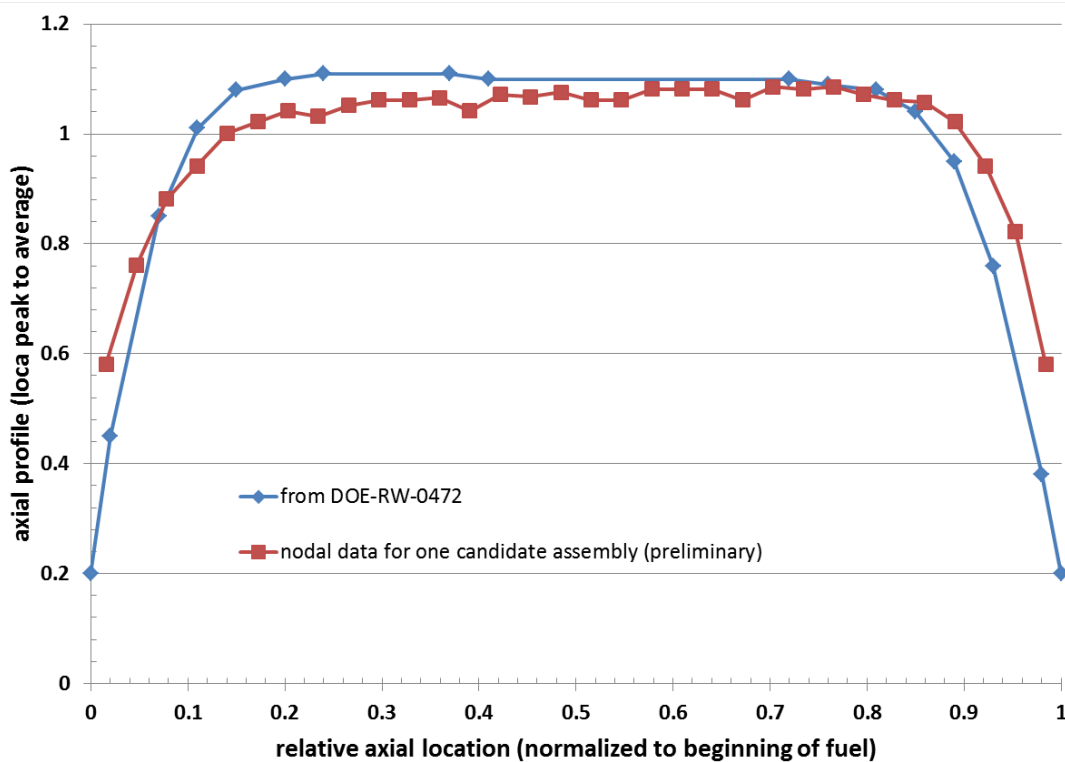


Figure 2-14. Bounding low-burnup axial decay heat profile from DOE/RW-0472 compared to preliminary axial burnup profile data obtained for one candidate fuel assembly in the Demonstration project.

2.4 COBRA-SFS Results

Results for the initial modeling of the cask in support of fuel assembly loading are shown here. Only results for the final selected loading map shown in Figure 2-13 are provided in this section of the report.

2.4.1 Initial Storage

Figure 2-15 and Figure 2-16 show the PCT and the minimum cladding temperature, respectively, for each assembly, as calculated using the conservative estimates of decay heat (with total of 36.8 kW) and preliminary inputs from the loading map in Figure 2-13.

These preliminary results show that at the beginning of the Demonstration project, an estimate of the maximum PCT is 315°C (598°F), on the hottest rod of fuel assembly 57A (in basket cell #14). The minimum cladding temperature on rods in this assembly is calculated as 157°C (315°F). The maximum/minimum temperature results for assembly 57A are based on an initial assembly decay heat of 1.281 kW at the projected time of loading in July 2017.

	270	284	279	267	
267	297	312	312	295	268
275	311	300	315	312	283
283	311	307	301	313	284
271	291	312	312	296	272
	273	284	281	268	

Figure 2-15. Assembly PCTs (°C) estimated with COBRA-SFS for conservative decay heats and initial storage conditions (total decay heat load 36.8 kW, as of 7/1/2017).

	156	156	156	156	
156	156	157	157	157	156
156	157	158	157	156	156
156	157	156	157	156	156
156	157	157	157	157	156
	158	156	155	156	

Figure 2-16. Assembly minimum cladding temperatures (°C) estimated with COBRA-SFS for conservative decay heats and initial storage conditions (total decay heat load 36.8 kW, as of 7/1/2017).

The radial distribution of peak component temperatures through the diameter of the cask, including the fuel assembly peak temperatures, is shown in Figure 2-17. The chart in this figure gives the temperature on each component at the axial location of the PCT. Figure 2-18 shows the axial distribution of temperature on the hottest rod in the hottest fuel assembly (57A), along with the axial temperature distribution on the coolest rod in this assembly. The hottest rod is located near the center of the rod array, and the coolest rod is located in the outer corner of the array, reflecting the radial distribution of temperature in the assembly. The same pattern is observed in all assemblies within the basket, with similar variation in the magnitude of the difference between the hottest rod and coolest rod in a given assembly. In general, assemblies at the periphery of the basket have slightly steeper radial temperature gradients than those in the center of the basket.

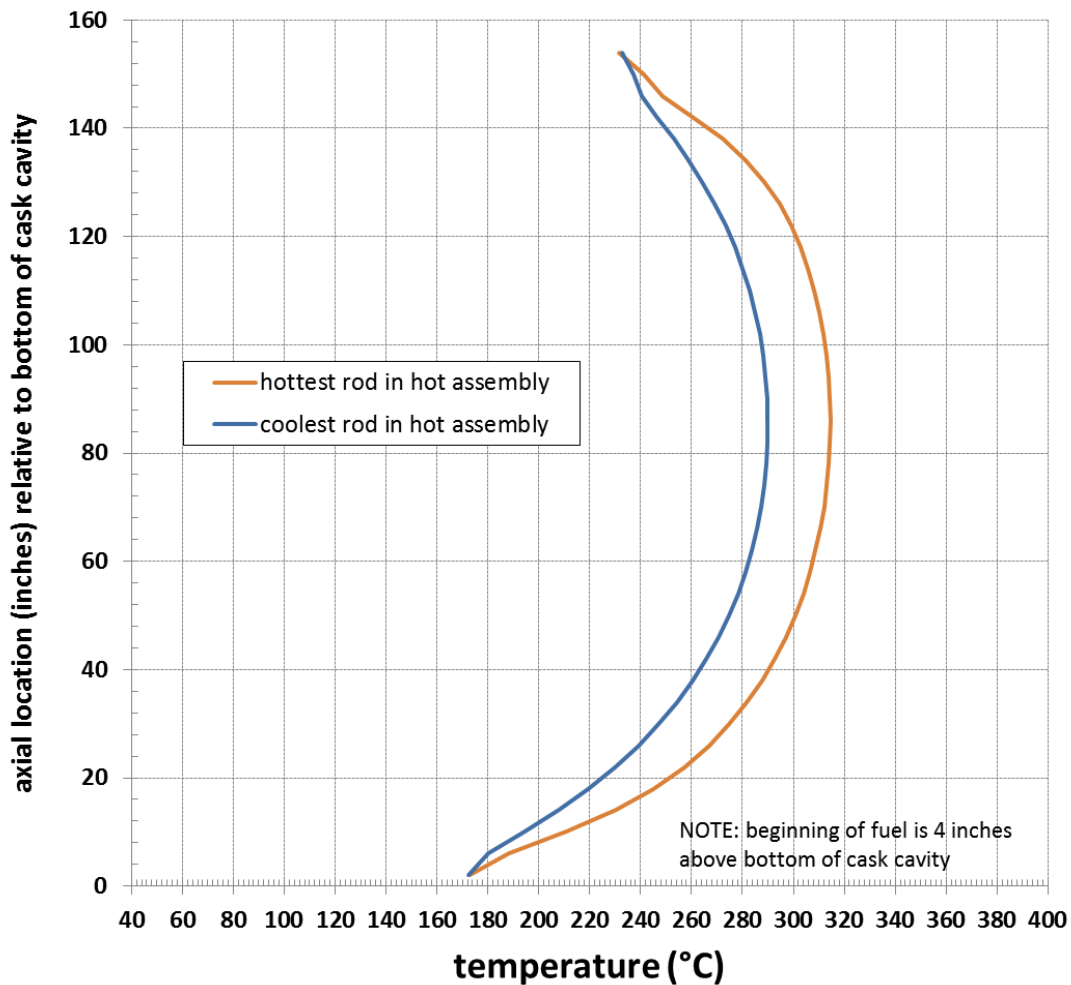


Figure 2-18. Axial distribution of temperature on hottest and coolest rods in the hottest assembly (57A) for initial storage conditions (conservative decay heats, as of July 2017).

Predicted axial temperature distributions on major cask components are shown in Figure 2-19. The peak basket temperature occurs on an inner basket plate of the cell enclosing the hottest assembly (as expected). The lowest basket temperatures, with the flattest profile, occur on the basket outer periphery. The axial profiles for the cavity liner, neutron shield resin radially averaged temperature, and neutron shield outer shell reflect the diminishing trend of the radial profile shown in Figure 2-17, and also illustrate the flattening of the axial profile in components farther from the decay heat source of the fuel.

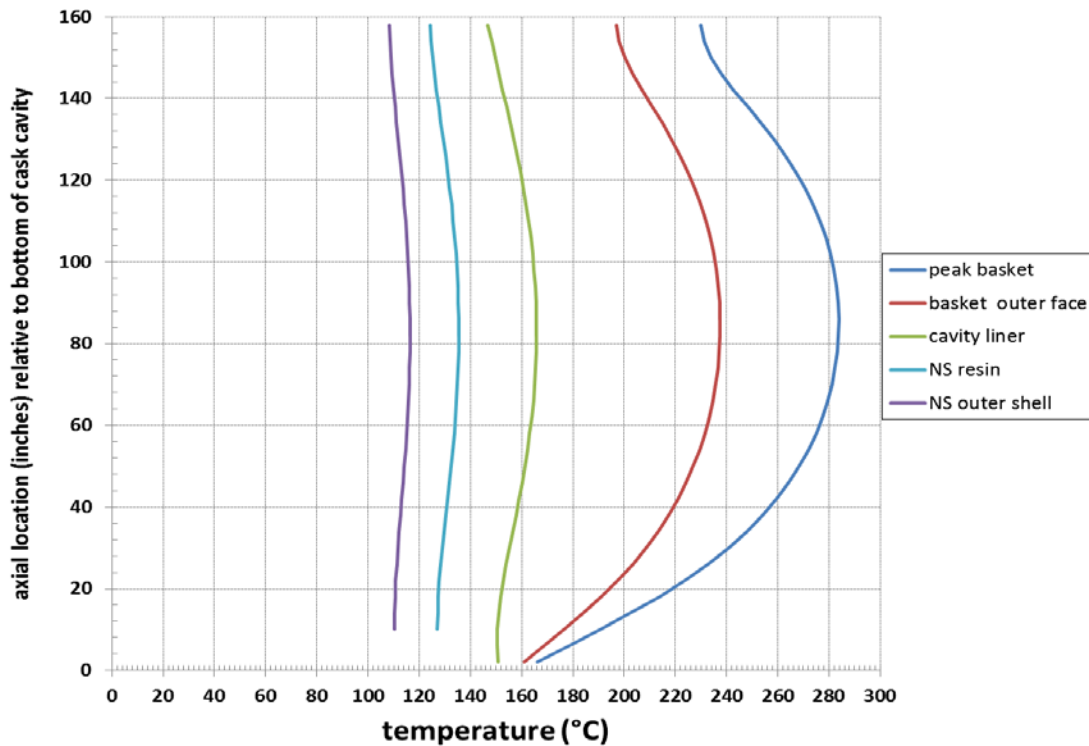


Figure 2-19. Axial temperature distributions on main components of TN-32B cask for initial storage conditions (conservative decay heats, as of July 2017).

2.4.2 Vacuum Drying Conditions

At this preliminary stage, information was not available on proposed vacuum drying operations for the TN-32B in the Demonstration project. Therefore, thermal evaluations for the vacuum drying transient have been performed for the bounding assumptions typically used in licensing basis evaluations. Specifically,

1. The ambient conditions external to the cask within the decontamination pit are assumed to allow unconstrained free convection to air at an ambient temperature of 38°C (100°F).
2. The initial conditions for the transient assume a uniform temperature distribution of 100°C (212°F) within the fuel and basket, as a bounding temperature for the fuel rods with water in the cask cavity.
3. The actual time required to drain the bulk of the water from the cavity and draw the cavity pressure down to the vacuum drying reference value (typically 3 torr or less), is ignored in the calculation. The system is assumed to be emptied of bulk water and reduced to the reference pressure “instantaneously” at the start of the transient.

With these conservative assumptions, a vacuum drying transient was performed using the COBRA-SFS model of the TN-32B, with initial loading based on the conservative July 2017 decay heat values described in Section 2.3. This calculation provides a bounding estimate of system temperatures during vacuum drying operations. Figure 2-20 shows the predicted PCT as a function of time for this bounding transient.

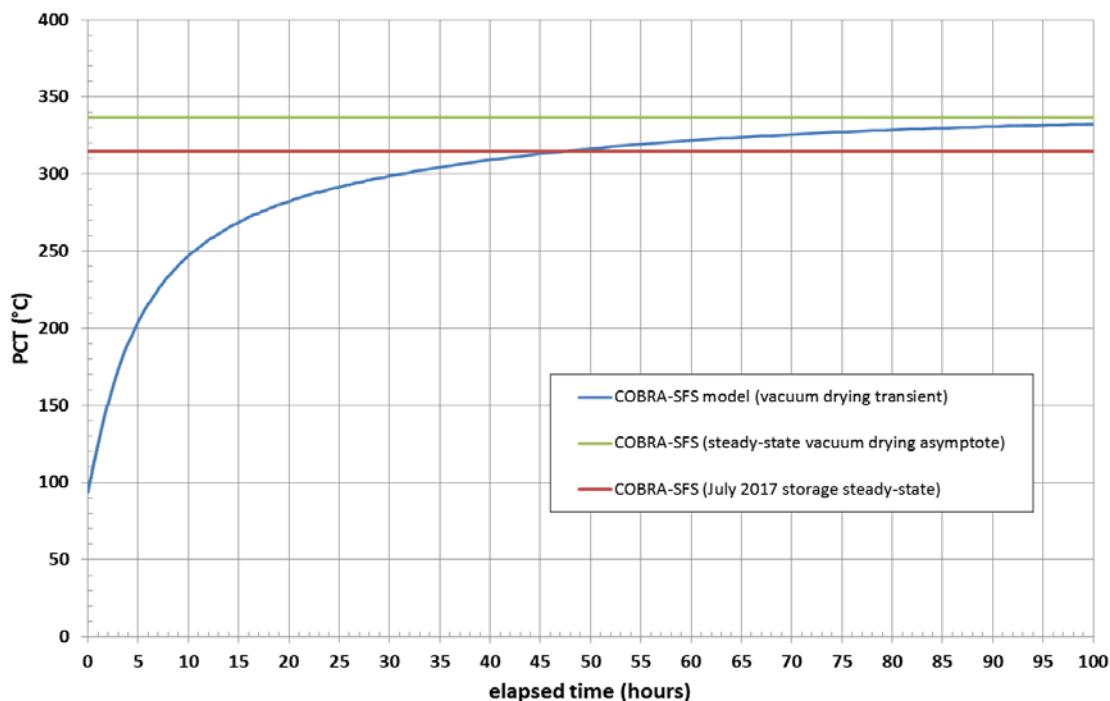


Figure 2-20. PCT as a function of time, calculated with COBRA-SFS model for bounding vacuum drying transient (conservative decay heats, as of July 2017).

The transient results for this bounding evaluation of the vacuum drying operation suggest that the PCT in vacuum drying may not be significantly greater than the PCT for storage conditions, and may be constrained to a lower value, due simply to the time-frame of the operation. It has been suggested that the vacuum drying time for the demonstration cask could be as short as 10 hours. The plot in Figure 2-20 shows that at 10 hours, a conservative estimate of the PCT would be only about 247°C (476°F).

Even if the actual vacuum drying transient is not that short for the demonstration cask, the requirements defined in the TN-32B UFSAR specifically limit vacuum drying time to no more than 36 hours at design-basis heat load of 32.7 kW, primarily due to thermal limits on non-fuel components of the cask. The predicted PCT for the transient evaluation for the demonstration cask is 305°C (582°F) at 36 hours, which is below the maximum value of 315°C (598°F) predicted for normal storage conditions. In this conservative bounding evaluation, it requires approximately 47 hours for the PCT to exceed the maximum value calculated for storage.

2.4.3 Storage Conditions after 10 Years

The final transmittal of decay heat distributions from Dominion did not include information on projected decay heat loads for assembly F40 at the end of the Demonstration project, as of 1/1/2027. Presumably, this is because the replacement of assembly F52 with F40 in basket cell #13 makes very little difference in the overall total decay heat. The effect of swapping out F52 for F40 is relatively small (a decrease of only 162 Watts at initial loading conditions projected as of July 2017), and within the uncertainty of the overall thermal evaluations, these two loading configurations have essentially the same thermal behavior. Therefore, the results presented here, for the configuration with F52, can be considered as representative of the results that would be expected for the final configuration with F40, after 10 years in storage. Figure 2-21 and Figure 2-22 show PCT and minimum cladding temperature, respectively, for each assembly.

	213	220	219	211	
211	228	234	234	228	213
218	234	239	240	234	219
220	234	238	235	234	219
214	227	234	234	228	213
	213	220	220	212	

Figure 2-21. Assembly PCTs (°C) estimated using conservative decay heats at end of 10 years in storage (with F52, as of January 2027).

	124	125	124	125	
125	125	125	125	125	124
124	125	125	125	125	124
125	125	124	125	125	124
125	125	125	125	125	124
	126	125	124	124	

Figure 2-22. Assembly minimum cladding temperatures (°C) estimated using conservative decay heats at end of 10 years in storage (with F52, as of January 2027).

These results show that at the end of the Demonstration project, an estimate of the maximum PCT is 240°C (463°F), on the hottest rod of fuel assembly 57A, with burnup 52.2 GWd/MTU, M5[®] cladding. The minimum cladding temperature on rods in this assembly is calculated as 124°C (255°F). This is based on an assembly decay heat of 834 W, calculated as of January 2027. These results are for the August 2014 loading pattern, with Assembly F52, and temperatures are slightly higher than what would be expected for the final loading configuration with F40.

2.4.4 Recirculation within the TN-32B Basket

The design of the TN-32B basket specifically excludes the possibility of thermo-siphon natural convection recirculation flow between the basket and the open channels of the support rails, since there is no open flow path at the base of the support rails, as discussed in Section 2.1.1. For the final loading pattern, and assembly decay heat distribution based on Dominion calculations (with total decay heat of 36.8 kW) the COBRA-SFS model predicts a very small convective circulation of the helium gas, with average exit velocity of 0.008 m/s (0.027 ft/s) from the fuel assemblies and -0.028 m/s (-0.091 ft/s) down the open regions in the support rails surrounding the basket. This is no more than a minor leakage flow in an unsealed system. Within the basket region, a small localized recirculation flow is predicted within some assemblies, near the mid-plane, where gas temperatures are highest, but these flows are not sustained over the full axial length of the assembly, and do not extend to global recirculation between adjacent assemblies. Figure 2-23 shows a plot of peak and minimum velocities predicted within the assemblies, based on the conservative assembly decay heat loading values from Dominion as of July 2017. In the legend to Figure 2-23, inlet and exit correspond to the bottom and top of the fuel assembly in each basket cell.

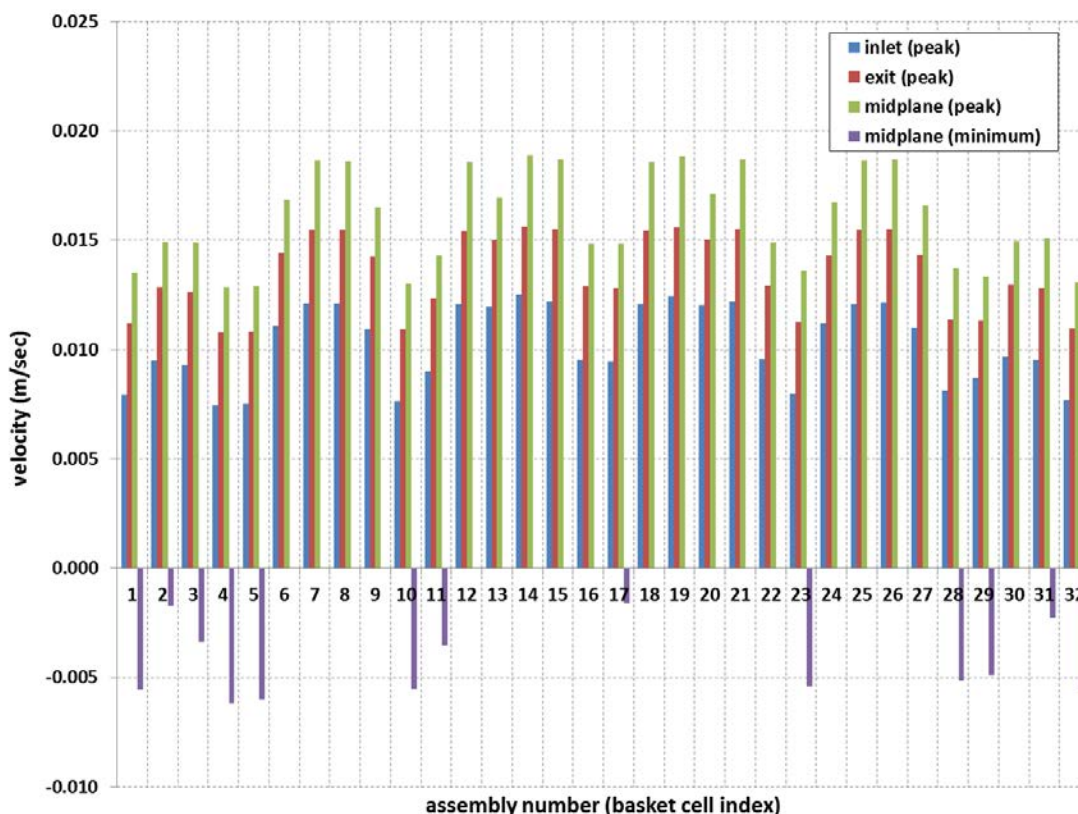


Figure 2-23. Helium gas velocities in TN-32B basket for initial storage conditions, predicted with COBRA-SFS model using rod-and-subchannel representation of fuel assemblies (based on 36.8 kW total decay heat load, as of 7/1/2017).

The velocities predicted for this cask geometry, where the design excludes the possibility of significant thermo-siphoning between the basket and support rail region, are quite low, as expected, and consequently the effect of heat transfer by convection in the cask is small. As shown in the discussion of vacuum drying conditions (see Section 2.4.2), the difference in predicted PCT for normal storage conditions (with nominal recirculation within the basket) and the vacuum drying asymptote (in which the effect of convection is entirely excluded), is only a small increase in the PCT (i.e., 315°C [599°F] for normal storage, and 336°C (637° F) predicted for the vacuum drying asymptote). As the system cools with age over the life of the Demonstration project, the thermal gradients driving this minor recirculation will tend to flatten, and the contribution of convection to heat transfer in the basket will decrease further, becoming even more insignificant over time.

2.4.5 Summary of Clad Temperature Distribution

In addition to the initial estimates of peak and minimum cladding temperatures reported in Section 2.4.1, the overall distribution of temperature on the fuel rods throughout the demonstration cask is included here. The overall distribution of temperature throughout the 32 assemblies of the basket was captured by means of cataloging the temperatures to indicate the fraction of the cladding surface that is expected to be within a given range. Figure 2-24 shows the distribution for the hottest assembly (as per the July 2017 loading). This plot indicates that approximately 56% of the cladding surface is in the temperature range 250-300°C (482-572°F), with only about 20% in the temperature range 300-350°C (572-662°F). About

20% of the cladding is in the range 200-250°C (392-482°F), and only about 6% of the cladding surface is at the lowest temperature range, between 150-200°C (302-392°F).

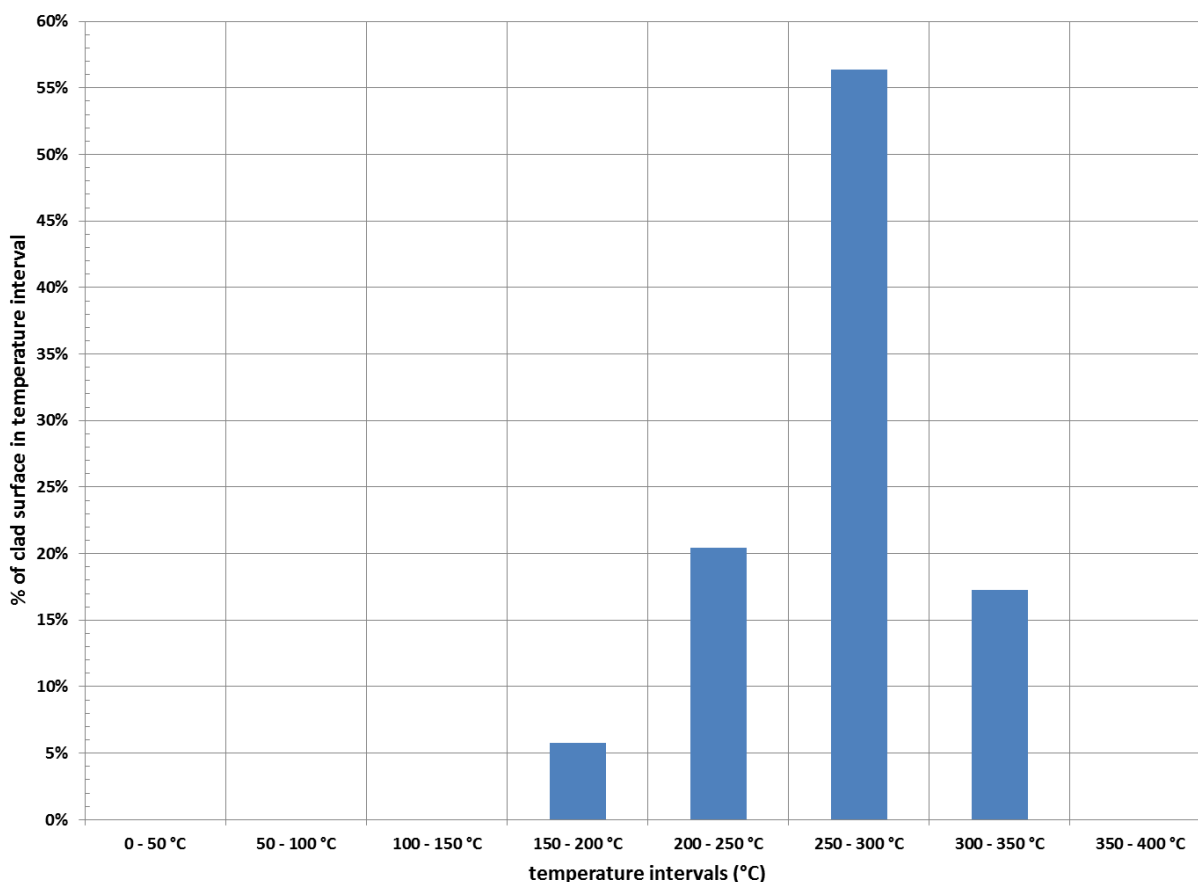


Figure 2-24. Temperature distribution ranges in the hottest assembly (57a in cell #14), from cladding temperatures predicted with COBRA-SFS model for conservative decay heats and initial loading conditions (as of 7/1/2017)

As the fuel assemblies continue to cool during the planned 10-year duration of the Demonstration project, the temperatures on the fuel rods will decrease, and the axial profiles will tend to flatten. This can be seen in the plot in Figure 2-25, for the assumed decrease in conservative decay heat values by 2027. In this parsing of the cladding surface temperature predictions obtained with the COBRA-SFS model, nearly 66% of the cladding is expected to be in the temperature range of 200-250°C (392-482°F) by 2027. About 30% is expected to be in the range 150-200°C (302-392°F), and approximately 5% is expected to be in the range of 100-150°C (100-302°F).

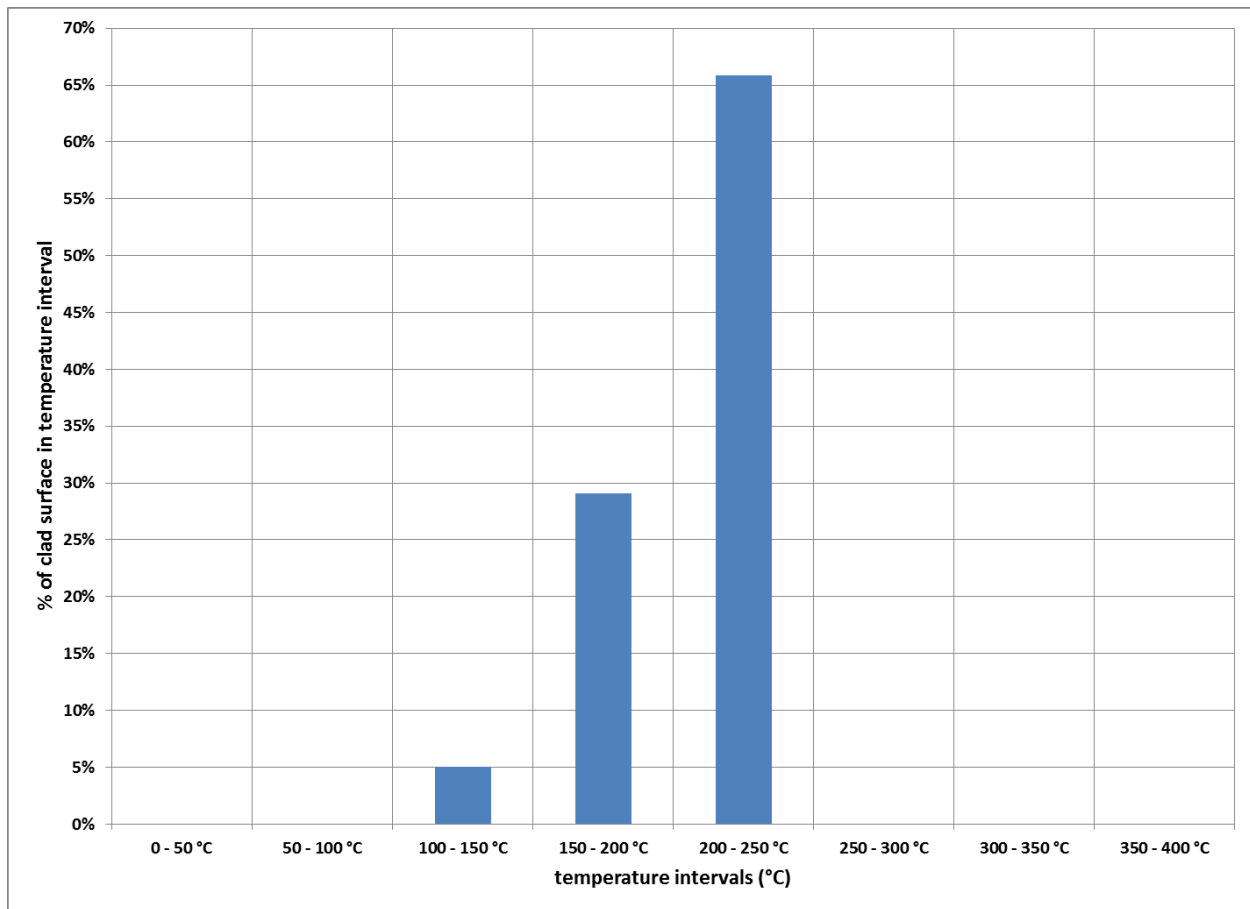


Figure 2-25. Temperature distribution ranges in the hottest assembly (57a in cell #14) after 10 years (1/1/2027), from cladding temperatures predicted with COBRA-SFS model using conservative decay heats

Considering the temperatures predicted for all rods in all assemblies in the basket, Figure 2-26 shows the overall predicted distribution ranges for the initial decay heat loading (as of 7/1/2017). Approximately 50% of the cladding surface is expected to be in the temperature range 250-300°C (482-572°F). Only about 6% of the total cladding surface is likely to be above 300°C (572°F), in the temperature range 300-350°C (572-662°F). Since the PCT is predicted to be only 315°C (599°F), this “bin” is effectively only 300-315°C (572-555°F), and does not actually extend to temperatures as high as 350°C (572°F). Approximately 37% of the cladding surface is expected to be in the range 200-250°C (392-482°F), and about 9% is predicted to begin the demonstration test in the coolest range of 150-200°C (302-392°F).

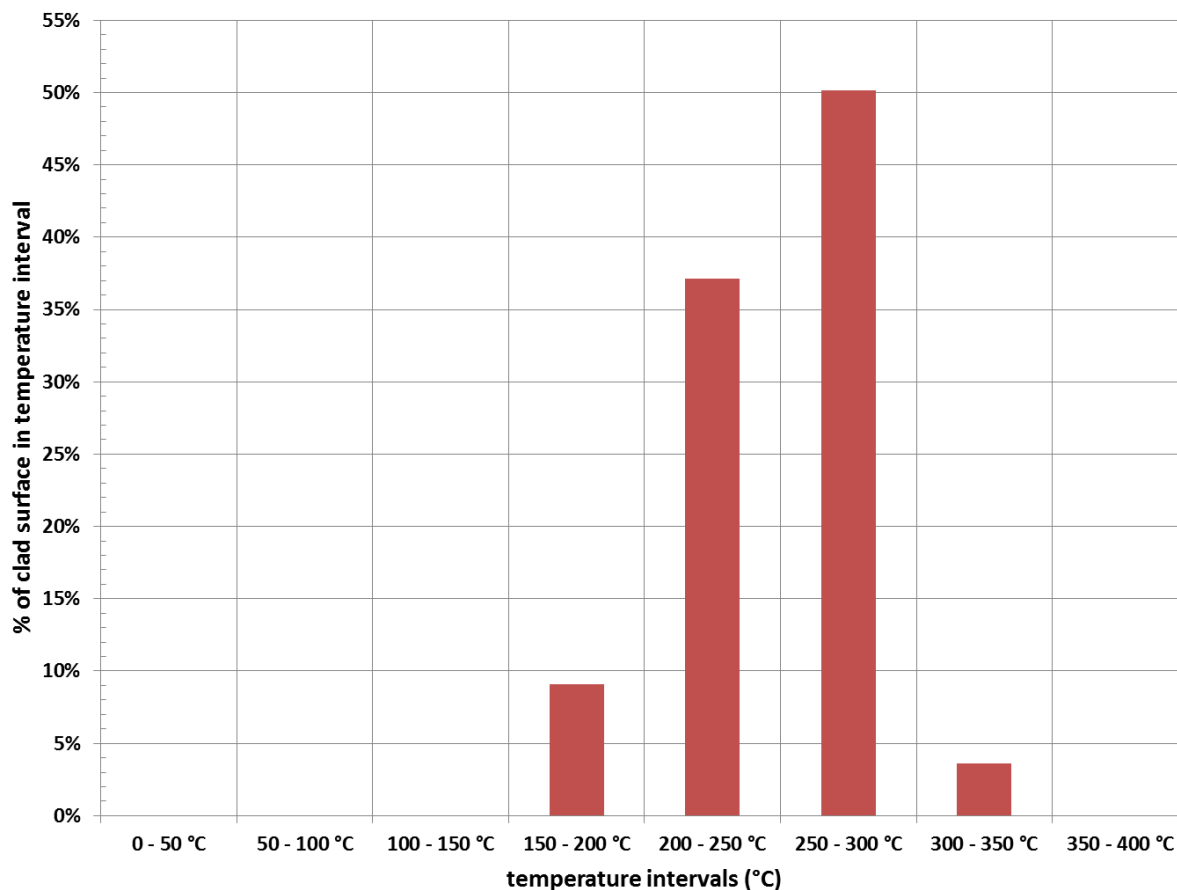


Figure 2-26. Temperature distribution ranges for all fuel assemblies in the TN-32B basket, from cladding temperatures predicted with COBRA-SFS model for initial loading conditions (with F40, as of 7/1/2017).

2.5 STAR-CCM+ Results

Results for the initial modeling with STAR-CCM+ for the final selected loading map and conservative decay heats in Section 2.3 are provided in this section.

2.5.1 Initial Storage

Figure 2-27 shows the PCT for each assembly, from the STAR-CCM+ model, as calculated using the conservative estimates of decay heat and preliminary inputs.

These preliminary results show that at the beginning of the Demonstration project, an estimate of the maximum PCT is 325°C (617°F), which occurs on the hottest rods of fuel assemblies 30B and 15B (in basket cells #15 and 21). Assembly 30B is adjacent to the hot assembly indicated by the COBRA-SFS model, however PCTs for all three assemblies are all within 1°C (1.8°F) in the STAR-CCM+ model. The conservative estimates of decay heats for these assemblies are 1.482 kW and 1.496 kW for 30B and 15B, respectively. The decay heat for 57A is somewhat lower at 1.281 kW, however it is positioned closer to the center of the basket.

	257	287	281	252	
262	298	320	319	294	262
281	324	303	324	325	291
292	325	315	304	325	291
268	290	320	320	295	268
	291	287	282	253	

Figure 2-27. Assembly PCTs (°C) estimated with STAR-CCM+ for conservative decay heats and initial storage conditions (total decay heat load 36.8 kW, as of 7/1/2017).

Minimum cladding temperatures are not presented here because these occur at rod ends, which are not included in the STAR-CCM+ model.

2.5.2 Sensitivity of Results to Solar Heat Loading

As stated previously (see Section 2.2.5) the assumption in models with both codes is to neglect the influence of insolation. Experience has shown this to have a small effect on PCT, and the conservative use of the hot ambient temperature in the external surface boundary condition is expected to effectively account for solar heat loading. This is reasonable for cladding temperature predictions. However, the predicted peak temperature in the neutron shield material is already near the thermal limit and inclusion of insolation may therefore be significant. This is especially true for the preliminary model using conservative decay heat values.

The UFSAR states that the temperature limit for the neutron shield resin is 149°C (300°F). Table 2-3 shows a comparison of peak temperature in the lid and radial neutron shield material with and without regulatory¹ solar insolation and a 38°C (100°F) ambient. Credit is not taken for the solar absorptivity value of the cask surface, which would lessen this difference. However, these results indicate that, for decay heats estimated for the initial loading, the material limit could be exceeded in the upper lid neutron shield.

Table 2-3. Peak neutrons Shield temperature with and without regulatory solar insolation.

Neutron Shield	T _{max} w/o solar, °C	T _{max} w/ solar, °C
circumferential	137.0	146.5
upper lid	148.8	158.6

The corresponding increase in peak fuel cladding temperature is 9°C, from 325°C without insolation to 334°C with insolation, with no other changes.

It should be emphasized that, while this analysis indicates it is possible to exceed the material limit for the lid neutron shield, several conservative assumptions make it unlikely to occur. First, and most importantly, this preliminary calculation was performed using a conservative estimate of total decay heat^m. Second, the assumption that all the incident solar flux is absorbed is very conservative, as normally a reduction due to solar absorptivity is applied. Also, this is treated in a steady-state calculation as a bounding 12-hour solar heat load, averaged over 24 hours. In actual conditions of service, the solar

¹ As specified for normal conditions under 10CFR71.71 (10CFR71 2003).

^m A refined decay heat estimate of 32.9 kW using ORIGEN calculations was provided by Dominion with the Demonstration Test license amendment request. See ML16272A380.pdf on NRC ADAMS website. This was a significant reduction from the 36.8 kW conservative estimate used in the initial modeling described here.

heat load would be much more variable, and probably much lower. In addition, the normal diurnal cycle would also add protection against this limit.

3. BEST ESTIMATE UPDATES TO PLANNING MODELS

This section describes refinements to model inputs that were included to provide more accurate estimates of fuel and cask component temperatures. The model inputs were updated to include proprietary fuel geometry from the fuel vendors and decay heat estimates from Oak Ridge National Laboratory (ORNL). With these revisions, the models represent the fuel assemblies actually loaded into the Demonstration cask and are therefore referred to as best estimate models.

The updated inputs are described in Sections 3.1 through 3.3 and updated model results follow in Sections 3.4 and 3.5. The results sections parallel those for the preliminary model results in Section 2.

3.1 Fuel Assembly Geometry and Decay Heats

For the results presented in Section 3.4, the COBRA-SFS model used fuel assembly geometry information for Westinghouse NAIF P+Z, Westinghouse NAIF, and Framatome AMBW fuel assemblies, provided after completion of the NDAs with the fuel vendors and utility. For the STAR-CCM+ model, the k-effective model for WE 17x17 fuel used to represent the homogenized fuel region is bounding for all of these fuel assembly designs (see Section 2.2.4). Therefore, this input was unchanged in the best estimate model. Both the COBRA-SFS model and the STAR-CCM+ model, however, incorporated the updated assembly decay heat values and decay heat distributions developed to replace the conservative estimates initially provided by the utility.

The updated assembly decay heat values are based on detailed calculations with ORIGEN (Gauld et al. 2009) performed at ORNL in August 2015, taking into account pin-by-pin burnup and assembly cycle history provided under the final NDAs with the fuel vendors and the site operator (Dominion). The total decay heat in the cask is calculated as 30.6 kW as of 7/31/2017, and 22.7 kW as of 1/1/2027. The loading map with the updated estimates of decay heat is shown in Figure 3-1. The information contained in Figure 3-1 is also presented in tabular form in Table 3-1.

	1 6T0 Zirlo, 54.2 GWd 4.25%, 3cy, 11yr 907 / 727 W	2 (TC Lance) 3K7 M5, 53.4 GWd 4.55%, 3cy, 8yr 983 / 749 W	3 3T6 Zirlo, 54.3 GWd 4.25%, 3cy, 11yr 909 / 729 W	4 6F2 Zirlo, 51.9 GWd 4.25%, 3cy, 13yr 793 / 653 W	DRAIN PORT
5 3F6 Zirlo, 52.1 GWd 4.25%, 3cy, 13yr 795 / 653 W	6 (TC Lance) 30A M5, 52.0 GWd 4.55%, 3cy, 6yr 1039 / 746 W	7 22B M5, 51.2 GWd 4.55%, 3cy, 5 yr 1170 / 754 W	8 20B M5, 50.5 GWd 4.55%, 3cy, 5 yr 1149 / 741 W	9 5K6 M5, 53.3 GWd 4.55%, 3cy, 8yr 977 / 745 W	10 5D5 Zirlo, 55.5 GWd 4.2%, 3cy, 17yr 806 / 668 W
11 Vent Port 5D9 Zirlo, 54.6 GWd 4.2%, 3cy, 17yr 795 / 660 W	12 28B M5, 51.0 GWd 4.55%, 3cy, 5 yr 1162 / 750 W	13 F40 Zirc-4, 50.6 GWd 3.59%, 3cy, 30yr 463 / 397 W	14 (TC Lance) 57A M5, 52.2 GWd 4.55%, 3cy, 6yr 1047 / 752 W	15 30B M5, 50.6 GWd 4.55%, 3cy, 5 yr 1152 / 744 W	16 3K4 M5, 51.8 GWd 4.55%, 3cy, 8 yr 944 / 718 W
17 5K7 M5, 53.3 GWd 4.55%, 3cy, 8yr 979 / 746 W	18 50B M5, 50.9 GWd 4.55%, 3cy, 5 yr 1159 / 747 W	19 (TC Lance) 3U9 Zirlo, 53.1 GWd 4.45%, 3cy, 10yr 918 / 724 W	20 0A4 Low-Sn Zy-4, 50 GWd 4.0%, 2cy, 22yr 641 / 541 W	21 15B M5, 51.0 GWd 4.55%, 3cy, 5 yr 1163 / 750 W	22 6K4 M5, 51.9 GWd 4.55%, 3cy, 8 yr 944 / 717 W
23 3T2 Zirlo, 55.1 GWd 4.25%, 3cy, 11yr 929 / 744 W	24 (TC Lance) 3U4 Zirlo, 52.9 GWd 4.45%, 3cy, 10yr 912 / 719 W	25 56B M5, 51.0 GWd 4.55%, 3cy, 5 yr 1161 / 749 W	26 54B M5, 51.3 GWd 4.55%, 3cy, 5 yr 1162 / 759 W	27 6V0 M5, 53.5 GWd 4.4%, 3cy, 8yrs 989 / 756 W	28 (TC Lance) 3U6 Zirlo, 53.0 GWd 4.45%, 3cy, 10yr 915 / 721 W
	29 4V4 M5, 51.2 GWd 4.40%, 3cy, 8yr 915 / 709 W	30 5K1 M5, 53.0 GWd 4.55%, 3cy, 8yr 970 / 740 W	31 (TC Lance) 5T9 Zirlo, 54.9 GWd 4.25%, 3cy, 11yr 922 / 738 W	32 4F1 Zirlo, 52.3 GWd 4.25%, 3cy, 13yr 798 / 656 W	

Figure 3-1. Final loading map proposed for Demonstration project.

Table 3-1. Summary of assembly loading map and projected decay heat values.

Cell #	TC Lance	Assembly ID	Cladding Type	Burnup [GWd/MTU]	Decay Heat [W], as of	
					July 31, 2017	January 1, 2027
1		6T0	Zirlo®	54.2	907	727
2	YES	3K7	M5®	53.4	983	749
3		3T6	Zirlo®	54.3	909	729
4		6F2	Zirlo®	51.9	793	653
5		3F6	Zirlo®	52.1	795	653
6	YES	30A	M5®	52.0	1039	746
7		22B	M5®	51.2	1170	754
8		20B	M5®	50.5	1149	741
9		5K6	M5®	53.3	977	745
10		5D5	Zirlo®	55.5	806	668
11		5D9	Zirlo®	54.6	795	660
12		28B	M5®	51.0	1162	750

Cell #	TC Lance	Assembly ID	Cladding Type	Burnup [GWd/MTU]	Decay Heat [W], as of	
					July 31, 2017	January 1, 2027
13		F40	Zirc-4	50.6	463	397
14	YES	57A	M5 [®]	52.2	1047	752
15		30B	M5 [®]	50.6	1152	744
16		3K4	M5 [®]	51.8	944	718
17		5K7	M5 [®]	53.3	979	746
18		50B	M5 [®]	50.9	1159	747
19	YES	3U9	Zirlo [®]	53.1	918	724
20		0A4	Low-Sn Zirc-4	50.0	641	541
21		15B	M5 [®]	51.0	1163	750
22		6K4	M5 [®]	51.9	944	717
23		3T2	Zirlo [®]	55.1	929	744
24	YES	3U4	Zirlo [®]	52.9	912	719
25		56B	M5 [®]	51.0	1161	749
26		54B	M5 [®]	51.3	1162	759
27		6V0	M5 [®]	53.5	989	756
28	YES	3U6	Zirlo [®]	53.0	915	721
29		4V4	M5 [®]	51.2	915	709
30		5K1	M5 [®]	53.0	970	740
31	YES	5T9	Zirlo [®]	54.9	922	738
32		4F1	Zirlo [®]	52.3	798	656

color coding:
red font == assemblies in central 4 cells of basket
blue font == assemblies on periphery of basket (16 cells)
green font == assemblies in central 4x4 grid of basket, not including central 4 cells

3.2 Axial Decay Heat Distribution

The axial decay heat distribution for a spent fuel assembly is essentially the axial burnup distribution, since this determines the distribution of heat-generating activated elements in the fuel rods. Uncertainty in the axial decay heat input to thermal evaluations contributes to uncertainty in the peak temperatures on the fuel rods, and uncertainty in the axial distribution of temperature, for the rods and throughout the cask structures. For the updated results presented in Section 3.4, the COBRA-SFS model used axial decay heat distributions determined from the detailed pin-by-pin calculations performed by ORNL in August 2015. The updated results in Section 3.5 for the STAR-CCM+ model used an axial decay heat distribution averaged over all 32 assemblies, based on the results of the ORNL calculations.

Figure 3-2 shows the assembly average profile determined for each of the 32 assemblies to be loaded into the demonstration cask. As shown in this plot, the axial profiles are very similar for all assemblies. For comparison, the plot in Figure 3-2 also includes the standard bounding profile for low-burnup fuel (DOE/RW-0472 1998) that was used for the initial calculations presented in Section 2. As shown, the low-burnup bounding profile has essentially the same peaking factor as the higher burnup fuel assemblies to be loaded in the demonstration cask. The only significant difference is the “fall-off” of decay heat near the ends of the active fuel region, which is somewhat steeper in the low-burnup profile. The main effect of this difference would be slightly higher temperatures near the ends of the active length of higher

burnup fuel rods, compared to lower burnup rods, but the peak temperatures would be expected to be essentially the same, for the same decay heat.

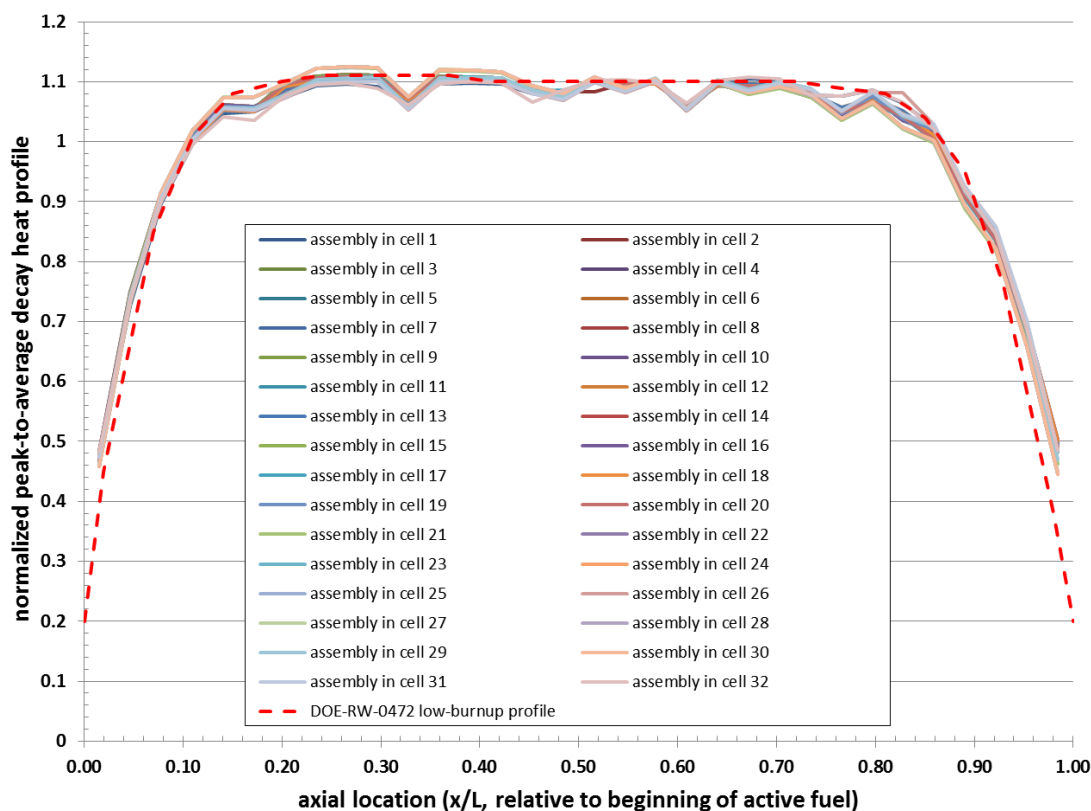


Figure 3-2. Axial decay heat profiles per assembly, from detailed pin-by-pin decay heat calculations, compared to bounding low-burnup axial decay heat profile from DOE/RW-0472.

As a simplifying assumption, the STAR-CCM+ model used a single average profile for all assemblies. Figure 3-3 compares this average profile to the maximum and minimum profiles (based on the maximum and minimum normalized peaking factor for all 32 axial decay heat profiles). This plot shows that the difference between the maximum and minimum profile is within the uncertainty in the calculation, and the average value is a reasonable approximation for all assemblies, for the homogenized representation of the fuel assemblies in the STAR-CCM+ model. As noted above, the detailed representation of the fuel assemblies in the COBRA-SFS model used axial decay heat distributions determined from detailed pin-by-pin calculations for each assembly.

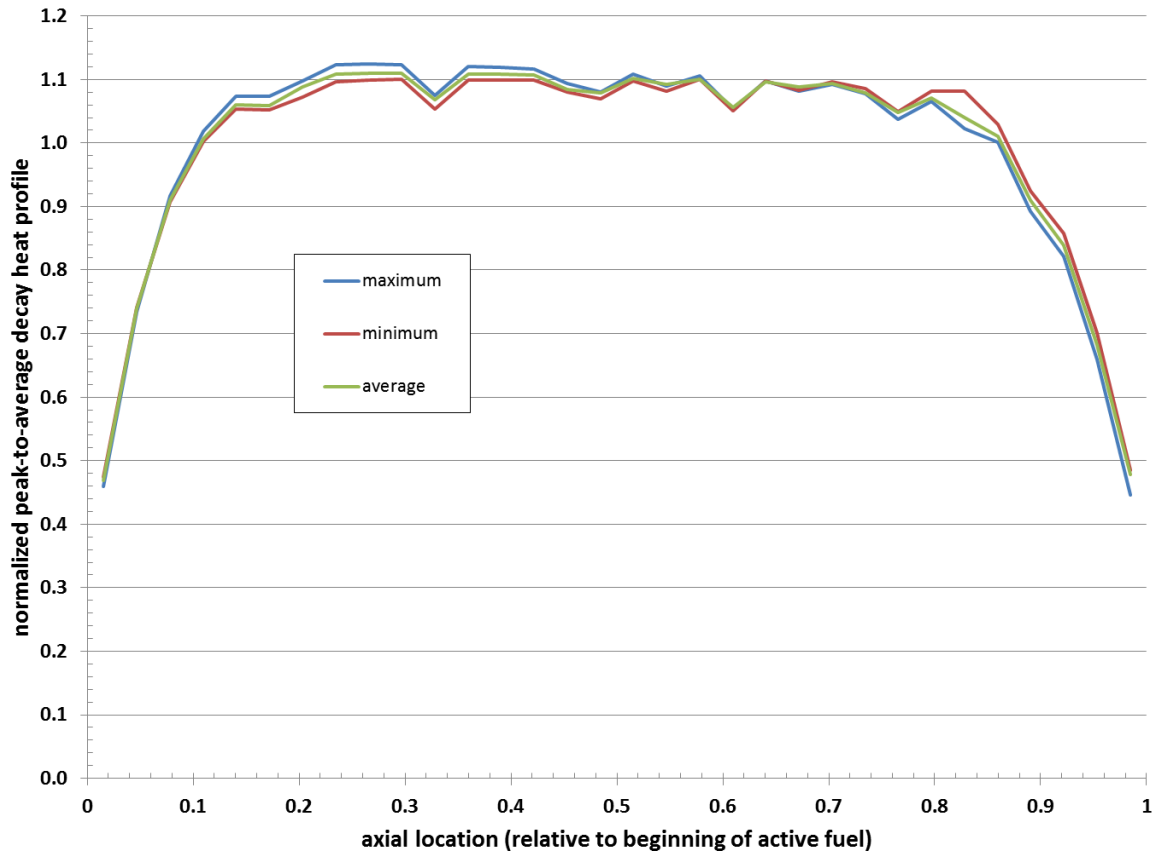


Figure 3-3. Maximum, minimum, and average axial decay heat profiles per assembly, from detailed pin-by-pin decay heat calculations.

3.3 Additional Model Updates

Beyond updates to the fuel decay heat and geometry described in Sections 3.1 and 3.2, model inputs and boundary conditions were the same as those used in the preliminary models. One exception was the surface emissivities used in the STAR-CCM+ model. These were changed from values used in the preliminary models (Table 2-1) to be consistent with values used in the COBRA-SFS model. The surface emissivity values that were used in the updated models are listed in Table 3-2.

Table 3-2. Updated emissivity values for radiation heat transfer.

Material	Emissivity
Carbon Steel	0.45
Exterior Painted Surfaces	0.9
Aluminum	0.2
Stainless Steel	0.3

3.4 COBRA-SFS Thermal Modeling Results

The individual assembly total decay heats shown in Figure 3-1 for the final proposed loading pattern with a total decay heat estimated as 30.6 kW as of 7/31/2017 were used to obtain the updated results presented here. Section 3.4.1 presents the peak and minimum clad temperatures calculated with the COBRA-SFS model for this loading configuration as of the planned beginning of the demonstration in July 2017. Section 3.4.2 compares axial temperature profiles at proposed thermocouple locations with hot fuel rod temperature profiles in the same assembly. Section 3.4.3 presents a transient and bounding steady-state evaluation of expected cladding temperatures for vacuum drying conditions. Section 3.4.4 discusses the expected temperatures for this loading pattern at the end of the planned 10-year span of the Demonstration project. Section 3.4.5 describes the distribution of temperature by cladding surface area, for planned initial loading conditions as of July 2017. Section 3.4.6 summarizes relative effect on PCT of changes in model inputs, including boundary conditions, decay heat, axial power profile, and fuel geometry.

3.4.1 Initial Storage Conditions

Figure 3-4 and Figure 3-5 show the PCT and the minimum cladding temperature, respectively, for each assembly, as calculated for the final proposed loading pattern in Figure 3-1.

	238	247	244	234	
234	257	269	268	256	235
241	268	255	271	269	246
247	268	268	260	269	247
238	255	269	269	257	238
	239	248	246	235	

Figure 3-4. Assembly PCT (°C) estimated for initial storage conditions (as of 7/31/2017).

	138	138	138	138	
138	138	138	138	138	138
138	138	139	138	138	138
138	138	139	139	138	138
138	139	138	138	138	138
	139	138	138	138	

Figure 3-5. Assembly minimum cladding temperatures (°C) estimated for initial storage conditions (as of 7/31/2017).

These results show that at the beginning of the Demonstration project, a reasonable estimate of the maximum PCT is 271°C (519°F), on the hottest rod of fuel assembly 57A (in basket cell #14). The minimum cladding temperature on rods in this assembly is calculated as 138°C (280°F).

The radial distribution of component temperatures through the diameter of the cask at the axial location of the PCT, including the fuel assembly peak temperatures, is shown in Figure 3-6. The key diagram in this figure indicates the specific components captured on this radial line. Figure 3-7 shows the axial distribution of temperature on the hottest rod in the hottest fuel assembly (57A), along with the axial temperature distribution on the coolest rod in this assembly. The hottest rod is located near the center of the rod array, and the coolest rod is located in the outer corner of the array, reflecting the radial distribution of pin-by-pin decay heat in the assembly, and the simple fact that the walls of the basket enclosing the assembly are the coolest temperatures seen by the rod array for conduction and thermal radiation heat transfer. The same pattern is observed in all assemblies within the basket, with similar variation in the magnitude of the difference between the hottest rod and coolest rod in a given assembly.

In general, assemblies at the periphery of the basket have slightly steeper radial temperature gradients than those in the center of the basket.

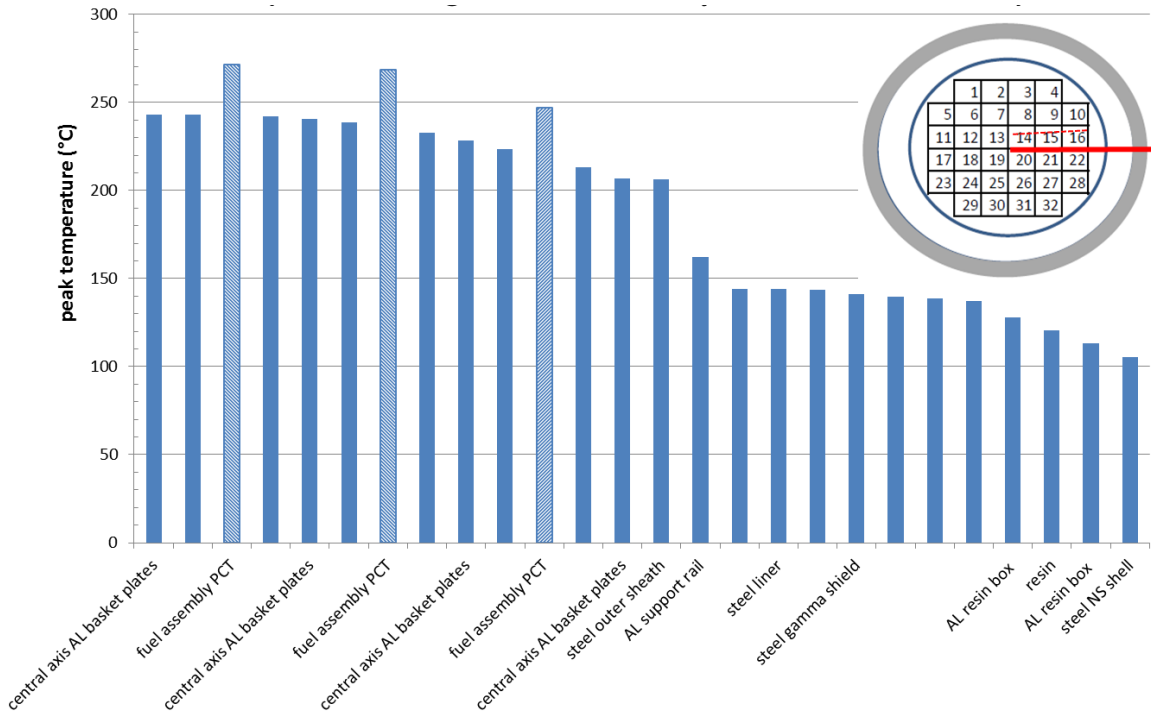


Figure 3-6. Radial distribution of system component temperatures at the axial location of PCT for initial storage conditions (as of 7/31/2017).

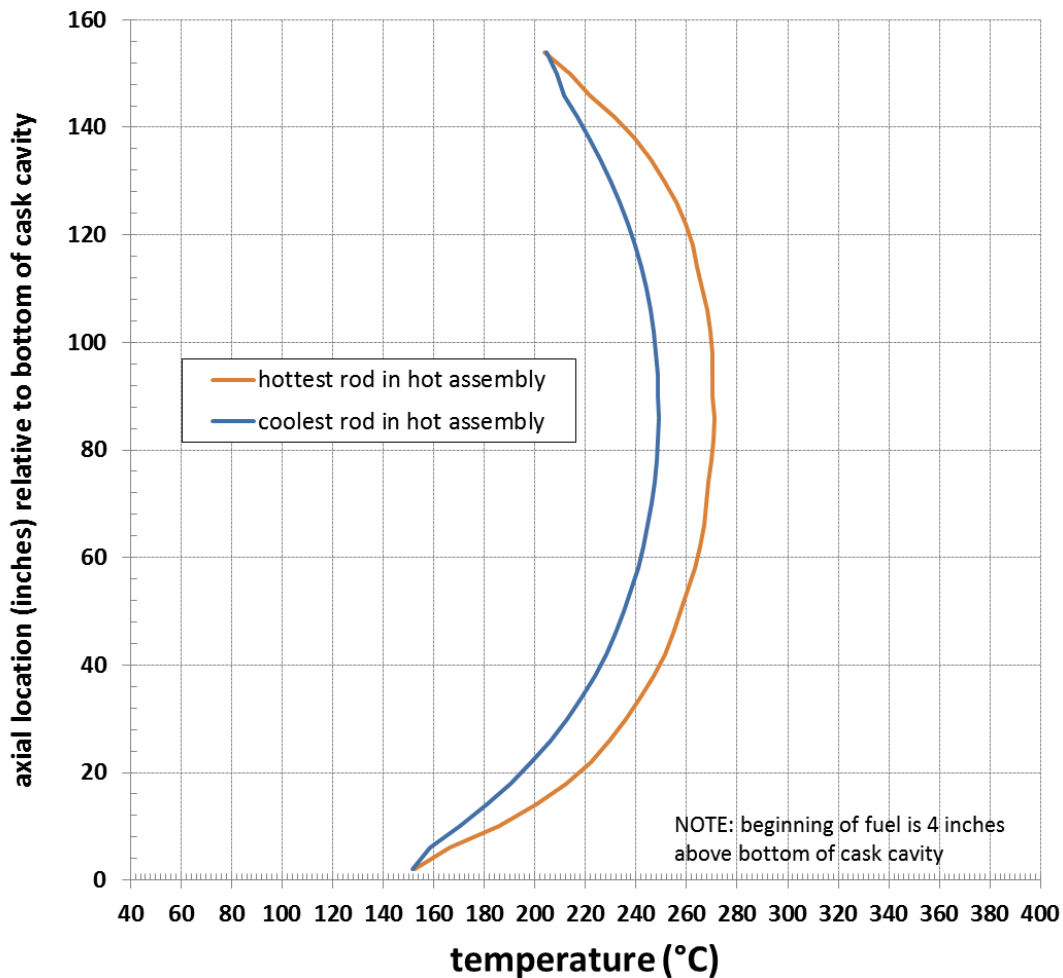


Figure 3-7. Axial distribution of temperature on hottest and coolest rods in the hottest assembly (57A) for initial storage conditions (as of 7/31/2017).

Predicted axial temperature distributions on major cask components are shown in Figure 3-8. The peak basket temperature occurs on an inner basket plate of the cell enclosing the hottest assembly (as expected). The lowest basket temperatures, with the flattest profile, occur on the basket outer periphery. The axial profiles for the cavity liner, neutron shield resin radially averaged temperature, and neutron shield outer shell reflect the diminishing trend of the radial profile shown in Figure 3-6, and also illustrate the flattening of the axial profile in components farther from the decay heat source of the fuel.

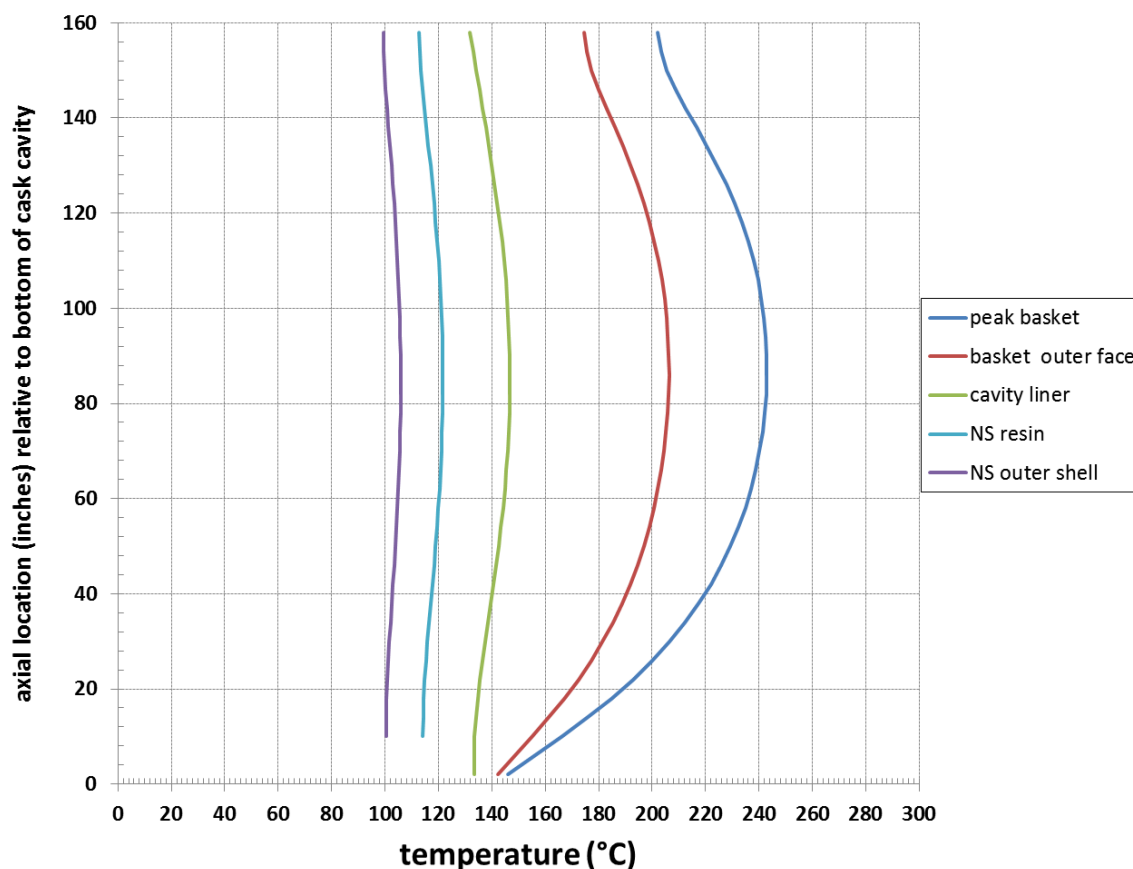


Figure 3-8. Axial temperature distributions on main components of TN-32B cask for initial storage conditions (as of 7/31/2017).

3.4.2 Axial Temperature Profiles for Option 1 Thermocouple Locations

Measured temperature data to be obtained from the fuel assemblies in the course of the 10-year Demonstration project is limited to a single radial location in each of seven assemblies, from TC lances (each containing nine thermocouples) that will be inserted into selected guide tube locations. Figure 3-9 shows the proposed Option 1 locations¹⁴ of the TC lances. The predicted axial temperature profiles from the COBRA-SFS modeling for these proposed instrumentation locations are shown in Figure 3-10. The predicted axial temperature profiles on the hottest rod in each of these instrumented assemblies are shown in Figure 3-11. Comparison of the profiles in these two Figures for a given instrumented assembly show that the measured temperatures at the TC lance location are expected to be within 5 to 10 °C of the corresponding locations on the hottest rod in an assembly. This is due in part to the relatively uniform burnup of all rods in the assembly but can also be attributed in part to the proximity of the hottest rod to the instrumented guide tube location. The hottest rod in a given instrumented assembly is generally within two to five rod rows or columns of the instrumented guide tube, for the proposed Option 1 locations, even for the peripheral assemblies, which tend to have the steepest radial temperature gradients.

¹⁴ The proposed Option 1 locations were adopted and used for actual insertion of the TC lances in the Demonstration cask.

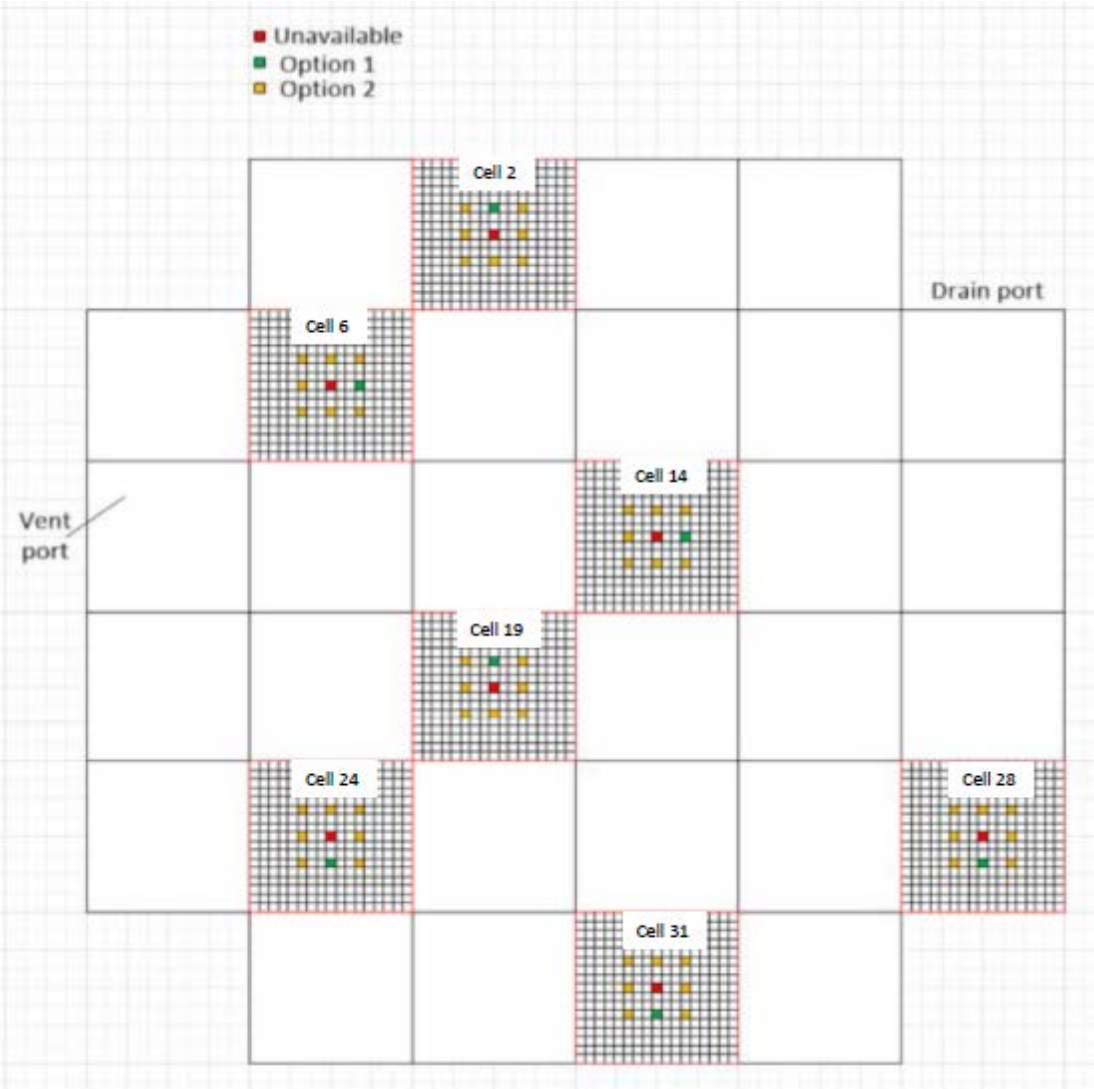


Figure 3-9. Proposed TC lance insertion locations for instrumented assemblies in the cask (Option 1 was adopted for demonstration test).

COBRA-SFS rod T predictions at Option 1 locations

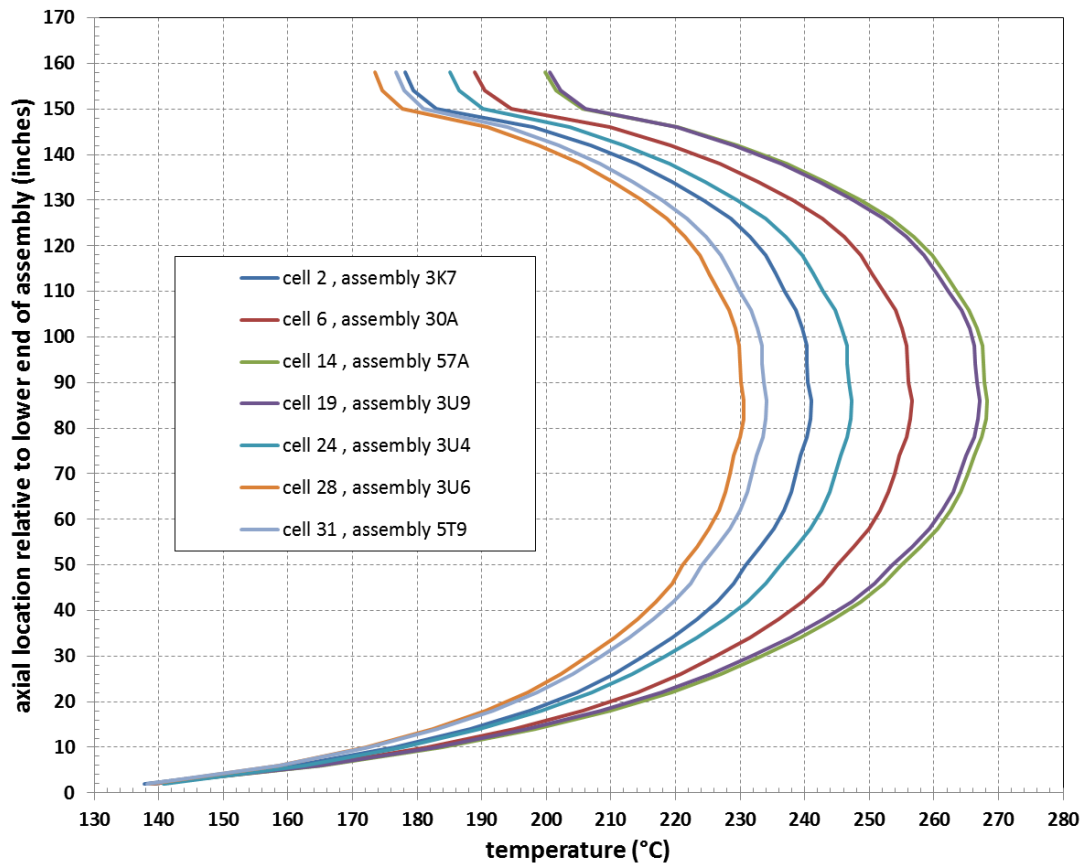


Figure 3-10. Axial temperature distribution on guide tube rod at proposed Option 1 locations for instrumented assemblies in the cask, predicted with COBRA-SFS model for initial loading conditions (decay heat as of 7/31/2017).

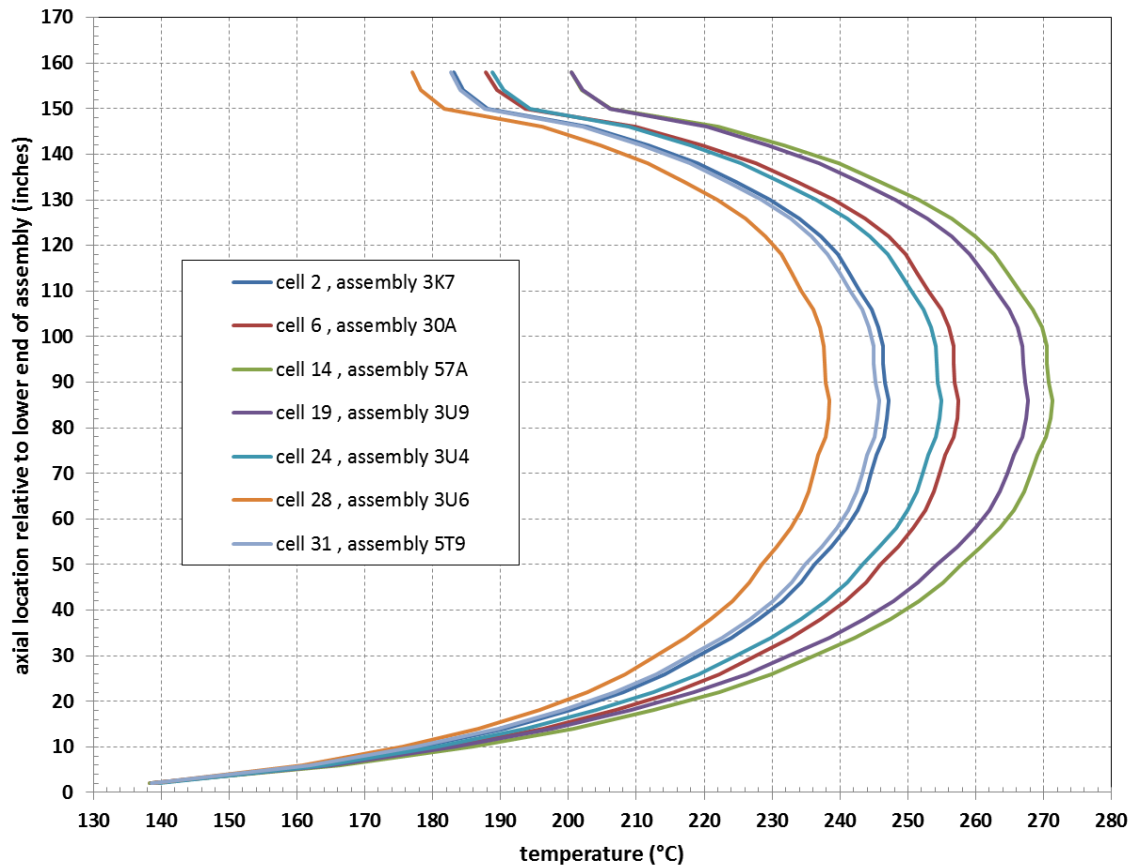


Figure 3-11. Axial temperature distribution on hottest rod in each instrumented assembly in the cask, predicted with COBRA-SFS model for initial loading conditions (decay heat as of 7/31/2017).

3.4.3 Vacuum Drying Conditions

The analysis of vacuum drying conditions was performed using the same model and inputs that were used to produce the results reported in Section 3.4.1. However, the vacuum drying analysis is a transient calculation, which in COBRA-SFS requires determining a meaningful steady-state initial condition. Since the vacuum drying conditions had not yet been defined at the time this analysis was performed, the thermal evaluations for the vacuum drying transient used the bounding assumptions typical of in licensing basis evaluations for transfer operations. Specifically,

1. The ambient conditions external to the cask within the decontamination pit are assumed to allow unconstrained free convection to air at an ambient temperature of 38°C (100°F).
2. The initial conditions for the transient assume a uniform temperature distribution of 100°C (212°F) within the fuel and basket, as a bounding temperature for the fuel rods with water in the cask cavity.
 - a. A more realistic assessment could be obtained by performing a “time to boiling” calculation for the system, based on actual conditions during loading operations. Depending on the time-frame required for operations prior to actual vacuum drying, the bounding assumption of the boiling temperature of water at 1 atm for the fuel cladding temperature may constitute a significant conservatism in the transient analysis. Actual rod temperatures within conservative time limits for transfer operations with water in the cask cavity are generally significantly below the boiling temperature for water and may be as low as 50-60°C (122-140°F).

3. The actual time required to drain the bulk of the water from the cavity and draw the cavity pressure down to the vacuum drying reference value (typically 3 torr or less), is ignored in the calculation. The system is assumed to be emptied of bulk water and reduced to the reference pressure “instantaneously” at the start of the transient.
 - a. In actual practice, the draining of the cask would be expected to take several hours, and the cavity pressure would be reduced gradually in a series of steps, with specific “hold” points at pressures much higher than 3 torr. The actual rate of temperature increase on the fuel rods during the vacuum drying transient would therefore tend to be slower than predicted in the calculation, at least for the first few hours of the transient.

With these conservative assumptions, a vacuum drying transient was performed using the COBRA-SFS model of the TN-32B, with initial loading based on the 7/31/2017 decay heat values described in Section 3.1. This calculation provides a bounding estimate of system temperatures during vacuum drying operations. Figure 3-12 shows the predicted PCT as a function of time for this bounding transient.

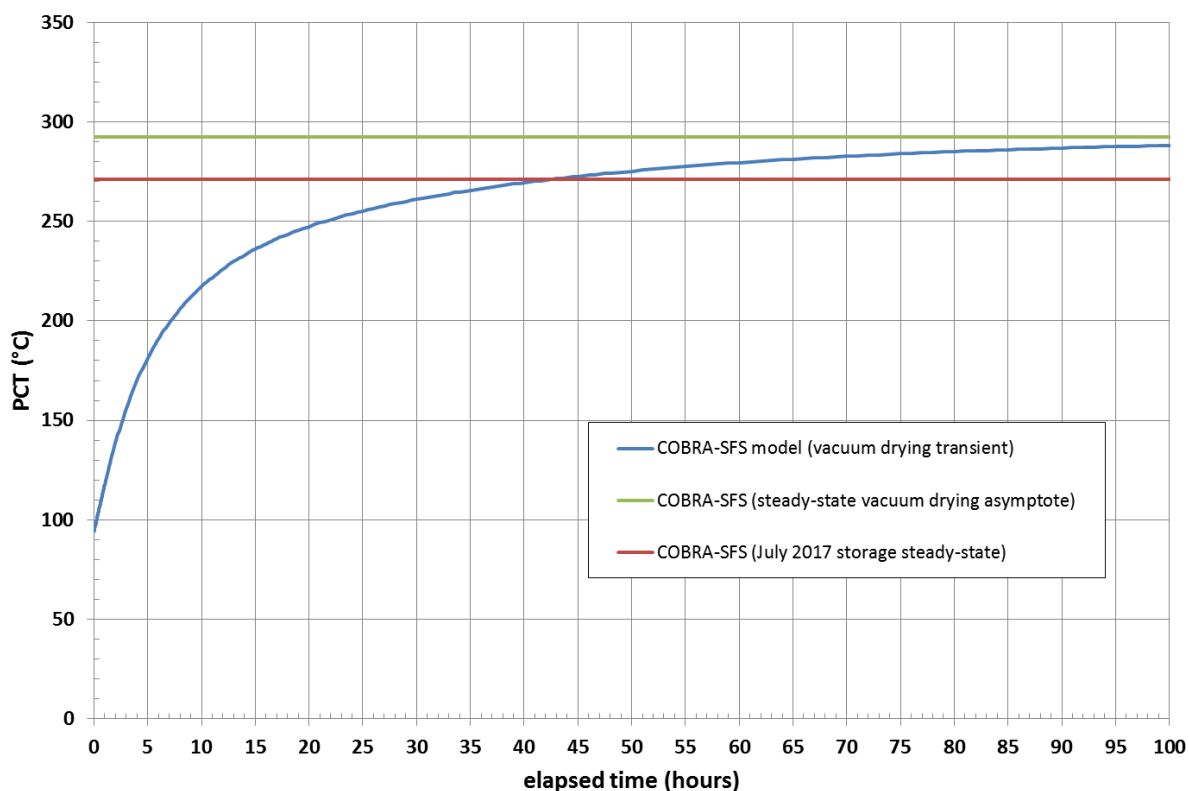


Figure 3-12. PCT as a function of time, calculated with COBRA-SFS model for bounding vacuum drying transient (30.6 kW decay heat total, as of 7/31/2017).

The transient results for this bounding evaluation of the vacuum drying operation suggest that the PCT in vacuum drying may not be significantly greater than the PCT for storage conditions, and may be constrained to a lower value, due simply to the time-frame of the operation. It has been suggested that the vacuum drying time¹⁵ for the demonstration cask could be as short as 10 hours. The plot in Figure 3-12 shows that at 10 hours, a conservative estimate of the PCT would be only about 217°C (423°F).

¹⁵ Actual vacuum drying time when the fuel assemblies were loaded into the cask, in November 2017, was less than 9 hours.

Even if the actual vacuum drying transient is not that short for the demonstration cask, the requirements defined in the TN-32B UFSAR specifically limit vacuum drying time to no more than 36 hours at design-basis heat load of 32.7 kW, primarily due to thermal limits on non-fuel components of the cask. For the estimated decay heat load of 30.6 kW, the predicted PCT for the transient evaluation shown in Figure 3-12 is 266°C (512°F) at 36 hours, which is below the maximum value of 271°C (520°F) predicted for normal storage conditions.

Program goals for the Demonstration project have led to plans for the TN-32B cask to remain in the decontamination pit for an extended period of time (2-3 weeks) after vacuum drying and helium backfill. Complete evaluation of this transient would require information on the actual transient times for specific phases of the operation, including vacuum drying and helium backfill, plus additional information on the temperature and air flow conditions in the decontamination pit, to define the boundary conditions seen by the cask for this extended transient. It would also be helpful to know how many purge cycles the cavity is subjected to in the process of backfilling with helium, as this would tend to cool down the fuel rods during the backfill process. However, an estimate of the thermal behavior of the cask during transfer operations that occur after helium backfilling can be obtained simply by extrapolating the boundary conditions assumed for the vacuum drying operation to extend to include the transient response of the system *after* backfill. Figure 3-13 shows an approximation of this transient, assuming unconstrained natural convection heat transfer from the cask outer surface to ambient air at 38°C (100°F).

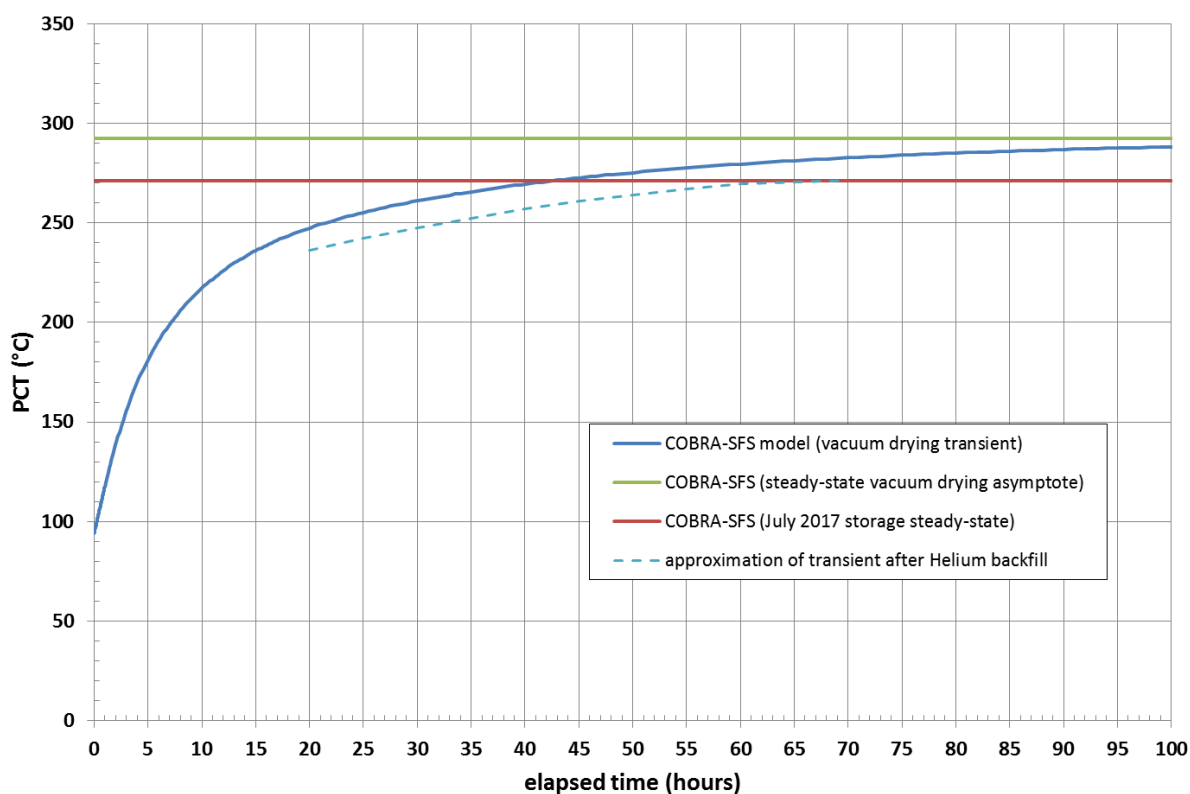


Figure 3-13. Estimated PCT as a function of time for extended transient in decontamination pit after helium backfill (30.6 kW decay heat total, as of 7/31/2017).

The results shown in Figure 3-13 suggest that the demonstration cask is very likely to reach a steady-state condition if it remains within the decontamination pit for more than 3 days after completion of vacuum drying and backfilling with helium. The actual peak temperature reached on the fuel rods would depend on the actual boundary conditions on the cask during the time in the decontamination pit, during and after the actual vacuum drying transient.

In summary, these results provide a bounding estimate of PCT during vacuum drying. A more accurate estimate of actual temperatures for the fuel during vacuum drying would require detailed information on procedures used when loading the cask, including the actual vacuum drying duration and boundary conditions during the steps prior to and during the vacuum drying process itself.

3.4.4 Storage Conditions after 10 Years

As described above, the thermal evaluations presented here are based on estimates of assembly decay heat values presented in Table 3-1. This table contains two sets of decay heat values; one set for an assumed loading date of July 2017, and one set for January 2027, at the end of the intended 10-year duration of the project. This section presents analysis results for the fuel assembly temperatures after 10 years in storage, using the decay heat estimates for 1/1/2027.

Figure 3-14 and Figure 3-15 show the predicted PCT and minimum cladding temperature, respectively, for each assembly, as of 1/1/2027.

	194	200	199	191	
191	206	212	211	206	192
197	211	204	216	212	199
200	212	215	210	212	199
195	206	213	212	207	194
	194	200	200	192	

Figure 3-14. Assembly PCTs (°C) estimated for end of 10 years in storage (as of 1/1/2027).

	115	114	114	115	
115	115	115	115	114	115
115	115	115	115	114	114
114	115	115	115	114	114
115	115	115	115	115	115
	115	115	114	115	

Figure 3-15. Assembly minimum cladding temperatures (°C) estimated for end of 10 years in storage (as of 1/1/2027).

These results show that at the end of the Demonstration project, a reasonable estimate of the maximum PCT is 216°C (421°F), on the hottest rod of fuel assembly 57A, which has a burnup of 52.2 GWd/MTU and M5[®] cladding. The minimum cladding temperature on rods in this assembly is calculated as 115°C (239°F). This is based on an assembly decay heat of 0.752 kW, calculated as of January 2027.

3.4.5 Summary of Clad Temperature Distribution

In addition to the predicted PCTs and minimum cladding temperatures reported in Section 3.4.1 for the beginning of the Demonstration project, the overall distribution of temperature on the fuel rods throughout the demonstration cask is of some interest for evaluations of material performance over time. With 32 assemblies in the cask, each containing nominally 289 fuel pin positions (and up to 264 active rods), the amount of cladding temperature data generated in a single execution of the COBRA-SFS code is on the order of 369,920 individual values (with 11,560 temperatures per assembly). Presentation of this information in a digestible form presents something of a challenge, particularly if the purpose is to convey a three-dimensional picture of the temperature distribution throughout the fuel assemblies in the basket. The predicted axial temperature profiles shown in Section 3.4.1 for the peak rod and the coolest rod of the hottest assembly illustrate the general shape of the temperature distribution throughout the basket. That is, the highest temperatures occur near the axial center of the fuel assembly, and the lowest temperatures

occur near the fuel rod ends. Minimum temperatures are near the bottom of the assemblies, and slightly higher temperatures (but still significantly lower than the peak temperatures) are seen near the upper ends of the fuel rods.

The overall distribution of temperature throughout the 32 assemblies of the basket has been captured by means of cataloging the temperatures to indicate the fraction of the cladding surface that is expected to be within a given range. Figure 3-16 shows the distribution for all assemblies (as of July 2017), cataloged in increments of 10 degrees-C, from 100°C (212°F) to 300°C (572°F). This interval results in a distribution with about 73% of the cladding surface in the range 200-250°C (392-482°F). Only about 10% of the cladding surface is predicted to be above 250°C (482°F), with less than 3% above 260°C (500°F). Approximately 17% of the cladding surface is predicted to be below 200°C (392°F) at initial loading.

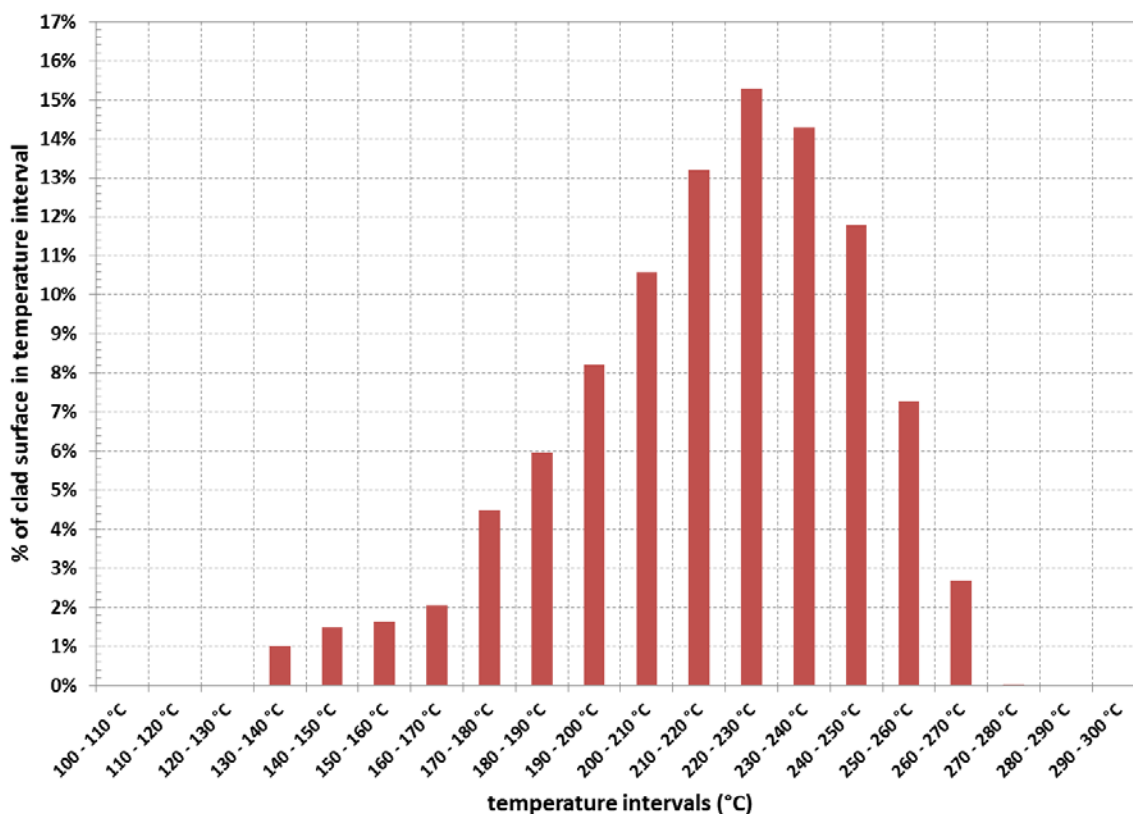


Figure 3-16. Temperature distribution ranges for all 32 assemblies in the cask, from cladding temperatures predicted with COBRA-SFS model for initial loading conditions (as of 7/31/2017).

As the fuel assemblies continue to cool during the planned 10-year duration of the Demonstration project, the temperatures on the fuel rods will decrease, and the axial profiles will tend to flatten. This is illustrated by the plot in Figure 3-17 for the hottest assembly (in cell 14), for calculated decay heat values at initial loading and projected values ten years later, for 1/1/2027. In this parsing of the cladding surface temperature predictions obtained with the COBRA-SFS model, nearly all the cladding is expected to be below 220°C (428°F) by 2027. The coolest temperatures are expected to be approaching within 50 to 60 °C of the system boundary temperature at the bottom of the cask.

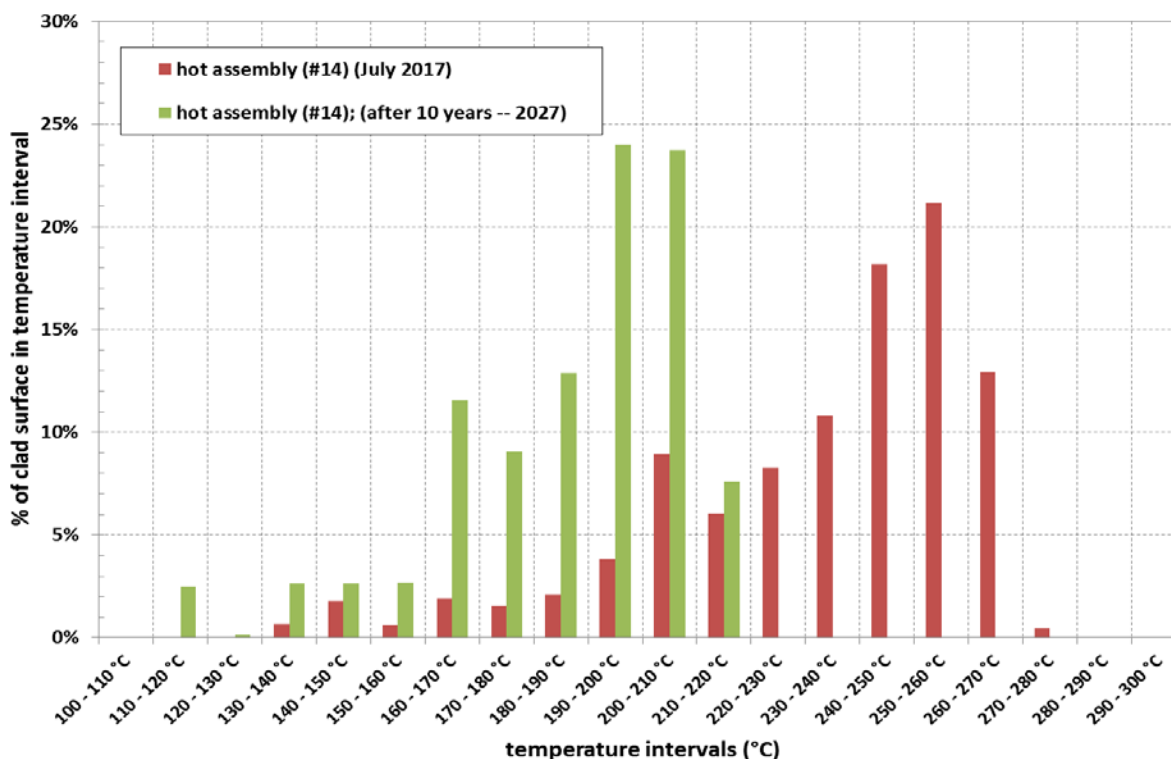


Figure 3-17. Temperature distribution ranges in the hottest assembly (#14) at initial loading (7/31/2017) and after 10 years (1/1/2027), for cladding temperatures predicted with COBRA-SFS model.

3.4.6 Effect of Changes in Input and Boundary Conditions

Development and testing of the thermal models described in this report was a lengthy process, reflecting program needs for preliminary information to guide decisions related to fuel assembly selection, materials performance concerns, and test planning, before complete information was available on the fuel to be loaded into the cask. A detailed history of this process is not described here. However, it is useful to compare results from preliminary models in Section 2.4.1 with those from the updated version in Section 3.4.1 to illustrate the impact of replacing selected inputs and assumptions with more accurate or more realistic information specific to this planned test. In general, this information was not available until final NDAs were completed with the utility, the storage cask manufacturer, and the fuel vendors.

Comparison of updated modeling results to preliminary modeling results obtained with reasonable approximations for all incompletely characterized parameters show that the single most significant input for the thermal modeling effort is the assembly decay heat values for the fuel inserted in the cask. Results presented in Section 2.4.1 of this report, based on conservative assembly decay heat values supplied by Dominion Energy (totaling 36.8 kW), yielded an overall PCT of 315°C (599°F). Results obtained *with the same model*, changing *only* the total assembly decay heat values to correspond to the values obtained in detailed calculations at ORNL (30.6 kW) in August 2015, yields a PCT of 273°C (523°F).

Additional refinement of the model to include the assembly axial decay heat profiles and pin-by-pin radial decay heat distribution from the ORNL calculations results in a further reduction of the PCT to 272°C (522°F). Including minor input adjustments to the representation of the rod-and-subchannel geometry in the final configuration of the COBRA-SFS model, using proprietary information on fuel assembly dimensions, results in a small reduction of the PCT to 271°C (520°F), as documented in Section 3.4.1.

The combined effect of these changes is a reduction in PCT of 44 °C from the preliminary model results. The magnitude of these changes in PCT in response to changes in model inputs shows that accurate results for PCT require accurate estimates of decay heats. Detailed representation of the distribution of those decay heats across an individual assembly are not essential, within the relatively narrow range of variation typical of a spent fuel assembly. Furthermore, publicly available axial power profiles and representative fuel assembly geometry data can be a sufficient basis for making accurate predictions of PCT. However, as stated in Section 3.4.1, the accuracy in cladding temperature distributions, particularly at rod ends, would benefit from an axial power profile estimated from the actual burnup history of the assembly.

The changes implemented in the final model, particularly the changes related to decay heat, yield a similar change in the steady-state asymptote predicted in the bounding calculations for vacuum drying conditions. As documented in Section 2.4.2, the steady-state PCT in vacuum drying is predicted to be 336°C (637°F) for a decay heat load of 36.8 kW, based on the conservative estimates initially supplied by Dominion. The updated model (see Section 3.4), with decay heat values from the ORNL calculations (30.6 kW) (including new axial decay heat profiles and pin-by-pin decay heat based on burnup), yields a PCT of 292°C (558°F) for the vacuum drying steady-state asymptote. This constitutes a reduction of 44 °C, which is, as expected, the same relative change seen in the calculations for storage conditions.

The transient PCT and steady-state asymptotes for these two cases are compared in Figure 3-18. The temperature transients are consistent in their approach to the asymptote and have the same time constant, as would be expected, since the thermal mass of the system is unchanged. The only significant difference is that the temperature magnitudes are shifted, in proportion to the change in total decay heat. The final result suggests that in the actual vacuum drying transient with the TN-32B cask during loading operations, the PCT is unlikely to exceed 300°C (572°F), for any reasonable boundary conditions in the fuel handling facility, or for any reasonable duration of the drying transient.

Other than the decay heat loading and distribution, the only other major boundary condition influencing PCT in the thermal modeling parameters is the assumed ambient temperature. As noted above, for simplicity and consistency, thermal evaluations for storage conditions were performed assuming still air at ambient temperature of 38°C (100°F) and neglecting the effect of insolation. For the conservative loading of 36.8 kW (as presented in Section 2.4.1), this yielded a predicted PCT of 315°C (599°F). The same model, with assumed ambient air temperature of 38°C (100°F) and insolation as specified in 10CFR71.71, yielded a PCT of 323°C (613.4°F). This suggests that adding the effect of a bounding value of solar insolation could be expected to increase the PCT by as much as 8°C. However, this same case (including insolation), with a more reasonable assumed still air temperature of 27°C (80°F), yields a PCT of 316°C (601°F). This result is essentially the same as that obtained for an assumed ambient air temperature of 38°C (100°F), without insolation.

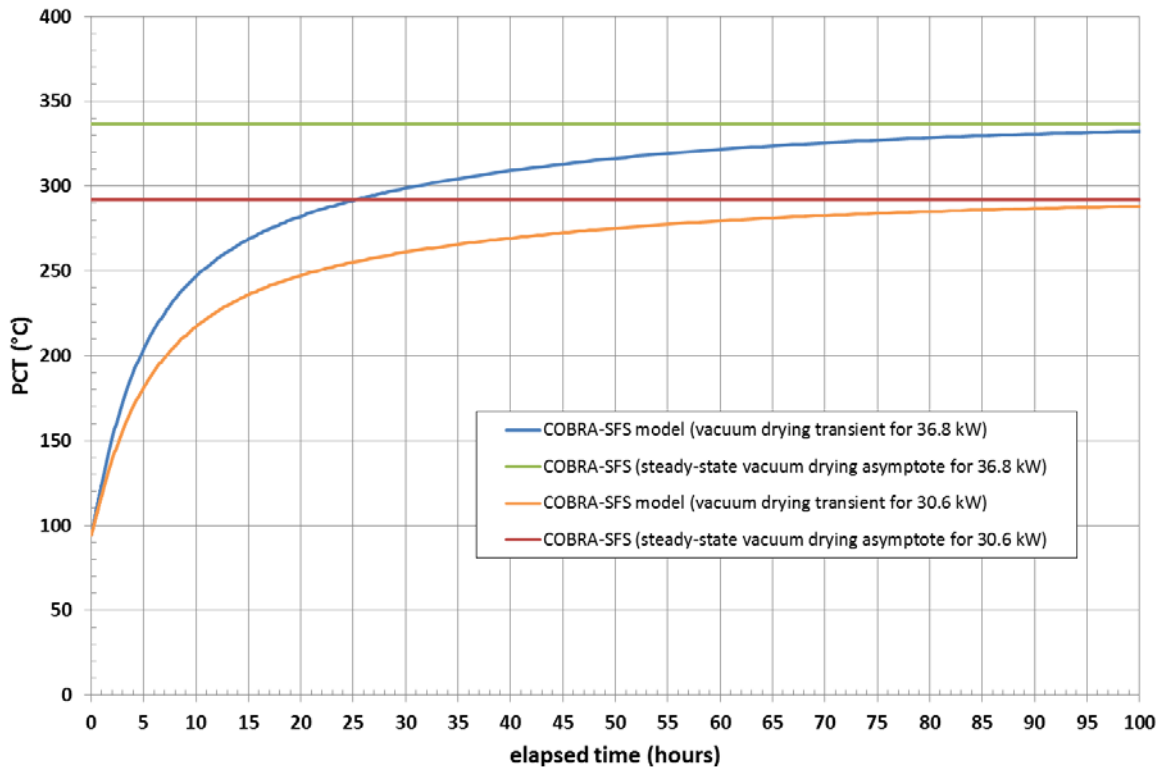


Figure 3-18. Transient PCT calculated with COBRA-SFS for 30.6 kW total decay heat compared to preliminary result with conservative (36.8 kW) total decay heat.

3.5 Model Results: STAR-CCM+

This section summarizes the results of thermal evaluations with the STAR-CCM+ model of the TN-32B cask. Section 3.5.1 presents results for assumed storage conditions at the initial planned beginning of the demonstration in July 2017. Section 3.5.2 includes a discussion of the impact of changes in input and boundary conditions on model results.

3.5.1 STAR-CCM+ Results for Initial Storage Conditions

The individual assembly total decay heats in Figure 3-1 and Table 3-1 were provided for the final proposed loading pattern with a total decay heat estimated as 30.6 kW as of 7/31/2017. Figure 3-19 shows the corresponding PCT from the STAR-CCM+ model for each assembly.

	227	250	247	222	
230	258	274	274	256	231
246	278	256	280	279	253
254	279	276	264	279	254
237	255	275	275	257	236
	254	250	248	223	

Figure 3-19. Assembly PCTs (°C) estimated with STAR-CCM+ for initial storage conditions (as of 7/31/2017).

These results show a predicted PCT of 280°C (536°F) for steady-state conditions using the same still air ambient boundary condition as in the COBRA-SFS model (see Section 3.4.1). This PCT is in basket cell 14, assembly 57A, the same as predicted with the COBRA-SFS model. Comparing the differences in peak temperatures predicted with the two models (Figure 3-20), there is agreement within 12 °C in all assemblies except for one of the outer corner assemblies.

	-11	3	3	-12	
-4	1	5	6	0	-4
5	10	1	9	10	7
7	11	8	4	10	7
-1	0	6	6	0	-2
	15	2	2	-12	

Figure 3-20. Differences (STAR-CCM+ minus COBRA-SFS) between model estimates of assembly PCTs (°C) for initial storage conditions (as of 7/31/2017).

The temperature contour plot over an axial section view of the cask in Figure 3-21 shows the full range of component temperatures, from the maximum within the heated region of the fuel to the minimum on the external surface. The section is taken through the center of the fuel compartment with the maximum cladding temperature. The elevation of the PCT is marked in Figure 3-21 and identifies the plane of the radial section view shown in Figure 3-22. The minimum surface temperature in the axial view (Figure 3-21) is 55°C (131°F), which is 17 °C above the ambient temperature of 38°C (100°F). This minimum is found at the surface of the top protective cover.

The 100°C (212°F) minimum temperature on the color scale for the contour plot of temperatures in the radial section (Figure 3-22) indicates that the outer shell temperature of the cask is considerably higher than the temperature at the top surface. The temperature contour plot in Figure 3-23 for the outer surface of the cask shows this more clearly. The highest external surface temperatures occur on the cask body, with a peak of 113°C (235°F), and the highest temperatures on the outer surface of the neutron shield are above 102°C (216°F). This is consistent with the primary direction of heat flow radially to the outer shell of the cask where it is dissipated to the environment through convection and thermal radiation. Only a small fraction of the internally generated decay heat is transferred through the ends of the storage cask.

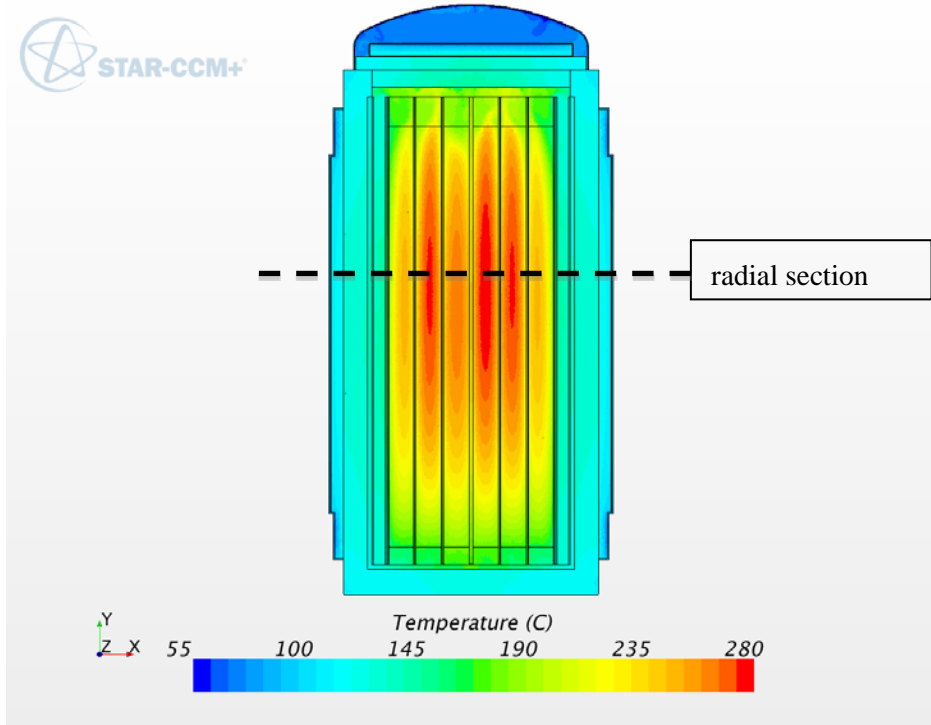


Figure 3-21. Axial section view of component temperatures.

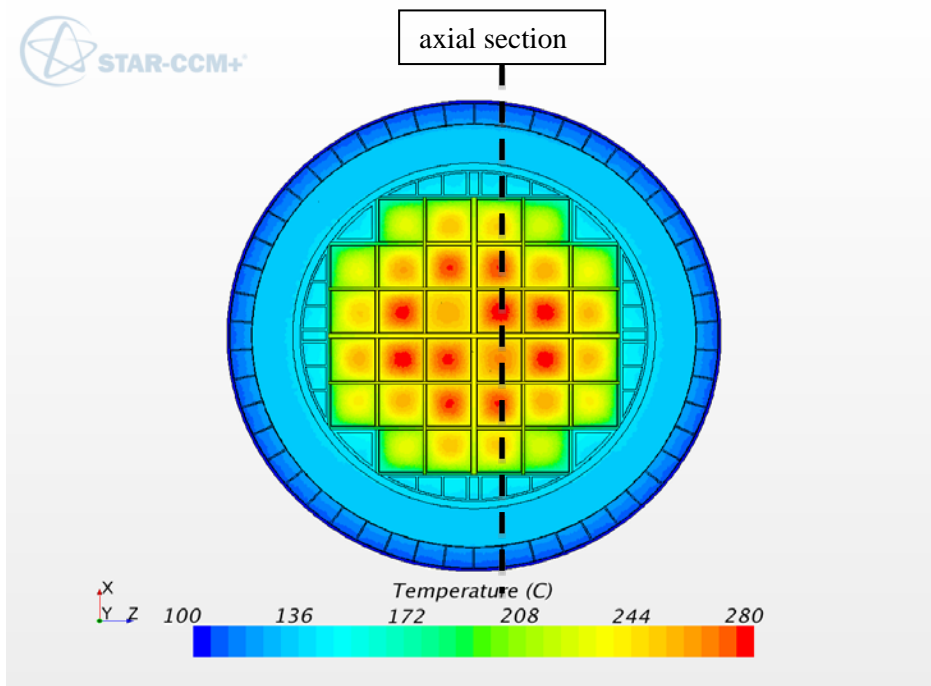


Figure 3-22. Radial section view of component temperatures at level of PCT.

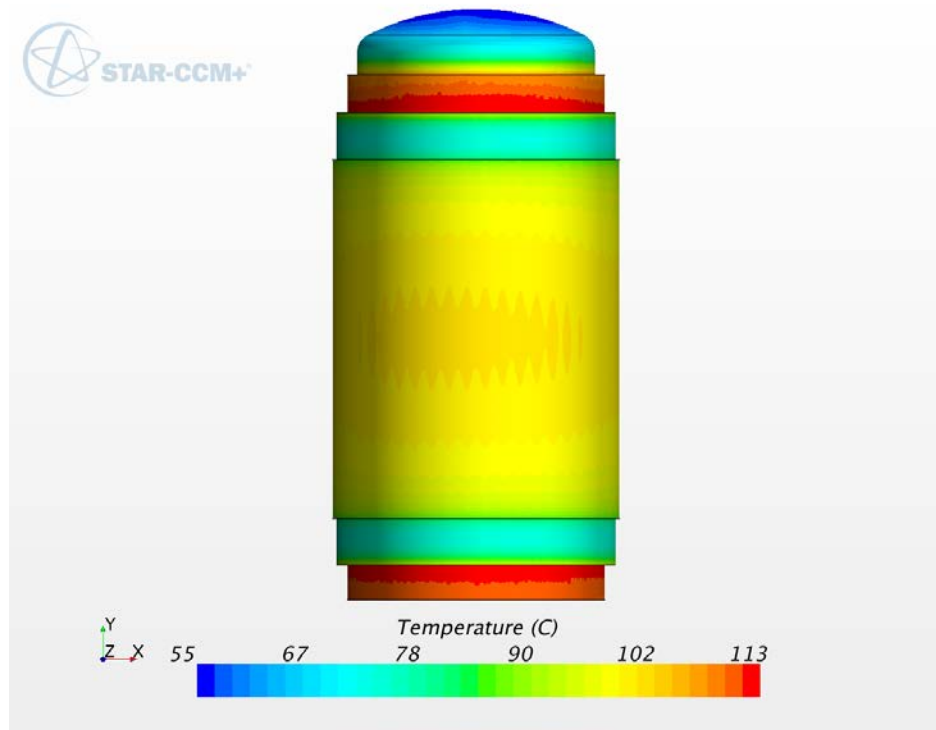


Figure 3-23. Temperature distribution on external surfaces of the cask.

The distribution of integrated heat flux through the external surfaces of the storage cask is shown in Table 3-3. There are three components of the cask with surfaces exposed directly to ambient air, consisting of the outer shell, the gamma shield, and the protective top cover (see Figure 3-23). The largest in surface area is the outer shell, which consists of the outside surfaces of the neutron shield (and appears in shades of yellow to green to aqua in Figure 3-23). The exposed surface of the carbon steel gamma shield consists of two segments, extending above and below the neutron shield structure, and is the hottest portion of the external surface (shown in shades of orange to red in Figure 3-23). The protective top cover is the coolest portion of the exposed cask surface (shown in shades of aqua to dark blue in Figure 3-23). The sum of the integrated heat flux through the outer shell and gamma shield represents the total radial heat loss from the system. This heat flux removes over 92% of the total decay heat.

Table 3-3. Split of heat loss through external boundaries.

Boundary	Integrated Heat Flux, kW
gamma shield	4.9
ground	0.7
outer shell	23.3
protective cover	1.7

The vertical component of gas velocities are shown in the axial and radial section contour plots in Figure 3-24 and Figure 3-25, respectively. The radial section is at the mid-height of the cask and the

velocity plot in Figure 3-25 clearly shows upflow in the center of the fuel region, balanced by downflow near the outside of the basket. However, the velocity magnitudes estimated with STAR-CCM+ are small and would not be expected to have a large effect on heat distribution in the cask. This result supports the reasonableness of the decision not to develop porous loss coefficients for this model.

Figure 3-26 shows the backfill gas velocity magnitude at the elevation of the drain holes in the bottom of the basket. This illustrates the flow between locations in the fuel basket due to varying decay heat load and transverse temperature gradient. There is no exchange with gas in the rail cavities due to the lack of rail cutouts that would allow this communication. The rails are open at the bottom, but they sit flat on the bottom of the containment. No allowance for leakage at this interface was assumed in the present model.

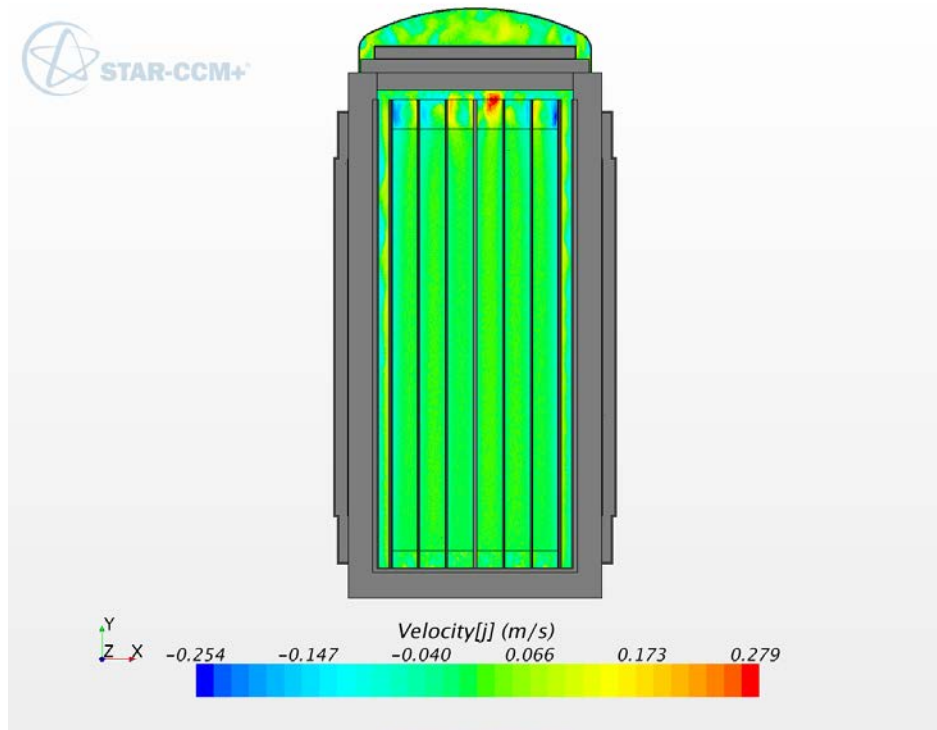


Figure 3-24. Axial section view showing vertical component of gas velocities.

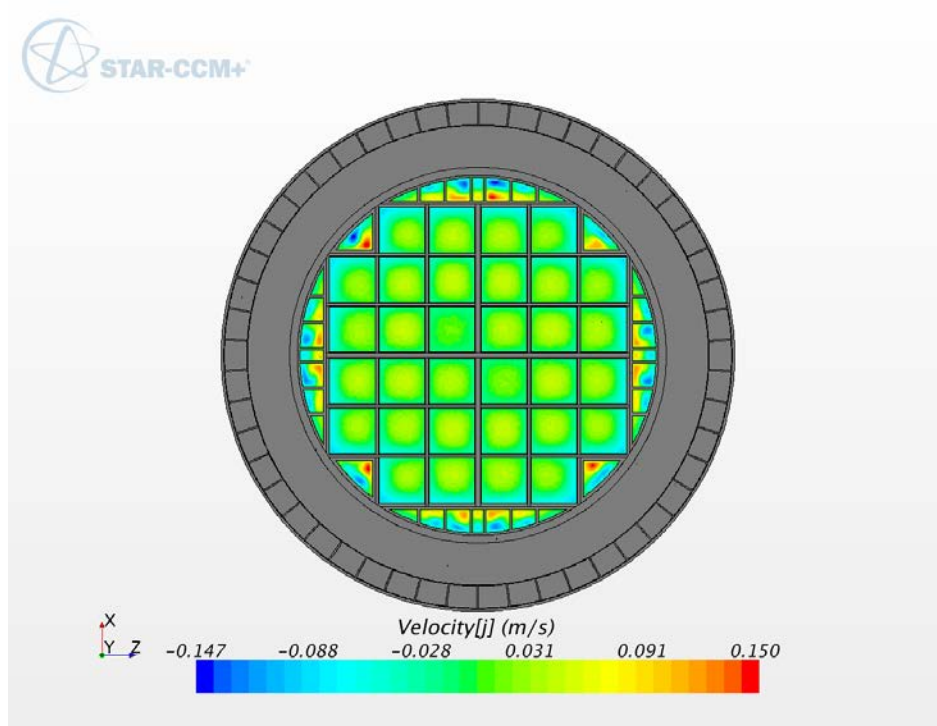


Figure 3-25. Radial section view showing vertical component of backfill gas velocity.

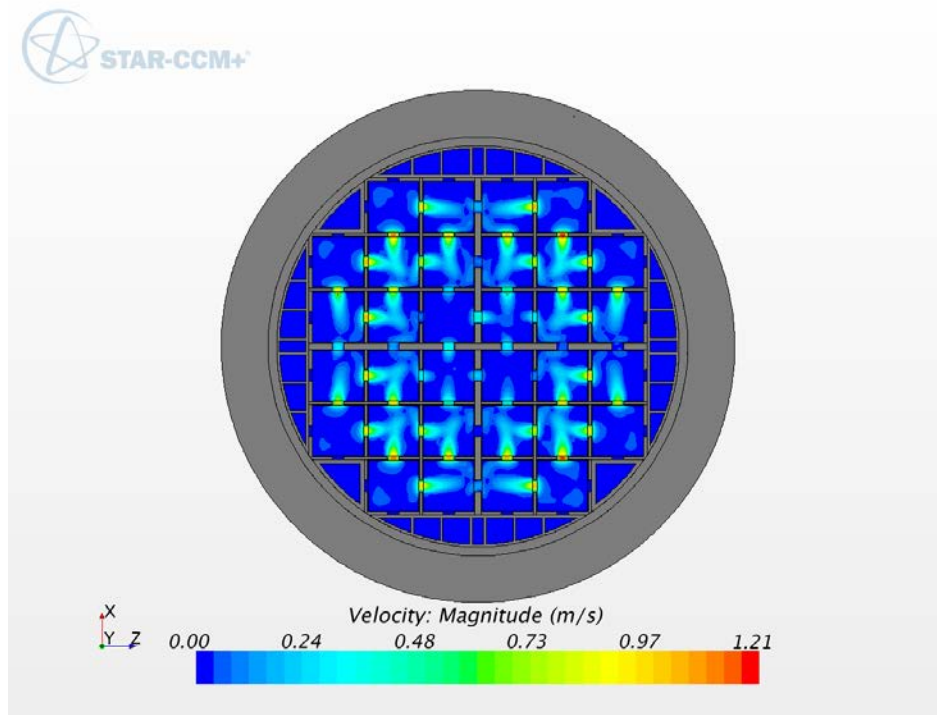


Figure 3-26. Velocity magnitude of fill gas at level of drain holes at bottom of basket.

3.5.2 Effect of Changes in Input and Boundary Conditions

This section compares results from the updated model to show the impact of input and boundary condition changes on cladding and cask component temperatures. This parallels the discussion for the COBRA-SFS model in Section 3.4.6, but here the comparison is limited to the effect of decay heat and solar insolation.

As observed for the COBRA-SFS model, changes made in decay heat had the most significant effect on PCTs. This is due to the magnitude of the change in this input variable. Conservative estimates of assembly decay heats from Dominion yielded a total decay heat load of 36.8 kW. In comparison, calculated values from burnup data, which were used in the final model runs, totaled only 30.6 kW, a reduction of 17%. PCT estimated with the STAR-CCM+ model for the final model was 280°C (536°F), as was shown in Figure 3-19. PCT estimated with the STAR-CCM+ model with the conservative estimate of decay heat, with all other model inputs and boundary conditions the same, is 325°C (617°F). The net decrease in PCT is 45°C, which is consistent with the change calculated with the COBRA-SFS model.

As stated in Section 3.5.1, the assumption in models with both codes is to neglect the influence of solar insolation. Experience has shown this to have a small effect on PCT, and the conservative use of the hot ambient temperature in the external surface boundary condition is expected to be essentially equivalent to more typical ambient temperatures with solar insolation (see discussion for COBRA-SFS in Section 3.4.6). This is a reasonable approach when the primary interest is in cladding temperature. However, it is useful to check the impact of solar insolation on the temperature of components external to the cask, in particular the neutron shield material.

The UFSAR (2012) states that the temperature limit for the neutron shield resin is 149°C (300°F). Table 3-4 shows a comparison of peak temperature in the lid and radial neutron shield material with and without regulatory¹⁶ solar insolation. Both cases use the same 38°C (100°F) ambient. Credit is not taken for the absorptivity of the cask surface, which would lessen this difference, and therefore this value with solar insolation should be viewed as a conservative maximum estimate. These results indicate that the material limit would not be exceeded in either neutron shield location.

Table 3-4. Peak neutron shield temperature with and without regulatory solar insolation.

Neutron Shield	T _{max} w/o solar °C	T _{max} w/ solar °C
circumferential	123	133
upper lid	132	143

The corresponding increase in peak fuel cladding temperature is 9 °C, from 280°C (536°F) without solar insolation to 289°C (552°F) with solar insolation, with no other changes. This increase is consistent with the increase calculated with the COBRA-SFS model.

¹⁶ As specified for normal conditions under 10CFR71.71 (10CFR71 2003).

This page is intentionally left blank

4. PRE-LOADING TEMPERATURE ESTIMATES

When the November 2017 loading date was set for the TN-32B cask at North Anna, one of the items on the list of preparations was estimates of fuel temperature after the cask is moved to the decontamination pit. These estimates would be compared with measured temperatures during the loading and post-drying thermal soak to gauge if fuel temperatures were behaving as expected.

The November loading date was shifted by a few months from the initial planning date of July 2017 used in the earlier modeling exercises (Sections 2 and 3). Therefore, a new set of decay heat estimates were required. ORNL produced these updated estimates and the total loading decay heat was 30.4 kW, or about 200 W lower than the July total. This estimate was refined further for the round robin modeling exercise described in the next section, but it was sufficiently close for the purpose of the pre-loading fuel temperature estimates.

Another significant input parameter to the models is the ambient conditions inside the fuels handling building. The building is unheated, so in November it would be less than the 100 °F, hot ambient that was assumed in the earlier storage condition estimates. Because of the potential variability in this input parameter, a range of cases were considered.

Although additional model updates would be required for more accurate representation of the geometry of the loaded cask and conditions in the decontamination pit, these pre-loading fuel temperature estimates were produced using the best estimate models described in Section 3 with updates only to the assembly decay heats and the ambient temperature.

Pre-loading peak fuel cladding temperature estimates are provided in Table 4.1 for ambient temperatures of 50, 70, and 90 °F. The comparison between the two models show a consistent difference of approximately 8 °C. This is consistent with the difference shown in the storage estimates for these two models in Section 3.4.1 and 3.5.1 and reflects the conservatism in the effective thermal conductivity representation of the fuel in the STAR-CCM+ model.

Table 4-1. Pre-loading estimates of peak fuel cladding temperature.

Ambient Temperature, °F	Peak Fuel Cladding Temperature, °C		
	COBRA-SFS	STAR-CCM+	Difference
50	252.3	260.6	8.3
70	259.4	267.8	8.4
90	266.3	274.5	8.2

The estimates shown in Table 4.1 for a 70 °F ambient are roughly 10 °C above those that were submitted later as blind predictions in the round robin modeling exercise. Although the magnitude of the peak cladding temperature decreased with further model refinement and more accurate model inputs, the trend in peak fuel temperature with ambient temperature should be unchanged. The results in Table 4.1 indicate that the slope over this range is 0.65 degrees increase in peak cladding temperature per degree increase in the thermal ambient.

The pre-loading temperature estimates included axial variation for comparison to the thermocouple lance, but these are omitted in this report since more accurate predictions are presented in Section 5.

This page is intentionally left blank

5. ROUND ROBIN MODELING OF THE CASK LOADING

Thermal modeling of the newly loaded TN-32B cask at North Anna was undertaken by several modeling teams, including ORANO TN, NRC, and PNNL. In planning this “round robin” modeling exercise, it was decided to model the cask conditions at the end of the two-week thermal soak, during which the cask was sitting in the decontamination pit in the fuels handling building. Earlier modeling work suggested that this time period would be more than sufficient for the cask to reach thermal equilibrium, which would thus allow steady state modeling, rather than requiring transient evaluations.

Each team was given the same description of the cask configuration in the decontamination pit, the assembly loading map, and measured temperatures of the ambient air adjacent to the cask. This description was compiled following the actual loading and included photographs and dimensional details. A copy of that document is included in Appendix A of this report. Additionally, each team had access to proprietary details involving the fuel geometry and all were directed to the proprietary TN-32B UFSAR (2012) for details regarding the cask.

Using this common information, the intention of the round robin was to find out what differences might be observed in predicted temperatures due to differing models and assumptions used by the individual teams and how far these predictions might differ from the measured temperatures in the cask fuel assemblies. The PNNL contributions to this exercise are described in more detail in this report. A separate report is being prepared by the Electric Power Research Institute (EPRI) that will present results from all of the modeling participants.

Differences from previous PNNL models of the TN-32B are described in Section 5.1. Blind prediction results are compared with measurements in Section 5.2. Section 5.3 presents results of sensitivity runs to determine the most likely cause of differences between blind predictions and measurements. Adjusted best estimate model results are provided in Section 5.4.

5.1 Model Descriptions

In general, both the COBRA-SFS and STAR-CCM+ models used in this exercise were based on the best estimate load planning models described in Section 3. This section describes specific changes to those models to estimate steady-state temperatures in the loaded cask following the two-week thermal soak in the fuels handling building.

5.1.1 COBRA-SFS Model

The cask loading used the updated decay heat estimates for November of 2017. The decay heat for one assembly was corrected upward from the values used in the pre-loading estimates (Section 4). The decay heats for several assemblies were decreased to account for the removal of sister rods. These decay heats are shown in the updated loading map in Figure 5-1. The total decay heat estimate for the November 2017 loading was 30.4 kW.

Since COBRA-SFS uses a rod-by-rod representation of the fuel assembly, the removal of the sister rods was represented by replacing those rods in the model by an identically dimensioned rod with no decay heat. Thermal properties of these dummy rods were the same as for the fuel.

	1 6T0 NAIF/P+Z Zirlo, 54.2 GWd 4.25%/3 cy/12.1 yr 912.2 W	2 (TC Lance) 3K7 AMBW M5, 53.4 GWd 4.55%/3 cy/8.7 yr 978.2 W	3 3T6 NAIF/P+Z Zirlo, 54.3 GWd 4.25%/3 cy/12.1 yr 914.4 W	4 6F2 NAIF/P+Z Zirlo, 51.9 GWd 4.25%/3 cy/13.5 yr 799.5 W	Drain Port
5 3F6 NAIF/P+Z Zirlo, 52.1 GWd 4.25%/3 cy/13.5 yr 800.9 W	6 (TC Lance) 30A AMBW M5, 52.0 GWd 4.55%/3 cy/7.2 yr 1008.6 W	7 22B AMBW M5, 51.2 GWd 4.55%/3 cy/5.7 yr 1142.4 W	8 (PRA) 20B AMBW M5, 50.5 GWd 4.55%/3 cy/5.7 yr 1121.2 W	9 5K6 AMBW M5, 53.3 GWd 4.55%/3 cy/8.7 yr 975.1 W	10 5D5 NAIF/P+Z Zirlo, 55.5 GWd 4.20%/3 cy/17.7 yr 814.5 W
11 (Vent Port) 5D9 NAIF/P+Z Zirlo, 54.6 GWd 4.20%/3 cy/17.7 yr 802.6 W	12 28B AMBW M5, 51.0 GWd 4.55%/3 cy/5.7 yr 1135.0 W	13 (PRA) F40 LOPAR Zry-4, 50.6 GWd 3.59%/3 cy/30.6 yr 573.8 W	14 (TC Lance) 57A AMBW M5, 52.2GWd 4.55%/3 cy/7.2 yr 1037.0 W	15 (PRA) 30B AMBW M5, 50.6 GWd 4.55%/3 cy/5.7 yr 1124.8 W	16 3K4 AMBW M5, 51.8 GWd 4.55%/3 cy/8.7 yr 941.3 W
17 5K7 AMBW M5, 53.3 GWd 4.55%/3 cy/8.7 yr 961.7 W	18 (PRA) 50B AMBW M5, 50.9 GWd 4.55%/3 cy/5.7 yr 1131.1 W	19 (TC Lance) 3U9 NAIF/P+Z Zirlo, 53.1 GWd 4.45%/3 cy/10.6 yr 920.2 W	20 (PRA) 0A4 NAIF Low-Sn Zry-4, 50.0 GWd 4.00%/2 cy/23.2 yr 646.2 W	21 15B AMBW M5, 51.0 GWd 4.55%/3 cy/5.7 yr 1135.8 W	22 6K4 AMBW M5, 51.9 GWd 4.55%/3 cy/8.7 yr 941.2 W
23 3T2 NAIF/P+Z Zirlo, 55.1 GWd 4.25%/3 cy/12.1 yr 934.7 W	24 (TC Lance) 3U4 NAIF/P+Z Zirlo, 52.9 GWd 4.45%/3 cy/10.6 yr 914.2 W	25 (PRA) 56B AMBW M5, 51.0 GWd 4.55%/3 cy/5.7 yr 1133.7 W	26 54B AMBW M5, 51.3 GWd 4.55%/3 cy/5.7 yr 1136.3 W	27 6V0 AMBW M5, 53.5 GWd 4.40%/3 cy/8.7 yr 988.2 W	28 (TC Lance) 3U6 NAIF/P+Z Zirlo, 53.0 GWd 4.45%/3 cy/10.6 yr 916.9 W
	29 4V4 AMBW M5, 51.2 GWd 4.40%/3 cy/9.1 yr 914.2 W	30 5K1 AMBW M5, 53.0 GWd 4.55%/3 cy/8.7 yr 968.0 W	31 (TC Lance) 5T9 NAIF/P+Z Zirlo, 54.9 GWd 4.25%/3 cy/12.1 yr 927.7 W	32 4F1 NAIF/P+Z Zirlo, 52.3 GWd 4.25%/3 cy/13.5 yr 804.3 W	

Figure 5-1. Updated loading map for November 2017 loading.

5.1.1.1 Geometry

There were several changes to the top and bottom of the model geometry. On the top, the protective cover, overpressure vessel assembly, and neutron absorber were removed from the model, leaving only the cask inner and outer lid represented, to conform to the cask configuration while in the decontamination pit. On the bottom, the leveling pad was included and represented as a conduction path only. Convection and radiation between the bottom of the leveling pad and the ground is neglected in the model. This simplification was made because it was determined that including these two modes of heat transfer would not significantly affect results. No change was made to the model geometry to account for the thermocouple penetrations in the lid or for the lead blankets placed on top of the lid for shielding.

5.1.1.2 Boundary Conditions

The description of the TN-32B in the decontamination pit in Appendix A reports a significant difference in ambient temperature between that measured in the air space surrounding the cask below the inspection platform and that measured in the much larger space above the working platform. A duplicate of that temperature plot (Appendix A, Figure A-19) is shown in Figure 5-2. As shown in this figure, the measured ambient temperatures all have a diurnal variation due to warmup and cooldown of the unconditioned airspace in response to changing outdoor temperatures. The temperature traces have a consistent average temperature over the ten-day period from 11/19 to 11/29. For the thermocouple measurement in the airspace below the working platform, this average was approximately 24°C (75°F). The two thermocouple measurements above the working platform, at the data logger, track together and have a nominal average of 15.6°C (60°F) over that same time period. Figure 5-2 shows that the daily minimum to maximum temperature difference ranged from -9.4°C to -3.9°C (15 to 25°F). However, the cask has a large thermal inertia and therefore a large time constant, allowing for an approximation using a steady-state solution and fixed ambient temperature. In the COBRA-SFS model, a 24°C (75°F) ambient temperature was applied to the side boundary with a natural convection correlation for a vertical cylinder. The top boundary used a 16°C (60°F) temperature with a natural convection correlation for an upward facing plate heated from below.

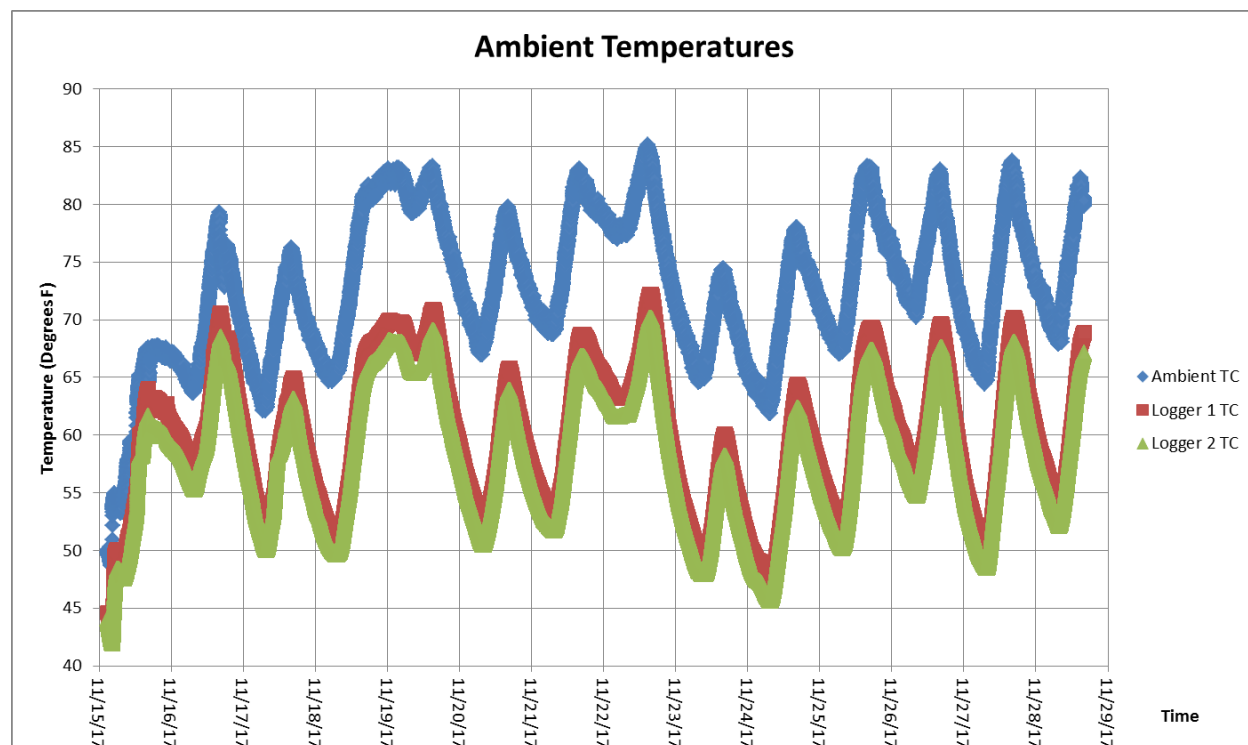


Figure 5-2. Air temperature in the decontamination pit (ambient TC) and above the work platform (logger 1 & 2 TC).

5.1.2 STAR-CCM+ Model

Assembly decay heats in the STAR-CCM+ model were updated to be consistent with Figure 5-1. As in previous models, these were applied as assembly average decay heats, as opposed to the COBRA-SFS model, which uses pin-by-pin data.

Model updates and runs for this part of the project were performed using STAR-CCM+ Version 11.06 (2016).

5.1.2.1 Geometry

By comparing the previous model geometry (Section 2.2.1) with photographs of the cask in the decontamination pit, it was obvious that the neutron shield as represented in the existing model was shorter than it should be. The model geometry was based on a section view of the cask through the trunnions, where the neutron absorber has a shorter length. This shortened length had been used for the full circumference of the cask. The neutron shield length was corrected for the model of the cask in the decontamination pit. Since the trunnions are not included in the model, this was accomplished by lengthening just the neutron shield toward the top and bottom of the cask.

The only other change in the model geometry was to remove the protective cover, overpressure vessel assembly, and neutron absorber from the top of the bolted cask lid to match to the conditions during the thermal soak. No change was made to the model geometry to account for the thermocouple penetrations in the lid or for the lead blankets placed on top of the lid for shielding.

5.1.2.2 Boundary Conditions

Two different sets of boundary conditions were used. One set used natural convection boundary conditions with measured air temperatures in the loading pit and in the space above the cask. The second set used the same convection boundary conditions for the top and bottom of the cask but imposed measured cask surface temperatures on its vertical surface. Details for the natural convection boundary conditions are provided below. The measurement locations and measured values for the imposed surface temperature boundary conditions are described along with model results for that case in Section 5.2.2.

The difference between ambient temperatures above and below the work platform in the decontamination pit were described above in Section 5.1.1.2. Unfortunately, in STAR-CCM+ there is no obvious way to treat differing ambient temperatures for different parts of the cask exterior. In addition to the differing ambient temperatures above and below the work platform, treatment of radiation from the base of the cask and leveling pad are complicated by this limitation. In the end, the decision was made to use a single 24°C (75°F) ambient for all surfaces of the cask. This best represents the vertical surface of the cask, through which most of the heat is dissipated. It is higher than the nominal value of 16°C (60°F) for the top of the cask, but this is at least partially compensated for by neglecting resistance for heat transfer through the lead blankets. The relative magnitude of these two compensating modeling simplifications was not estimated. Surface properties for these painted steel surfaces were the same as those used in the prior models.

For the boundary condition at the bottom of the cask, radiation to the floor would not be satisfactorily represented by a 24°C (75°F) ambient, since the floor surface is close to the base and would have a higher temperature locally. Because of this limitation, it was decided to ignore thermal radiation from the base and instead just treat it exclusively as a natural convection boundary. This also is an approximation since the air beneath the cask is confined and its temperature is no doubt higher than 24°C (75°F). But as with the treatment on top of the cask, there is some compensation from other simplifying assumptions; in this case neglecting the contribution of heat transfer due to thermal radiation.

Natural convection correlations are the same used in previous models (see Section 2.2.5.2). The full axial length of the radial neutron shield was used as the representative length scale in the correlation for that surface, ignoring the interference of the work platform, because the work platform was very nearly at the top of the neutron shield.

5.1.2.3 Gap Resistances

The thermal resistances used for helium and air gaps in the model were the same as those used in the previous models (Section 2.2.6). Sensitivity studies that looked at variations in some of these gap

resistances were completed following submission of the blind test results. These are described in Section 5.3.

5.1.2.4 Fuel Region

The same effective radial thermal conductivity model was used in the preliminary and best estimate analyses with STAR-CCM+. As described in Section 2.2.4, it was developed using COBRA-SFS models of a 17×17 OFA assembly with a 0.6 kW assembly decay heat.

The axial effective conductivity model was also retained from the earlier studies. As described in Section 2.2.4, it is taken directly from the UFSAR (2012). The impact of the poison rod assemblies (PRAs) inserted into the guide tubes of selected assemblies was considered (see Appendix A, Figure A-7), but their contribution to axial conduction was judged to be insignificant for this analysis. The neutron absorber material within the PRA inserts is in the form of pellets, so that the effective axial conductivity would be significantly reduced by the inter-pellet gap resistances.

5.1.2.5 Mesh

The geometry changes in the model necessitated a remesh. The preliminary and best estimate modeling had been done with the same computational mesh and it has been viewed as excessively refined. The remesh for the updated geometry provided an opportunity to compare results for a variety of mesh settings, one using the same settings as in the original mesh, and two with more-coarse meshes.

Results were compared for an intermediate model version, which is not quite what was submitted for the blind prediction, but close enough to be representative. Cell count for the three mesh cases are shown in Table 5-1 along with peak cladding temperature for the test case.

Table 5-1. Grid convergence test data.

Mesh	Cell count	PCT, C
fine	25M	267.600
medium	6.8M	267.587
coarse	4.1M	267.338

Using these results, an estimate of discretization error can be obtained by determining the Grid Convergence Index (GCI). This parameter is calculated following the approach outlined in Roach (2009).

The estimated fractional error, E_1 , for the fine grid solution f_1 , is calculated as

$$E_1[\text{fine grid}] = \frac{\varepsilon}{r^p - 1}$$
$$\varepsilon = \frac{f_2 - f_1}{f_1}$$

In this approach, ε is the relative change in the solution for two meshes, with f_1 designating the fine mesh solution and f_2 the solution for the coarse mesh. The r term is the refinement ratio of the two meshes f_1 and f_2 . The exponent p on the refinement ratio is the order of the solution method, which in this case is second order, so $p = 2$. Ideally, the mesh is refined by a ratio of two in each dimension, so $r^p = 2^2 = 4$. In practice, this is often impractical, and the refinement ratio need not be identically two.

For an unstructured mesh, an effective refinement ratio is

$$\text{effective } r = \left(\frac{N_1}{N_2} \right)^{1/D}$$

where N_1 and N_2 are the total cell count for the two meshes and D is the dimensionality of the system. The GCI is obtained by multiplying the absolute value of the estimated fractional error, E_1 , by a scale factor. The calculation here uses the recommended value of 3.

$$GCI [\text{fine grid}] = 3 \frac{|\varepsilon|}{r^p - 1}$$

Applying this to the results for the cell counts of the different mesh resolutions shown in Table 5-1 yields the estimates of GCI shown in Table 5-2. Note that the GCI is not a bounding error estimate, rather an indication of the relative error. For these two cases, it is prudent to use the larger of the two estimates. So, for a PCT on the order of 260°C, an estimate of the relative numerical error for the fine grid solution is 0.00125 x 260, which is 0.3°C.

Table 5-2. Grid convergence index.

f_2	r	ε	E_1	GCI [fine grid]
Coarse mesh	1.83	0.000979	0.000417	0.00125
Medium mesh	1.55	4.78E-05	3.45E-05	0.000103

5.2 Blind Predictions of Temperature at End of Two-Week Thermal Soak

This section describes the results of blind model predictions using convective correlations and measured surface temperature as boundary conditions. Results are presented for blind predictions with both the STAR-CCM+ model and the COBRA-SFS model, comparing these predicted temperatures to each other and to the measured data. Comparisons with results obtained with different modeling assumptions are also discussed. Section 5.2.1 discusses results obtained with both models using natural convection correlations to ambient as boundary conditions. Section 5.2.2 discusses results obtained in blind calculations with STAR-CCM+ only using measured cask surface temperatures as boundary conditions.

5.2.1 Blind Modeling Results Using Convective Correlations as Boundary Conditions

The first blind modeling results were obtained using a convective boundary condition on the side of the cask, for both STAR-CCM+ and COBRA-SFS. This section presents comparisons of predicted temperatures to measured surface temperatures for this modeling configuration. The peak cladding temperatures estimated by each model are shown first, in Figure 5-3. Note that these peak temperatures will be slightly above the temperatures in the guide tubes where the thermocouples lances are located.

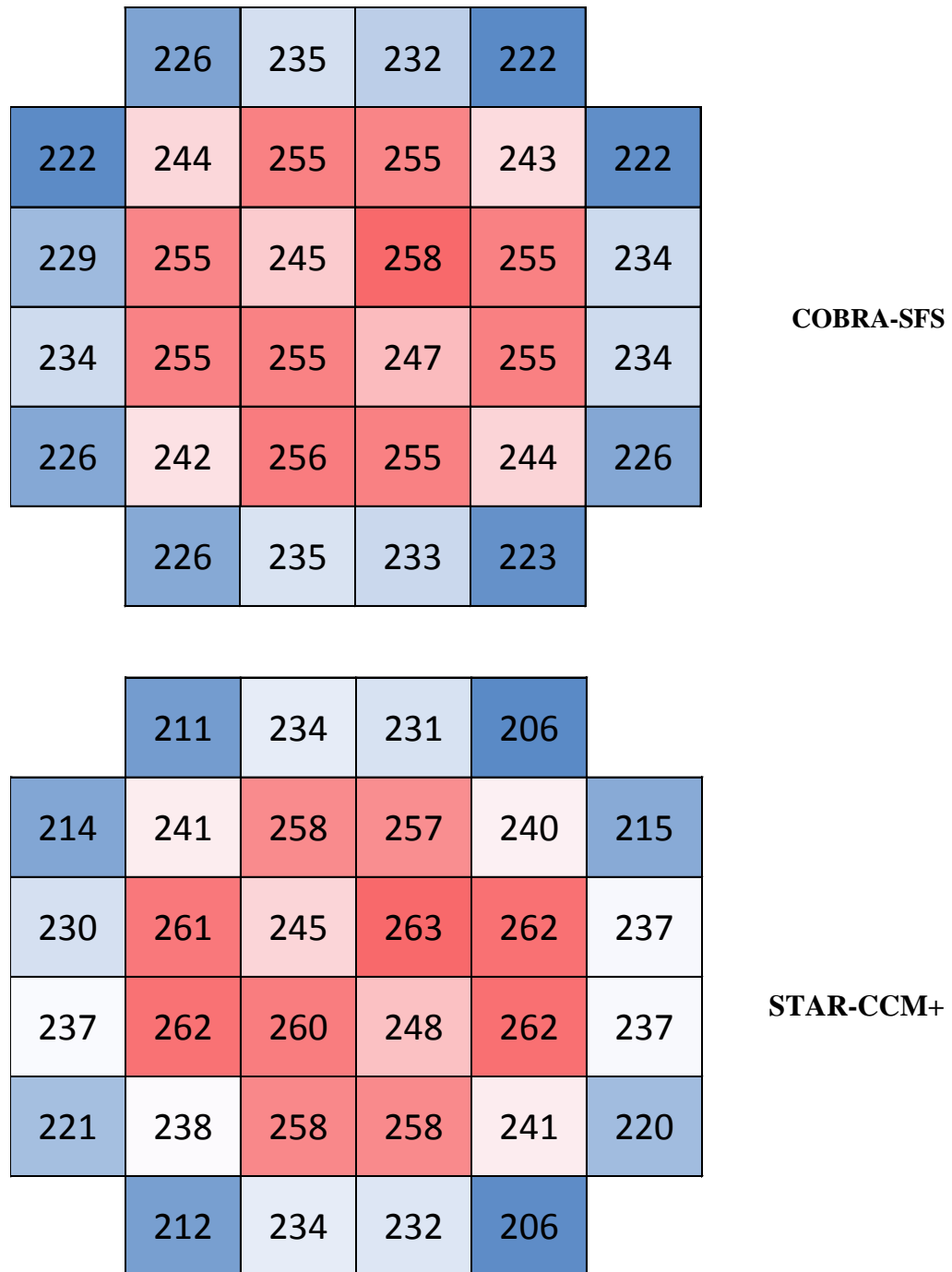


Figure 5-3. Estimated peak fuel cladding estimates – Convective Boundary Condition.

Temperatures at the thermocouple locations are presented next. The measured temperatures at the end of the five-day thermal soak are shown in Table 5-3. The predicted temperatures at the thermocouple locations obtained with convection boundary conditions are shown in Table 5-4. The difference between the measured and predicted temperatures are shown in Table 5-5.

The comparison shown in Table 5-5 was rather surprising when first observed. The code predictions range from 20 to 40 °C high. These differences are far too large for a “best estimate” and suggest problems with the models or model inputs. Reasons for these differences are provided in sections that follow.

Note that there is good agreement for the location of the peak fuel temperature. A comparison between model predictions and measurements show the peak temperature in Cell 14 (Assembly 57A) at an axial level of 94 inches.

Table 5-3. Measured temperatures at thermocouple lance positions at end of thermal soak.

Thermocouple Lance Data (°C)							
Axial Level (in.)	2 (3K7)	6 (30A)	14 (57A)	19 (3U9)	24 (3U4)	28 (3U6)	31 (5T9)
9	132.8	136.6	143.8	141.5	135.3	121.6	131.9
25	166.9	174.3	186.2	180.8	171.7	151.1	164.9
40	181.3	191.3	205.6	200.0	189.1	164.4	181.8
60	191.4	203.7	220.7	215.2	201.3	174.3	193.9
76	194.2	207.9	227.2	221.1	205.7	177.6	198.0
94	194.1	209.3	229.2	223.3	207.2	178.1	199.6
117	190.7	206.2	225.4	218.5	201.8	173.4	194.2
140	170.2	183.9	201.7	195.9	177.7	151.8	171.5
150	150.6	160.8	178.3	174.4	155.4	130.8	150.7

Table 5-4. Model results for temperatures at thermocouple locations – Convective Boundary Condition.

Thermocouple Temperature Predictions Convection Boundary Condition (°C)														
	2 (3K7)		6 (30A)		14 (57A)		19 (3U9)		24 (3U4)		28 (3U6)		31 (5T9)	
Axial Level (in.)	STAR-CCM+	COBRA-SFS												
9	157.8	153.3	160.4	156.6	170.8	156.7	169.1	155.8	160.9	155.4	156.4	153.1	157.3	152.9
25	191.2	190.6	198.7	200.8	211.7	206.1	207.7	203.7	195.5	197.0	188.3	187.9	191.2	189.8
40	208.4	207.4	218.7	221.0	234.1	229.6	232.1	227.2	215.2	216.4	199.6	203.7	207.0	206.8
60	221.6	219.5	232.7	235.3	253.5	246.7	250.8	244.5	229.4	230.2	212.3	215.1	217.7	219.1
76	222.5	222.4	238.4	238.9	259.4	251.0	258.3	249.0	231.6	233.7	213.5	217.8	220.6	222.1
94	223.7	224.5	237.9	241.6	261.6	254.5	258.5	252.5	231.9	236.3	212.1	219.7	223.3	224.2
117	218.1	218.8	232.5	235.5	257.3	248.1	252.1	246.1	225.2	230.2	204.0	214.0	215.4	218.4
140	183.6	197.4	210.0	212.2	239.9	224.3	236.7	222.9	206.1	207.5	171.1	193.0	171.3	197.2
150	143.8	171.7	150.1	185.2	187.1	198.0	197.3	198.4	173.2	181.8	138.0	167.6	145.8	172.1

Table 5-5. Differences between model predictions and measured temperatures at thermocouple positions – Convective Boundary Condition.

Prediction - Measured Convection Boundary Condition (°C)														
	2 (3K7)		6 (30A)		14 (57A)		19 (3U9)		24 (3U4)		28 (3U6)		31 (5T9)	
Axial Level (in.)	STAR-CCM+	COBRA-SFS												
9	25.0	20.5	23.8	20.0	27.0	12.9	27.6	14.3	25.6	20.1	34.8	31.5	25.4	21.0
25	24.3	23.7	24.4	26.5	25.5	19.9	26.9	22.9	23.8	25.3	37.2	36.8	26.3	24.9
40	27.1	26.1	27.4	29.7	28.5	24.0	32.1	27.2	26.1	27.3	35.2	39.3	25.2	25.0
60	30.2	28.1	29.0	31.6	32.8	26.0	35.6	29.3	28.1	28.9	38.0	40.8	23.8	25.2
76	28.3	28.2	30.5	31.0	32.2	23.8	37.2	27.9	25.9	28.0	35.9	40.2	22.6	24.1
94	29.6	30.4	28.6	32.3	32.4	25.3	35.2	29.2	24.7	29.1	34.0	41.6	23.7	24.6
117	27.4	28.1	26.3	29.3	31.9	22.7	33.6	27.6	23.4	28.4	30.6	40.6	21.2	24.2
140	13.4	27.2	26.1	28.3	38.2	22.6	40.8	27.0	28.4	29.8	19.3	41.2	-0.2	25.7
150	-6.8	21.1	-10.7	24.4	8.8	19.7	22.9	24.0	17.8	26.4	7.2	36.8	-4.9	21.4

Comparing surface temperature results is a good way to gain a broad estimate of how the model is performing and whether an appropriate boundary condition has been specified. In this case, it can also help determine if the convective boundary condition is the source of the difference seen between the predicted and measured temperatures in Table 5-5. Figure 5-4 shows the locations where surface temperature values were measured. Table 5-6 shows a comparison of measurements and COBRA-SFS and STAR-CCM+ model predictions of surface temperatures at these locations. In the calculations with the convective boundary condition, both simulations performed well in predicting surface temperatures. Figure 5-5 shows these model predictions plotted as a difference relative the measured value. This plot suggests that the convective boundary condition is less of a cause for differences in model versus measured temperatures in the STAR-CCM+ model than it may be with COBRA-SFS.

Attachment 1 - Test Cask Exterior Temperature Monitoring Locations

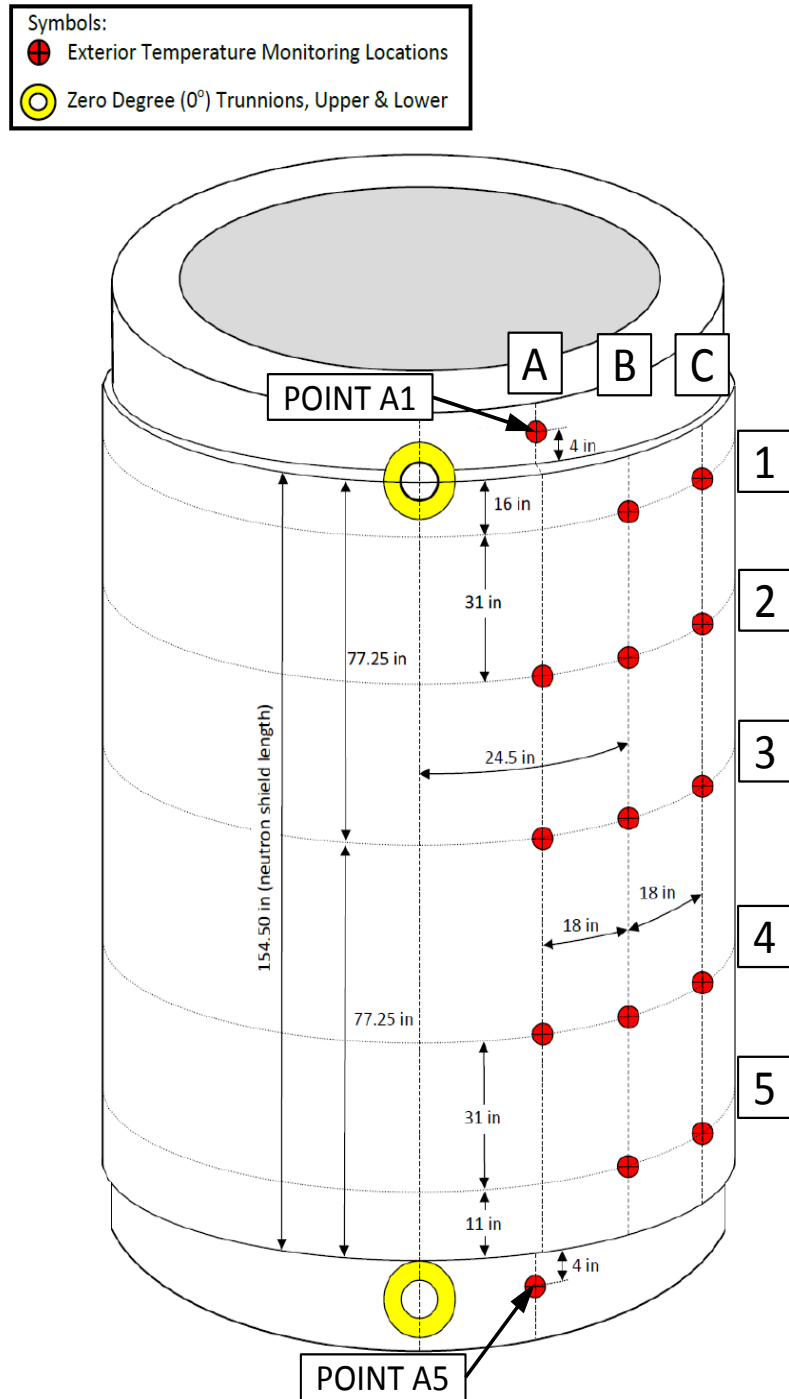


Figure 5-4. Cask surface measurement locations.

Table 5-6. Comparison of model predictions with measured surface temperatures (°F).

Predicted and Measured Surface Temperatures (°F)										
Axial Location		COBRA-SFS			STAR-CCM+			Data		
ID (Fig. 5.4)	Level (in.)	A	B	C	A	B	C	A	B	C
5	11		190.4	190.4	189.2	177.8	178.4	165.5	163	163.5
4	42	195.4	195.4	195.4	184.6	185.2	185.9	181.0	177.5	179.0
3	73	200.5	200.5	200.5	187.7	188.3	189.1	190.5	190.5	189.5
2	103	199.9	199.9	199.9	182.7	183.1	183.8	190.0	189.5	187.5
1	135		193.5	193.5	187.3	171.3	171.8	168.0	176.5	176.0

The STAR-CCM+ model predicts surface temperatures above the measured data by 15 °F near the bottom of the cask, and approximately 5 to 7 °F below the measured data near the top of the cask. The difference near the mid-height of the cask, where the highest cladding temperatures would be expected, was 5 to 7 °C *below* the measured values. Since the model predicts fuel temperatures that are well above measurements, the treatment of the surface boundary does not appear to be a factor in those differences.

The COBRA-SFS temperature predictions show a consistently high trend compared to the measured temperatures. Predicted surface temperatures at each location range from 10 °F to 25 °F above the measured value. Near the mid-height of the cask the model estimates are approximately 10 °F high. While this may account for some of the difference between estimated and measured fuel temperatures in the COBRA-SFS model, it would only be part of the explanation.

The differences between the estimated and measured surface temperatures shown in Figure 5-5 are due to the approximate treatment of the thermal conditions in the decontamination pit. This may be due to the convection correlation used for the side boundary. The COBRA-SFS model uses a correlation for free convection over a cylinder. The experimental setup has various aspects that may challenge the applicability of this correlation. The correlation is derived for free convection to an essentially infinite ambient. Within the decontamination pit, this assumption is compromised by the proximity of the walls and the presence of the work platform, which closes off vertical air flow near the top of the cask. The treatment of thermal radiation in this environment is similarly approximate. To eliminate the approximations in these boundary conditions, measured temperatures can be used in their place. This is discussed in the next section.

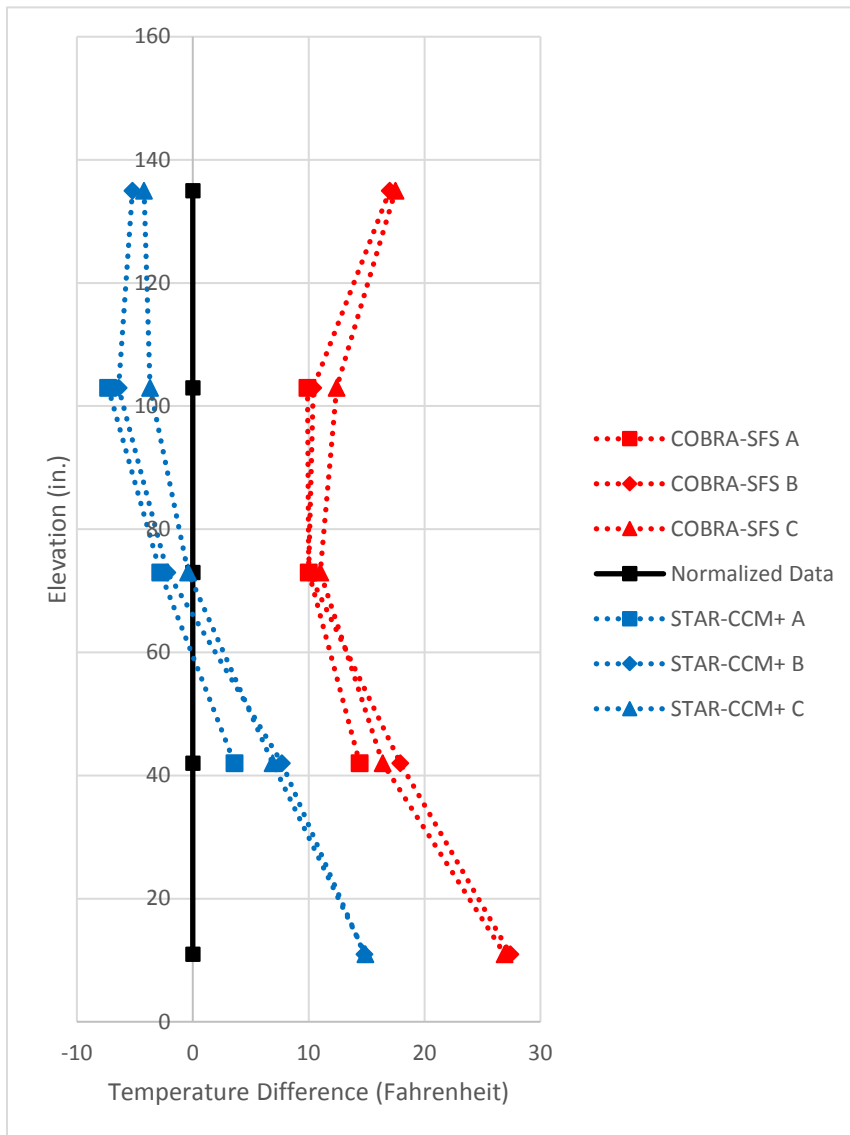


Figure 5-5. Normalized surface temperature predictions relative to measured data.

5.2.2 Blind Model Results Using Measured Surface Temperature as Boundary Conditions

The modeling results presented in this section use the measured temperatures on the cask surface as a boundary condition. Because of this, the model predictions at the thermocouple locations within the fuel assemblies are expected to be as accurate as possible, within the constraints of this modeling exercise. Recognize that the surface temperatures are only measured a fixed number of locations and only on one side of the cask, so any variation around the cask circumference is not imposed as a boundary condition on the model and its impact will not be seen in the temperatures inside the cask.

The peak cladding temperatures estimated by each model are shown first, in Figure 5-6.

	218	227	225	214	
215	236	248	247	236	215
221	247	237	251	248	226
226	247	247	239	248	226
219	235	248	248	237	219
	219	228	226	215	

COBRA-SFS

	207	230	227	202	
210	236	253	253	236	211
226	256	240	258	257	233
233	257	255	243	257	233
217	234	254	253	236	216
	208	230	227	203	

STAR-CCM+

Figure 5-6. Estimated peak fuel cladding temperatures – measured temperature boundary condition.

Model predictions for temperatures at the thermocouple locations are shown in Table 5-7. The differences between model results and measured values are shown in Table 5-8. The difference is less than with the convective boundary condition, ranging from 10 to over 30 °C, but this difference is still unexpectedly high.

Except at the ends, the blind predictions from both models showed good agreement with the trends of the data. However, they did not show good agreement on the magnitude of the recorded temperatures. Potential reasons for this are discussed further in Section 5.3.

An important indicator of agreement between model predictions and TC measurements is the shape of the axial temperature profiles, which are illustrated in Figure 5-7 over the full length of the instrumented region. This plot is meant to show the collective trends of differences, not individual basket cells. Plots comparing differences for individual basket cells are included in Appendix B. Figure 5-8 illustrates these profiles over the central region of the instrumented length. Figure 5-7 shows that the normalized temperature difference profile for COBRA-SFS has a relatively constant offset from the data. The STAR-CCM+ profile shows a similar trend, but it deviates from this trend at the 140 and 150-inch level. Taking both models together from 40 to 117 inches, as shown in Figure 5-8, the trend is very linear. This is positive for the model's agreement with data because the central axial region of the fuel is expected to best agree with the data due to simplifications in modeling the plenum region of the cask in COBRA-SFS and simplifications in modeling the ends of the fuel assemblies in STAR-CCM+.

Table 5-7. Model results for temperatures at thermocouple locations – measured temperatures as surface boundary condition.

Thermocouple Temperature Predictions Surface Temperature Boundary Condition (°C)														
	2 (3K7)		6 (30A)		14 (57A)		19 (3U9)		24 (3U4)		28 (3U6)		31 (5T9)	
Axial Level (in.)	STAR-CCM+	COBRA-SFS												
9	145.3	144.0	146.1	147.1	157.1	147.0	156.7	146.2	147.6	145.9	143.0	143.8	143.2	143.6
25	181.1	181.8	186.6	191.9	199.4	197.1	196.9	194.6	184.4	188.1	178.0	179.2	179.6	181.0
40	200.5	199.1	209.1	212.5	223.8	221.0	223.1	218.5	206.3	207.8	192.0	195.3	198.2	198.3
60	216.0	211.7	225.9	227.4	245.7	238.5	243.8	236.2	223.0	222.1	206.8	207.2	211.6	211.1
76	218.3	216.4	233.2	232.9	253.3	245.1	252.7	243.0	226.8	227.5	209.5	211.5	216.1	215.8
94	220.0	217.3	234.1	234.2	256.8	246.9	253.9	244.9	228.0	228.7	208.7	212.3	219.7	216.8
117	212.0	211.6	230.1	228.2	253.2	240.7	248.0	238.6	220.8	222.8	200.4	206.7	212.3	211.1
140	165.0	190.2	210.7	204.9	236.5	217.0	230.2	215.6	193.7	200.2	168.1	185.7	172.9	189.8
150	133.2	164.2	167.0	177.8	192.8	190.6	176.5	190.9	155.7	174.3	132.9	159.9	143.3	164.5

Table 5-8. Differences between model predictions and measured temperatures at thermocouple positions – measured temperatures as surface boundary condition.

Prediction - Measured Surface Temperature Boundary Condition (°C)														
	2 (3K7)		6 (30A)		14 (57A)		19 (3U9)		24 (3U4)		28 (3U6)		31 (5T9)	
Axial Level (in.)	STAR-CCM+	COBRA-SFS												
9	12.5	11.2	9.5	10.5	13.3	3.2	15.2	4.7	12.3	10.6	21.4	22.2	11.3	11.7
25	14.2	14.9	12.3	17.6	13.2	10.9	16.1	13.8	12.7	16.4	26.9	28.1	14.7	16.1
40	19.2	17.8	17.8	21.2	18.2	15.4	23.1	18.5	17.2	18.7	27.6	30.9	16.4	16.5
60	24.6	20.3	22.2	23.7	25.0	17.8	28.6	21.0	21.7	20.8	32.5	32.9	17.7	17.2
76	24.1	22.2	25.3	25.0	26.1	17.9	31.6	21.9	21.1	21.8	31.9	33.9	18.1	17.8
94	25.9	23.2	24.8	24.9	27.6	17.7	30.6	21.6	20.8	21.5	30.6	34.2	20.1	17.2
117	21.3	20.9	23.9	22.0	27.8	15.3	29.5	20.1	19.0	21.0	27.0	33.3	18.1	16.9
140	-5.2	20.0	26.8	21.0	34.8	15.3	34.3	19.7	16.0	22.5	16.3	33.9	1.4	18.3
150	-17.4	13.6	6.2	17.0	14.5	12.3	2.1	16.5	0.3	18.9	2.1	29.1	-7.4	13.8

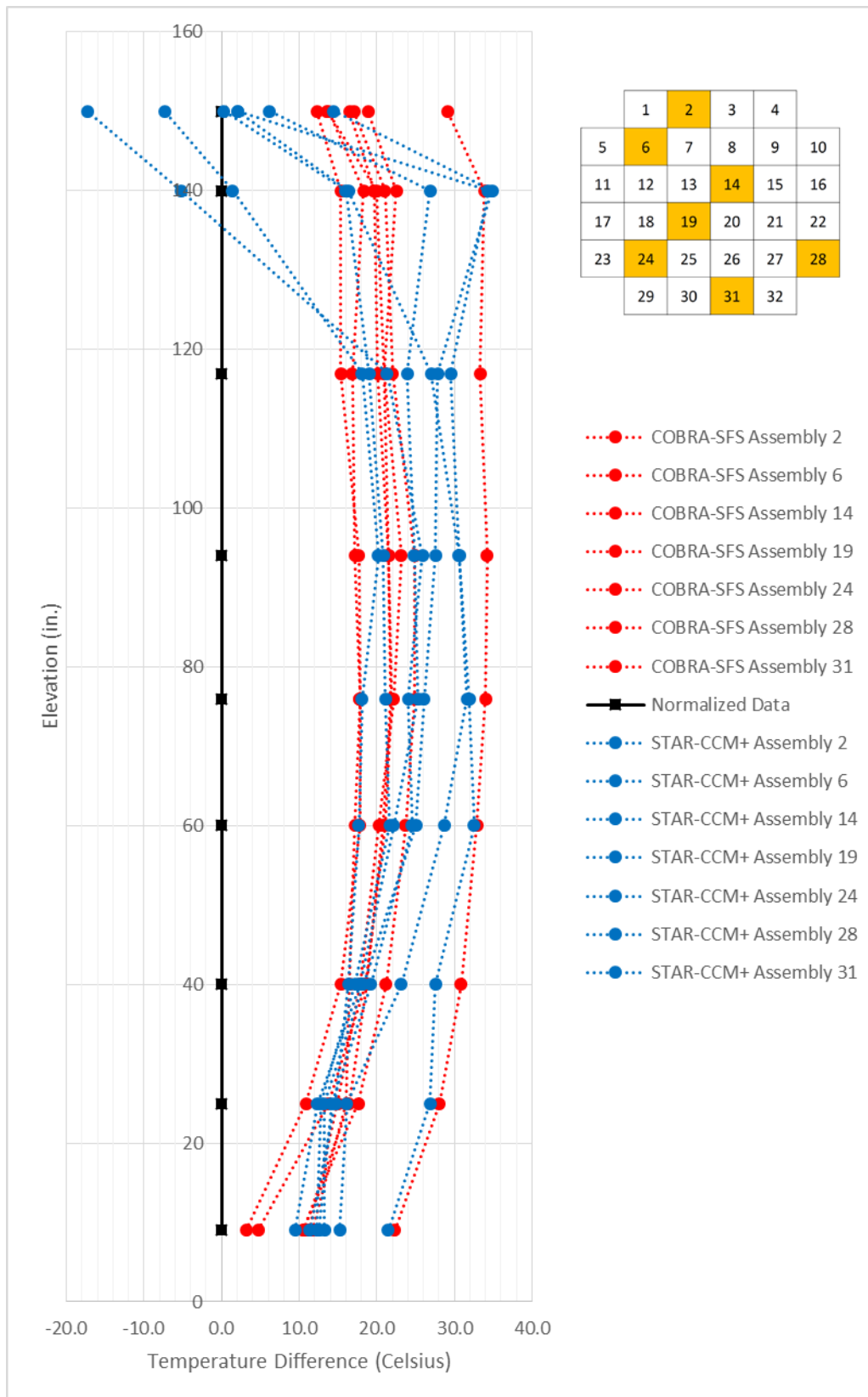


Figure 5-7. Normalized comparisons of temperatures at all thermocouple locations.

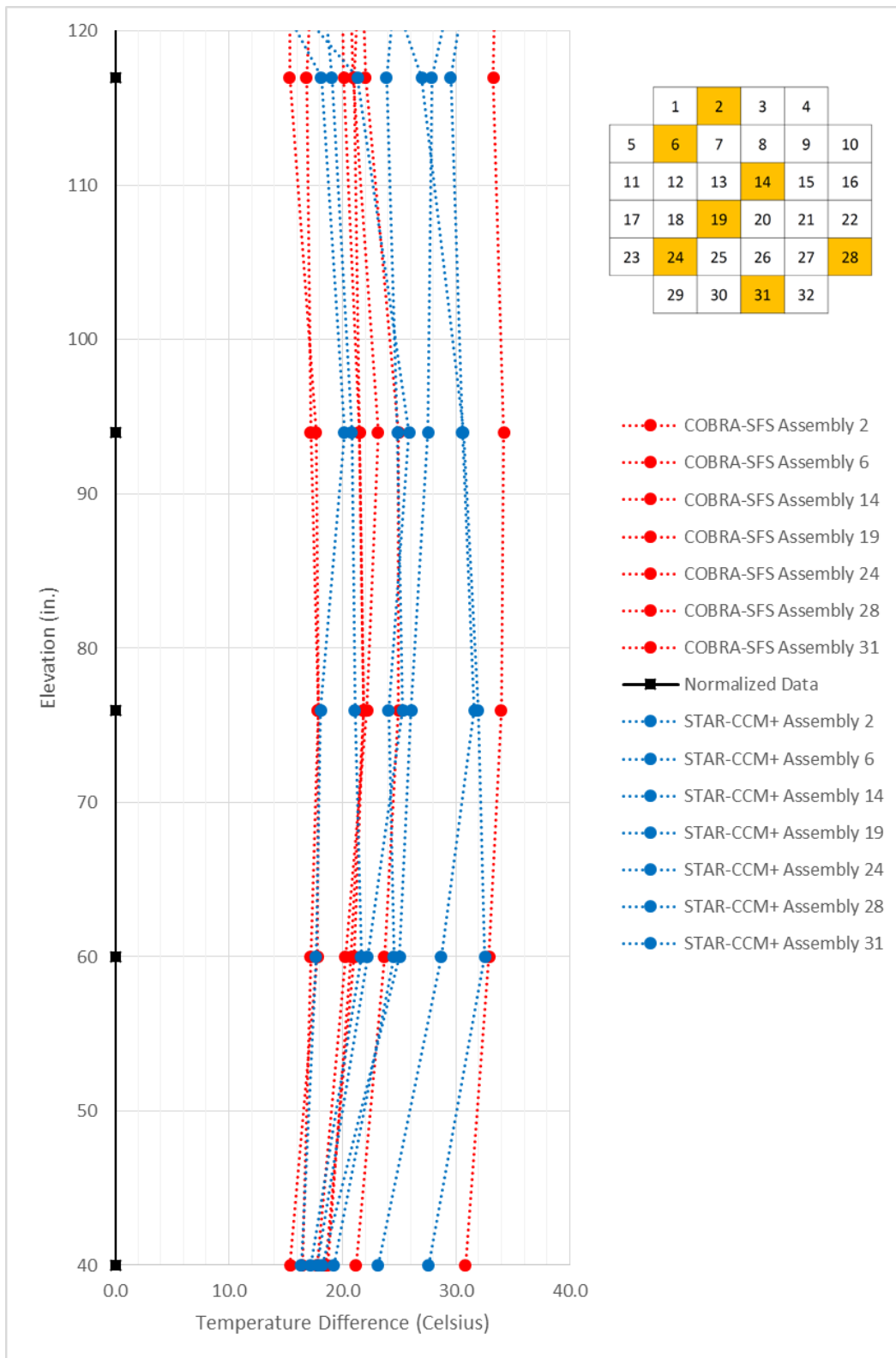


Figure 5-8. Normalized comparisons of temperatures at central thermocouple locations (40-117 in.).

The STAR-CCM+ analysis showed a significant drop in predicted temperatures relative to measurements at the uppermost thermocouple locations in the outer assemblies. This variation is likely due to two effects. One is the presence of recirculation within the basket rails in the model predictions. Due to the lack of bulk flow through the basket rails, in the model a stable recirculation pattern is predicted, as shown in Figure 5-9. This recirculation pattern is not predicted in the COBRA-SFS model due to the noding scheme used. Another factor contributing to the lower predicted temperature at the top is the interaction of the K_{eff} /porous media model with the helium flow model used in the STAR-CCM+ analysis.

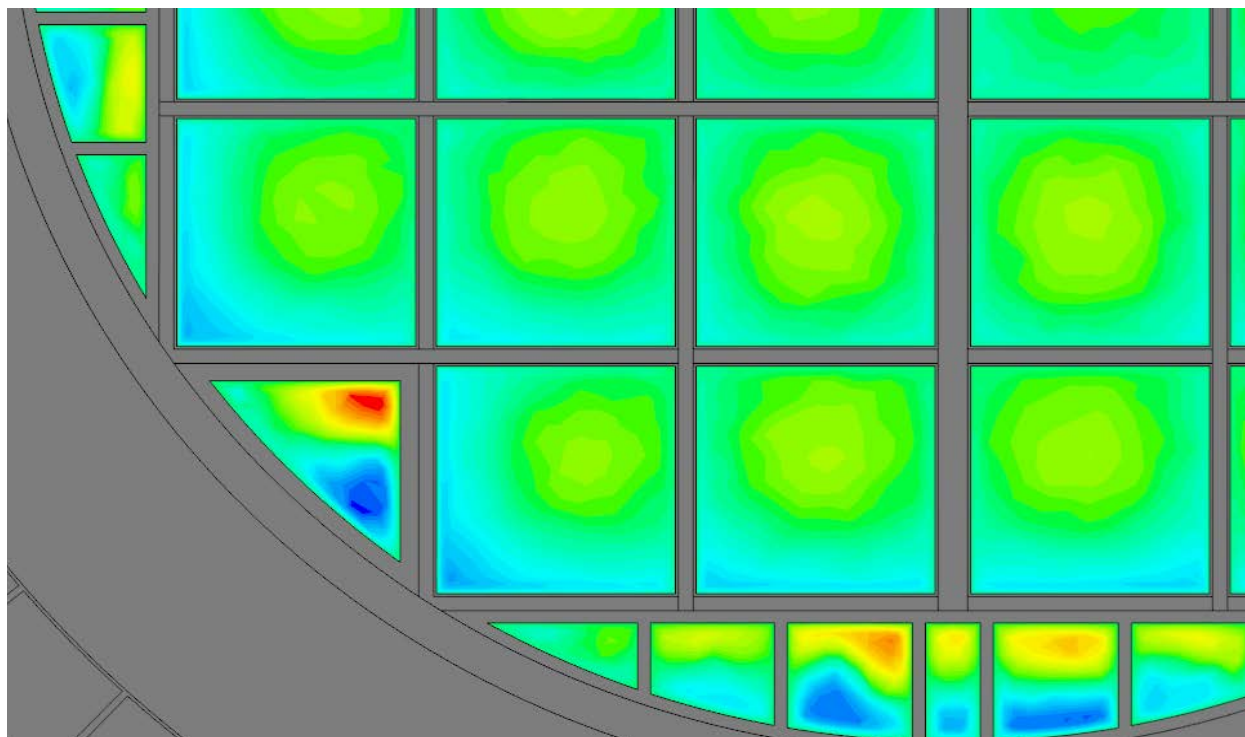


Figure 5-9. Gas vertical velocity across basket at axial level of maximum fuel temperature.

5.3 Non-Blind Sensitivity Runs

After examining results from the experimental data, a number of sensitivity tests were conducted to investigate causes of the differences between the modeling results and measured data. The results of these sensitivity tests for the COBRA-SFS model are shown in Table 5-9.

Changes in emissivity of the basket walls showed little effect on PCT. This is due primarily to the low temperature of the demonstration cask. Thermal radiation is dependent on a $(T_2^4 - T_1^4)$ relationship. Consequently, the change in emissivity would be greater at the higher temperature gradients that would result from higher overall temperatures. The original basket emissivity was a relatively low 0.22; increasing the emissivity to 0.8 to simulate a significantly roughened or damaged cask does not have a large effect in this case.

Sensitivity of assembly rod temperatures to decay heat is well documented, and for any cask design is in many cases the most sensitive single parameter. However due to the high-fidelity depletion and decay calculations utilized for estimating decay heats for this modeling effort, the uncertainty in the decay heat values used in these models is no more than $\pm 2\%$. In this case that difference is not sufficient to explain the differences between TC measurements and model predictions.

The effect of thermal gap resistances was also investigated. Both models include a number of these (for example, see Section 2.2.6). The gaps in the basket are helium filled and those between layers of the cask and neutron absorber components are air filled. The gaps between the rails and cavity shell are represented as very tight in the original models due to the construction of the cask. Because this gap is already very nearly closed, it is expected that there would be very little temperature change as a result of reducing it to zero.

The main source of uncertainty in the modeling is believed to be the representation of the gap between the basket and the rails. As can be seen from the results presented in Table 5-9 the models show a great deal of sensitivity to changes in this parameter. The baseline used in this comparison is the blind model prediction PCT from Section 5.2.2. The basket-rail gap was specified in the TN-32B UFSAR (2012) as being at thermal equilibrium. With further investigation, it is clear that the UFSAR value is conservatively large, and there is a relatively small gap in the actual demo cask. A nominal gap width of 0.10 inch is suggested as a reasonable best estimate approximation (see Section 5.4).

Additionally, there is a significant over-simplification in the modeling of the gap size generally. The input value is assumed uniform throughout the model, but in reality, the gap between rail and basket varies both axially and circumferentially. This is not taken into account in the modeling and may have a significant effect on predicted temperature distributions as well as local temperature values.

Table 5-9. Sensitivity results with COBRA-SFS model.

Condition	PCT Difference from Baseline (°C)
Increase Basket Emissivity 0.22 to 0.8	-2
Closed rail-shell gaps	-2
99% Decay Heat	-2
98% Decay Heat	-3
95% Decay Heat	-8
90% Decay Heat	-16
Basket-Rail Gap 0.15 in.	-5
Basket-Rail Gap 0.10 in.	-12
Basket-Rail Gap 0.05 in.	-20

Additional sensitivity tests were completed with the STAR-CCM+ model, and comparable results consistent with the results obtained in the COBRA-SFS model sensitivity studies were obtained. These are summarized in Table 5-10. In addition to the change in PCT, this table includes the change in the predicted temperature at the location of thermocouple TC7 in the hottest assembly. This measurement location is toward the bottom of the thermocouple lance and the change in temperature at this location relative to that of the PCT is a measure of change in skew of the axial profile. The results in Table 5-10 show the temperature at this lower measurement location tracked with the changes in the PCT for parameter changes that impacted radial heat transfer. For parameter changes that effected axial heat transfer, specifically the bottom air gap and boundary condition at the base, the difference in temperature was greater at the lower thermocouple position, as should be expected.

Table 5-10. Sensitivity results with STAR-CCM+ model.

Condition	PCT Difference from Baseline, °C	57A, TC7 Difference from Baseline, °C
Add thermal radiation between cask bottom and floor	-3.5	-7.3
Decrease Al emissivity from 0.2 to 0.1	0.1	0.2
Increase CS emissivity to 0.8, SS emissivity to 0.4	-0.8	0.0
Close air gap between liner base and gamma shield	-1.4	-4.5
Eliminate small air gap between liner OD and gamma shield	-0.7	-0.7
Reduce helium gap between rail and basket from UFSAR value to 0.1 in.	-16.1	-17.5

As noted in Section 5.1.2.2, the boundary condition at the bottom of the cask includes only natural convection to the 24°C (75°F) ambient. Because of the confined space and expected higher local air temperatures, it was assumed reasonable to neglect thermal radiation from this surface. The results in Table 5-10 show that radiation from the bottom of the cask to a 24°C (75°F) surface makes a significant difference in the predicted temperatures at these two locations. The PCT is lower by 3.5 °C and is at the location of TC7 is lower by 7.3 °C, indicating an even greater temperature reduction in the lower portion of the fuel assembly. This is consistent with a shift in heat transfer at the base. However, this is still believed to be an unrealistic addition considering the way in which convection is being treated from the same boundary. A more refined modeling treatment of this region could be performed, but based on this sensitivity test result, the magnitude of change in PCT would be expected to be relatively small, within only a few degrees Celsius.

Sensitivity tests also investigated changes to surface emissivity values. Depending upon surface condition, the emissivity of aluminum is often less than the value used in the base model (0.2). But the results in Table 5-10 show that decreasing this parameter to the lower bounding value of 0.1 makes an insignificant change in the temperatures predicted with this model. Similarly, increasing the emissivity of carbon steel to 0.8, based on expected properties of the spray-coated surface, and simultaneously increasing the emissivity of the stainless-steel surface to a typical value of 0.4 showed only minimal effect on predicted temperatures. The predicted PCT decreased by less than 1 °C, and there was no discernable change in the predicted temperature at that TC location.

As observed in the COBRA-SFS model, the STAR-CCM+ model was sensitive to changes in gap resistance. A significant change was observed only when changing the basket to rail gap, reducing it from the value assumed in the UFSAR to 0.1 inches. As shown in Table 5-10, the PCT decreased by over 16 °C. For this same change in gap width, the COBRA-SFS model gave a comparable (12 °C) decrease in PCT. The air gap between the liner base and the bottom gamma shield is assumed to be of similar magnitude in the UFSAR, but it is not in the principal direction of heat transfer and the change in PCT even when that gap is essentially closed is still modest. The air gap between the liner outside diameter (OD) and the cylindrical gamma shield is in the principal direction of heat transfer, however it is already assumed to be small, so closing it results in a similarly modest change in PCT.

5.4 Adjusted Best Estimate Case

Based on results from the sensitivity studies and the further details obtained on cask construction information, a final analysis run, termed the “adjusted best estimate” was conducted with the basket-rail gap set at 0.10 inch. Although further reduction of the gap could put the modeling results in close agreement with the measured data, there is insufficient information to justify this assumption, as there is no actual measurement of the basket-rail gap available. In this case it is reasonable to bring the results closer to the data by means of defensible revisions to the model inputs, but still maintain conservatism with respect to cladding temperature.

Only COBRA-SFS results are presented here for the adjusted best estimate case, for clarity. However, the change in STAR-CCM+ results are consistent with the change in COBRA-SFS results, providing further confidence in the validity of this approach. Thermocouple data comparisons are shown in Figure 5-10. Predicted peak cladding temperatures for all assemblies are shown in Figure 5-11 and a histogram of the cladding temperature within the cask is shown in Figure 5-12.

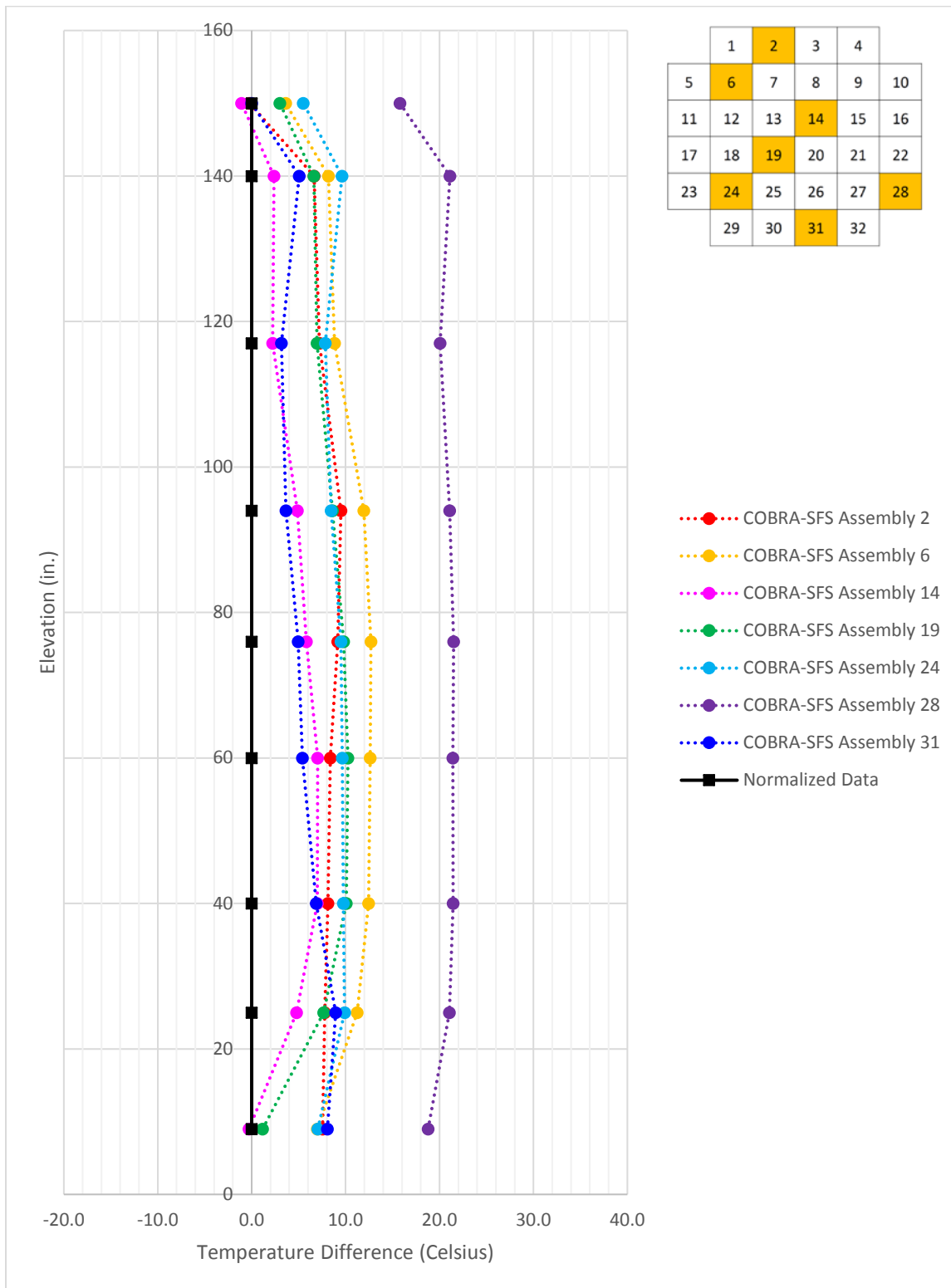


Figure 5-10. Adjusted best estimate results for thermocouple locations from COBRA-SFS model.

	205	214	211	201	
201	224	235	235	223	202
208	235	224	238	235	213
213	235	235	227	235	213
206	222	236	235	224	206
	206	215	213	202	

Figure 5-11. Adjusted best estimate peak cladding temperatures from COBRA-SFS model.

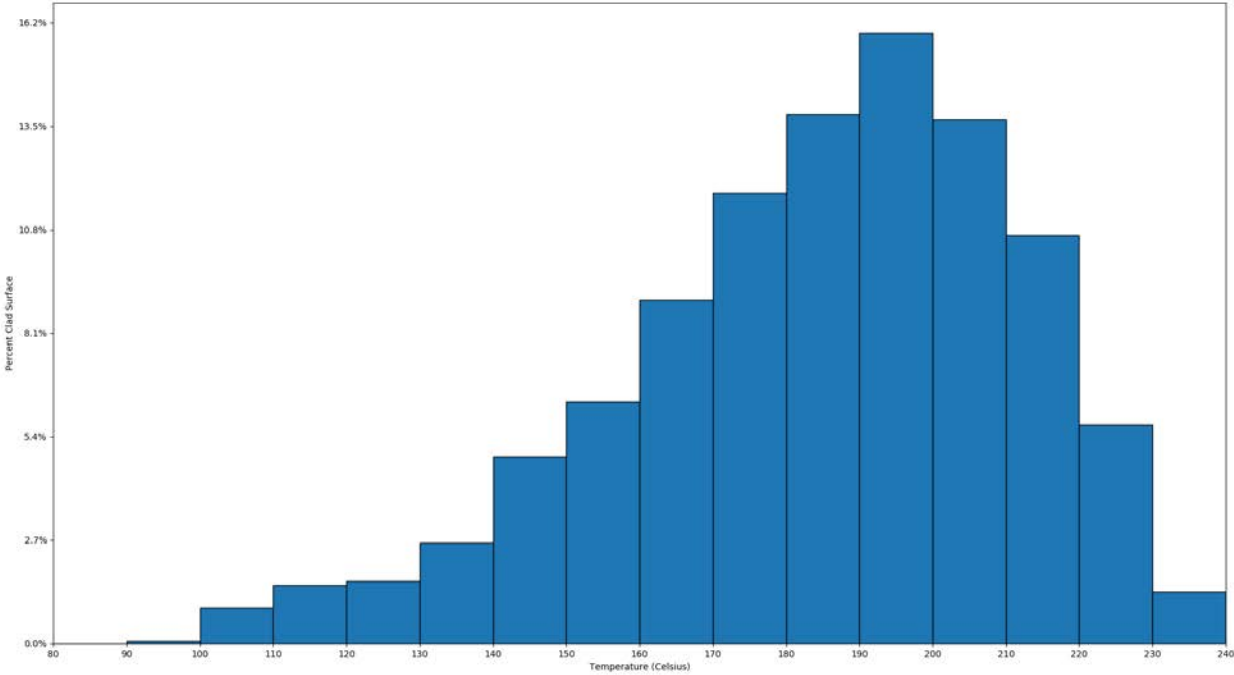


Figure 5-12. Adjusted best estimate cladding surface temperature distribution from COBRA-SFS model.

6. CONCLUSIONS AND RECOMMENDATIONS

This section presents conclusions and recommendations from this study.

6.1 Conclusions

The results of this study support the following conclusions:

- Thermal models were successfully used to help plan the dry storage cask demonstration.
- This success was aided by running two independent models with consistent input values. This approach helped to identify and correct modeling errors.
- The different modeling strengths of the two models were useful when project interest ranged from the details of fuel performance to limits for cask components.
- Decay heat estimates were found to vary widely depending on the methodology used. Estimates of assembly decay heats calculated using fuel burnup data were 17% lower than the conservative values initially provided by the utility.
- Accurate values for assembly decay heat are essential for reliable peak fuel cladding temperatures. The effect of axial power profile, pin-by-pin decay heat distribution versus assembly-averaged values, and pin and assembly geometry, are of secondary importance.
- Both models produced equivalent trends of peak fuel cladding temperature with ambient temperature (approximately 0.65 degree change in PCT per degree change in ambient temperature).
- When comparing model predictions and measurements for fuel temperatures following cask loading and a two-week thermal soak, blind model predictions over-predicted temperatures at measurement locations by between 20 to 40°C.
- Subsequent model runs to examine input parameter sensitivity suggest that, for this cask, fuel temperatures are strongly dependent on thermal resistances through gaps in the main radial heat transfer paths through the basket and support structure. Specifically, a reduction of the basket to rail gap to 0.1 inches reduced the temperature over-prediction to less than 12°C for all but one assembly.

6.2 Recommendations

Recommended follow-on activities include:

- Utilize the vacuum drying details for the demonstration cask in conjunction with temperature data from the thermocouple lances to test and refine vacuum drying models. This could include complete vacuum drying simulations using pool and ambient temperature data and recorded drying times. Comparing these results with measured fuel temperatures could allow development of needed refinements to the models.
- Run thermal simulations of the demonstration cask on the ISFSI pad and compare with fuel temperature data as it becomes available. Periods of quiescent weather conditions during cold and hot periods would be useful tests of steady-state model predictions. Transient simulations could also be run to study response to diurnal changes, to determine if there is any significant effect on fuel temperatures, and to evaluate fuel temperature response to sudden or sustained temperature changes.

This page is intentionally left blank.

7. REFERENCES

- 10 CFR 71. 2003. "Packaging and Transportation of Radioactive Material." *Code of Federal Regulations*, U.S. Nuclear Regulatory Commission, Washington, D.C.
- Bahney III, RH and TL Lotz. 1996. *Spent Nuclear Fuel Effective Thermal Conductivity Report*. BBA000000-01717-5705-00010 Rev. 00, TRW Environmental Safety Systems, Inc., Fairfax, Virginia.
- Brewster RA, E Volpenhein, E Baglietto, and CS Bajwa. 2012. "CFD Analyses of the TN-24P PWR Spent Fuel Storage Cask," PVP-2012-78491, in *Proceedings of the ASME 2012 Pressure Vessels and Piping Division Conference*, Toronto, Canada.
- Cuta JM, SR Suffield, JA Fort, and HE Adkins. 2013. *Thermal Performance Sensitivity Studies in Support of Material Modeling for Extended Storage of Used Nuclear Fuel*. Fuel Cycle Research and Development, U.S. Department of Energy, Used Fuel Disposition Campaign. FCRD-UFD-2013-000257. PNNL-22646.
- Dassault Systemes SolidWorks® Corp. 2011. SolidWorks® Premium 2011 x64 Edition (computer software). Dassault Systemes, Waltham, Massachusetts.
- DOE/RW-0184. 1987. Characteristics of Spent Fuel, High-Level Waste, and Other Radioactive Wastes Which May Require Long-term Isolation. **Appendix 2A**. Physical Descriptions of LWR Fuel Assemblies. Volume 3 of 6. U.S. Department of Energy, Office of Civilian Radioactive Waste Management.
- DOE/RW-0472. 1998. *Topical Report on Actinide-Only Burnup Credit for PWR Spent Nuclear Fuel Packages*. DOE/RW-0472, Revision 2, Office of Civilian Radioactive Waste Management, Washington, D.C.
- EPRI. 2014. High Burnup Dry Storage Cask Research and Development Project – Final Test Plan. Contract No. DE-NE-0000593, Electric Power Research Institute, Palo Alto, California.
- Fort JA, JM Cuta, SR Suffield, HE Adkins. 2015. Thermal Modeling of Proposed Tn-32b Cask for High Burnup Fuel Storage Demonstration Project. Fuel Cycle Research & Development, U.S. Department of Energy Used Fuel Disposition Campaign. FCRD-UFD-2015-000119, PNNL-24549. Prepared by Pacific Northwest National Laboratory, Richland, Washington.
- Gauld IC, SM Bowman, and JE Horwedel. 2009. *ORIGEN-ARP: Automatic Rapid Processing for Spent Fuel Depletion, Decay, and Source Term Analysis*. ORNL/TM-2005/39, Oak Ridge National Laboratory, Oak Ridge, Tennessee.
- Holman JP. 1997. *Heat Transfer*. 8th ed. McGraw-Hill, New York City, New York.
- Incropera FP, DP Dewitt, TL Bergman, and AS Lavine. 2007. *Fundamentals of Heat and Mass Transfer*. 6th ed. John Wiley & Sons, Hoboken, New Jersey.
- Lombardo NJ, JM Cuta, TE Michener, DR Rector, and CL Wheeler. 1986. *COBRA-SFS: A Thermal-Hydraulic Analysis Computer Code; Volume III: Validation Assessments*. PNL-6049, Vol. 3, Pacific Northwest Laboratory, Richland, Washington.
- Michener TE, DR Rector, JM Cuta, and HE Adkins, Jr. 2017. *COBRA-SFS: A Thermal-Hydraulic Code for Spent Fuel Storage and Transportation Casks, Cycle 4a*. PNNL-24841, Pacific Northwest National Laboratory, Richland, Washington.
- Michener TE, DR Rector, JM Cuta, RE Dodge, and CW Enderlin. 1995. *COBRA-SFS: A Thermal-Hydraulic Code for Spent Fuel Storage and Transportation Casks*. PNL-10782, Pacific Northwest National Laboratory, Richland, Washington.

NRC. 2003. U.S. Nuclear Regulatory Commission, Interim Staff Guidance-11, Revision 3, Cladding Considerations for the Transportation and Storage of Spent Fuel, NRC Spent Fuel Project Office.

NRC. 2010. *Standard Review Plan for Spent Fuel Dry Storage Systems at a General License Facility*, NUREG-1536, Revision 1. U.S. Nuclear Regulatory Commission, Office of Nuclear Material Safety and Safeguards. Washington, D.C.

Rector DR and TE Michener. 1989. *COBRA-SFS Modifications and Cask Model Optimization*. PNL-6706, Pacific Northwest Laboratory, Richland, Washington.

Roache PJ. 2009. *Fundamentals of Verification and Validation*, Hermosa Publishing, Socorro, New Mexico.

Siemens, PLM. 2016. STAR-CCM+ 11.06 (computer software). Siemens Product Lifecycle Management Software, Inc., Plano, Texas.

UFSAR TN-32. 2012. "Updated Final Safety Analysis Report." Rev. 5, Transnuclear, Inc., Columbia, Maryland.

Appendix A

INPUTS PROVIDED TO BLIND CASK LOAD MODELING PARTICIPANTS

This page is intentionally left blank.

This appendix contains a verbatim listing of input descriptions provided to all modeling participants on January 31, 2018.

Additional clarifications were provided after that date, regarding:

1. Cask surface measurement locations.
2. Basket orientation relative to cask surface measurement locations.

Finally, surface temperature measurements were provided to all participants.

***DRAFT* Thermal Modeling Round Robin Phase 2b Input**

Objective: To determine uncertainties in component temperatures calculated using different thermal modeling approaches. To do this, the TN-32B system loaded at the North Anna Nuclear Generating Station on November 14, 2017 will be modeled by different parties in a blind study where participants have not been informed of the temperatures measured to date. Each party will use the same input parameters. While decay heat is the largest single contributor to thermal performance, each party will use the decay heats provided in this input. Participants will calculate decay heats separately as part of Phase 2a.

Tasks: Each party will perform the following tasks and submit the results to the EPRI Thermal Subcommittee. EPRI will combine and compare the results with each other and with the data recorded from the TN-32B Research Project Cask. Peak and minimum temperatures are of most interest, but distributions should be provided.

1. Steady-state component temperatures for vacuum conditions (assume a vacuum <1 torr).
 - a. PNNL/NRC Only – Milestone Deliverable Date: February 28, 2018
 - b. Vary interior environment (assume water vapor contamination of 0.01%, 0.1%, and 1.0% for sensitivity)
 - c. Model with and without poison rod assemblies (k_{eff} difference)
 - d. Actual component temperatures using the assumed ambient air temperatures ([60°F] and [65°F]) as the boundary conditions:
 - i. 63 thermocouple lance locations (temps at the 9 axial locations in the 7 thermocouple lances located in a guide tube of seven specific assemblies)
 - ii. 32 PCTs from fuel assemblies
 - iii. 4 maximum temperatures
 1. Neutron shield resin
 2. Cask inner wall
 3. Cask outer walls
 4. Top lid seal location
 - e. Note that we did not achieve steady state during the vacuum drying (<7 hour duration), so this is to compare the results of different models but not compare with measured temperatures.
2. Steady-state component temperatures at the end of the thermal soak period of the Research Project Cask in the decon pit at North Anna.
 - a. PNNL/NRC/TN – Milestone Deliverable Date: 2/28/18 & TN (3/31/18)
 - b. Model with and without poison rod assemblies (k_{eff} difference)
 - c. Actual component temperatures using the assumed ambient air temperatures ([60°F] and [75°F]) as the boundary condition:
 - i. 63 thermocouple lance locations (temps at the 9 axial locations in the 7 thermocouple lances located in a guide tube of seven specific assemblies)
 - ii. 32 PCTs from fuel assemblies
 - iii. 4 maximum temperatures
 1. Neutron shield resin
 2. Cask inner wall
 3. Cask outer walls
 4. Top lid seal location (schematic to be provided by DOE/EPRI)
 - iv. 15 outer wall locations (see Figures A-12, A-13, and A-20)

- d. After completion of c, actual component temperatures using the 15 outer wall location temperatures to be provided as the boundary condition:
 - i. 63 thermocouple lance locations (temps at the 9 axial locations in the 7 thermocouple lances located in a guide tube of seven specific assemblies)
 - ii. 32 PCTs from fuel assemblies
 - iii. 4 maximum temperatures
 1. Neutron shield resin
 2. Cask inner wall
 3. Cask outer walls
 4. Top lid seal location (schematic to be provided by DOE/EPR).
3. GCI/Uncertainty under Phase IIC
 - a. PNNL/NRC – Milestone Deliverable Date: 3/31/18 pending DOE funding
 - b. Feeds discussion on uncertainty analyses for inputs.

Input

Cask: The cask used is the TN-32B. All materials of construction, dimensions, etc. are to be taken from the FSAR (all parties should use TN-32 Updated Final Safety Analysis Report, Revision 6 (Proprietary), Transnuclear Inc., April 2014). (Note that there were no changes from Revision 5 that affect thermal properties or performance.) The lid was modified to allow the insertion of seven thermocouple lances, as shown in Figure A-1. If information is not provided in the FSAR (e.g., emissivity of basket external surface and basket rails), each party should use their experience and use a best estimate and document it as an assumption.

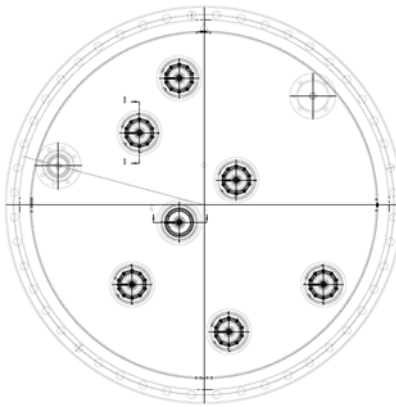


Figure A-1. Location of thermocouple lance penetrations. Note drain port, upper right, and vent port, middle left, are visible.

During the vacuum drying and thermal soak period, the neutron shield, overpressure system, and protective cover are not in place.

Fuel: Fuel was loaded per the loading diagram in Figure A-2. The loading diagram identifies the cell identifier (1-32), if a thermocouple lance or poison rod assembly is in that cell, Assembly ID, assembly design, cladding type, assembly average burnup in GWd/MTU, initial U^{235} enrichment, number of irradiation cycles, years since reactor discharge (as of 11/7/2017), and the decay heat as calculated by Oak Ridge National Laboratory as of November 7, 2017.

Assembly Design: All of the fuel loaded in the Research Project Cask is 17×17 high burnup fuel. All of the assemblies with M5[®] cladding are Orano AMBW design. All of the assemblies with ZIRLO[®] cladding are Westinghouse NAI/P+Z design. The single assembly F40, with Zircaloy-4 cladding is the

Westinghouse LOPAR design. The single assembly, 0A4, with low-Sn Zircaloy-4 cladding is the Westinghouse NAIF design. Much of the assembly design information is proprietary. Participants should use design information as necessary as obtained under Non-Disclosure Agreements with the fuel vendors. A diagram of an old Westinghouse design as obtained in *LWR Nuclear Fuel Bundle Data for Use in Fuel Bundle Handling* (Weihermiller and Allison, PNL-2575, September 1979) is shown in Figure A-2.

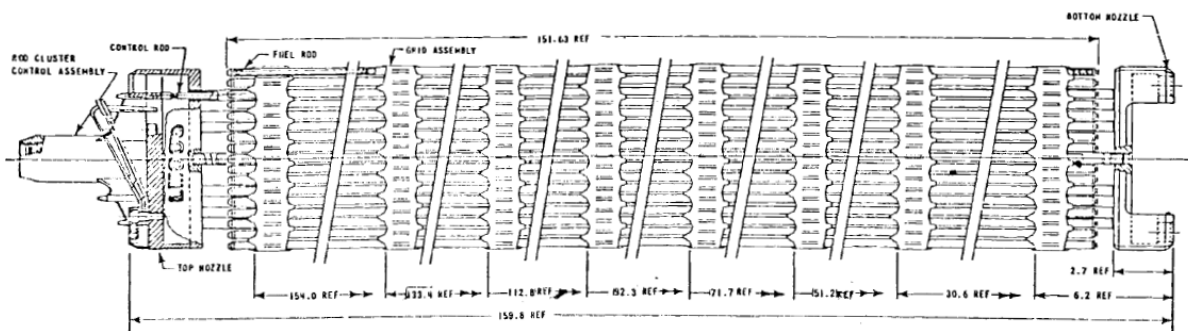


Figure A-2. Schematic of a Westinghouse 17×17 fuel bundle (PNL-2575).

Fuel Rods: Non-proprietary information to use. Note that all dimensions are nominal, as-fabricated (prior to irradiation).

Property	LOPAR	NAIF	NAIF/P+Z	AMBW
Cladding OD (in)	0.374	0.374	0.374	0.374
Fuel rod length (in)	151.635	152.2	152.6	152.16
Active fuel length (in)	144	144	144	144

Assumptions to use:

- Fuel in contact with bottom end plug
- Bottom end plug height of 0.7 inches (so active fuel length begins 0.7 in from bottom of cladding)
- Bottom of all fuel rods (cladding) are 4 inches from the bottom of the cask and are not in contact with the bottom nozzle
 - There are variable heights of the bottom nozzles depending on fuel assembly design; this assumption ignores those variations and variations in rod growth.

	1 6T0 NAIF/P+Z Zirlo, 54.2 GWd 4.25%/3 cy/12.1 yr 912.2 W	2 (TC Lance) 3K7 AMBW M5, 53.4 GWd 4.55%/3 cy/8.7 yr 978.2 W	3 3T6 NAIF/P+Z Zirlo, 54.3 GWd 4.25%/3 cy/12.1 yr 914.4 W	4 6F2 NAIF/P+Z Zirlo, 51.9 GWd 4.25%/3 cy/13.5 yr 799.5 W	Drain Port
5 3F6 NAIF/P+Z Zirlo, 52.1 GWd 4.25%/3 cy/13.5 yr 800.9 W	6 (TC Lance) 30A AMBW M5, 52.0 GWd 4.55%/3 cy/7.2 yr 1008.6 W	7 22B AMBW M5, 51.2 GWd 4.55%/3 cy/5.7 yr 1142.4 W	8 (PRA) 20B AMBW M5, 50.5 GWd 4.55%/3 cy/5.7 yr 1121.2 W	9 5K6 AMBW M5, 53.3 GWd 4.55%/3 cy/8.7 yr 975.1 W	10 5D5 NAIF/P+Z Zirlo, 55.5 GWd 4.20%/3 cy/17.7 yr 814.5 W
11 (Vent Port) 5D9 NAIF/P+Z Zirlo, 54.6 GWd 4.20%/3 cy/17.7 yr 802.6 W	12 28B AMBW M5, 51.0 GWd 4.55%/3 cy/5.7 yr 1135.0 W	13 (PRA) F40 LOPAR Zry-4, 50.6 GWd 3.59%/3 cy/30.6 yr 573.8 W	14 (TC Lance) 57A AMBW M5, 52.2GWd 4.55%/3 cy/7.2 yr 1037.0 W	15 (PRA) 30B AMBW M5, 50.6 GWd 4.55%/3 cy/5.7 yr 1124.8 W	16 3K4 AMBW M5, 51.8 GWd 4.55%/3 cy/8.7 yr 941.3 W
17 5K7 AMBW M5, 53.3 GWd 4.55%/3 cy/8.7 yr 961.7 W	18 (PRA) 50B AMBW M5, 50.9 GWd 4.55%/3 cy/5.7 yr 1131.1 W	19 (TC Lance) 3U9 NAIF/P+Z Zirlo, 53.1 GWd 4.45%/3 cy/10.6 yr 920.2 W	20 (PRA) 0A4 NAIF Low-Sn Zry-4, 50.0 GWd 4.00%/2 cy/23.2 yr 646.2 W	21 15B AMBW M5, 51.0 GWd 4.55%/3 cy/5.7 yr 1135.8 W	22 6K4 AMBW M5, 51.9 GWd 4.55%/3 cy/8.7 yr 941.2 W
23 3T2 NAIF/P+Z Zirlo, 55.1 GWd 4.25%/3 cy/12.1 yr 934.7 W	24 (TC Lance) 3U4 NAIF/P+Z Zirlo, 52.9 GWd 4.45%/3 cy/10.6 yr 914.2 W	25 (PRA) 56B AMBW M5, 51.0 GWd 4.55%/3 cy/5.7 yr 1133.7 W	26 54B AMBW M5, 51.3 GWd 4.55%/3 cy/5.7 yr 1136.3 W	27 6V0 AMBW M5, 53.5 GWd 4.40%/3 cy/8.7 yr 988.2 W	28 (TC Lance) 3U6 NAIF/P+Z Zirlo, 53.0 GWd 4.45%/3 cy/10.6 yr 916.9 W
	29 4V4 AMBW M5, 51.2 GWd 4.40%/3 cy/9.1 yr 914.2 W	30 5K1 AMBW M5, 53.0 GWd 4.55%/3 cy/8.7 yr 968.0 W	31 (TC Lance) 5T9 NAIF/P+Z Zirlo, 54.9 GWd 4.25%/3 cy/12.1 yr 927.7 W	32 4F1 NAIF/P+Z Zirlo, 52.3 GWd 4.25%/3 cy/13.5 yr 804.3 W	

Figure A-3. Loading map.

Decay Heat: Decay heats for each assembly are identified in Figure A-3 and were all rounded to the first decimal. Decay heats were calculated as of November 7, 2017, though loading did not occur until November 14, 2017. Note that the decay heats for assembly 30A in Cell 6 and assembly 5K7 in Cell 17 have been reduced from those calculated by ORNL to account for the 5 sister rods removed from assembly 30A and the 4 sister rods removed from assembly 5K7. Each sister rod was replaced with a stainless-steel rod. Locations of the removed sister rods for each assembly are found in Figure A-4 and Figure A-5. Total decay heat for the cask is 30.456 kW.

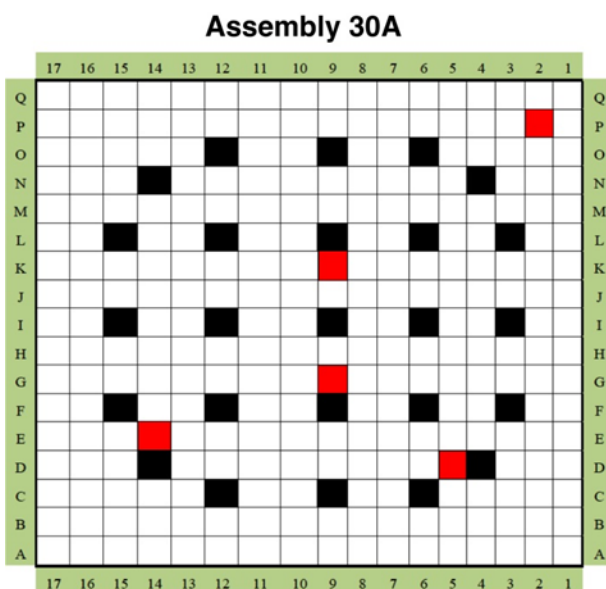


Figure A-4. Sister rods removed from Assembly 30A (in red, guide/instrument tubes in black). Rods replaced with stainless-steel rods.

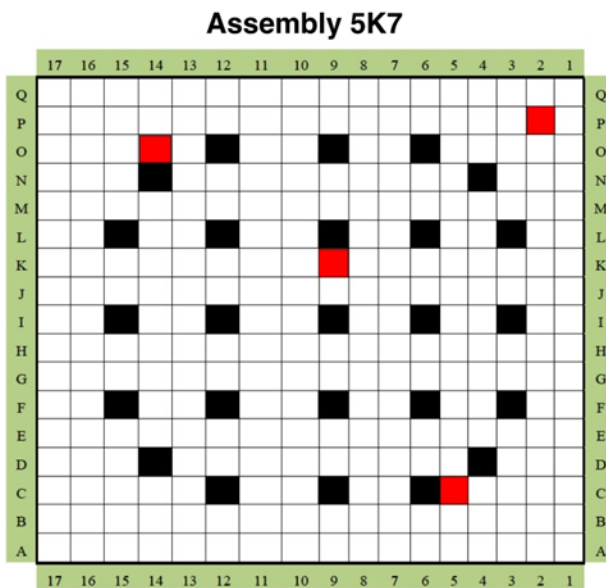


Figure A-5. Sister rods removed from Assembly 5K7 (in red, guide/instrument tubes in black). Rods replaced with stainless-steel rods.

Decay Heat Axial Profiles: ORNL calculated the decay heat on a pin-by-pin basis, each at 32 axial heights. The decay heat at each height was summed to get the assembly decay heat at that height. The axial decay heat for each assembly was then normalized to the highest decay heat for that assembly and all 32 assemblies plotted. The trends and values were very close, so the average normalized decay heat for all 32 assemblies was calculated and plotted. Figure A-6 shows this average normalized axial profile at the 32 axial heights with position 1 near the bottom of the rod and position 32 near the top of the rod. The average normalized values are then given in Table A-1.

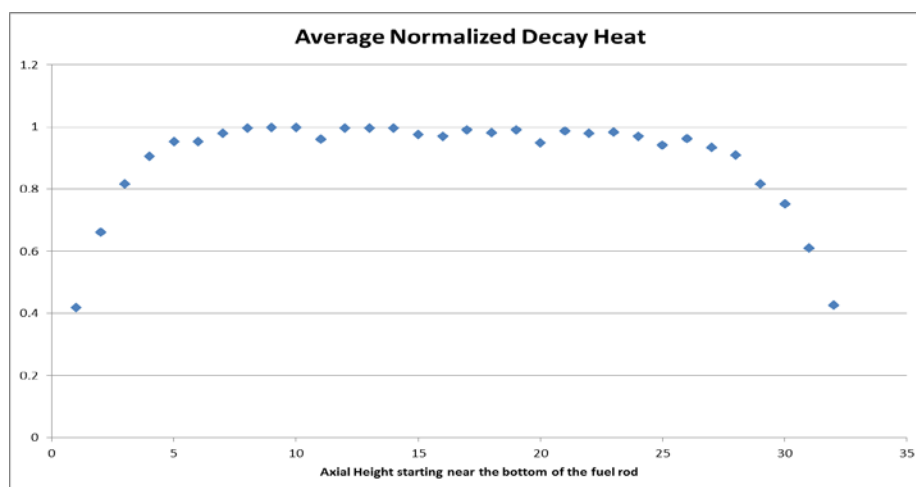


Figure A-6. Average of all 32 assembly normalized decay heats with 1 on the x axis near the bottom of the fuel rod and 32 being near the top of the fuel rod.

Table A-1. Average normalized axial decay heat profile.

Position	Normalized Decay Heat	Position	Normalized Decay Heat
1	0.4189	17	0.9916
2	0.6617	18	0.9823
3	0.8169	19	0.9902
4	0.9051	20	0.9499
5	0.9539	21	0.9869
6	0.9524	22	0.9789
7	0.9800	23	0.9838
8	0.9972	24	0.9706
9	0.9994	25	0.9424
10	0.9985	26	0.9633
11	0.9607	27	0.9340
12	0.9974	28	0.9087
13	0.9972	29	0.8163
14	0.9959	30	0.7522
15	0.9760	31	0.6106
16	0.9707	32	0.4269

For the positions in Table A-1, assume the bottom of the fuel rod is 4.0 inches from the inside surface of the bottom of the cask. Position 1 starts at the bottom of the active fuel portion of the rod, so with the assumption that the end plug is 0.7 inches and the fuel is in contact with the end plug (there is variability between the 4 assembly designs, but not enough to affect the thermal models), Position 1 starts at 4.7 inches above the inside surface of the bottom of the cask. Each of the 32 sections is 4.5 inches in height (144 inches active fuel length/32).

Poison Rod Assemblies: PRAs were inserted in the assemblies in Cells 8, 13, 15, 18, 20, and 25. They can be seen as loaded in the spent fuel pool in Figure A-7. (Materials and dimensions to be provided.)

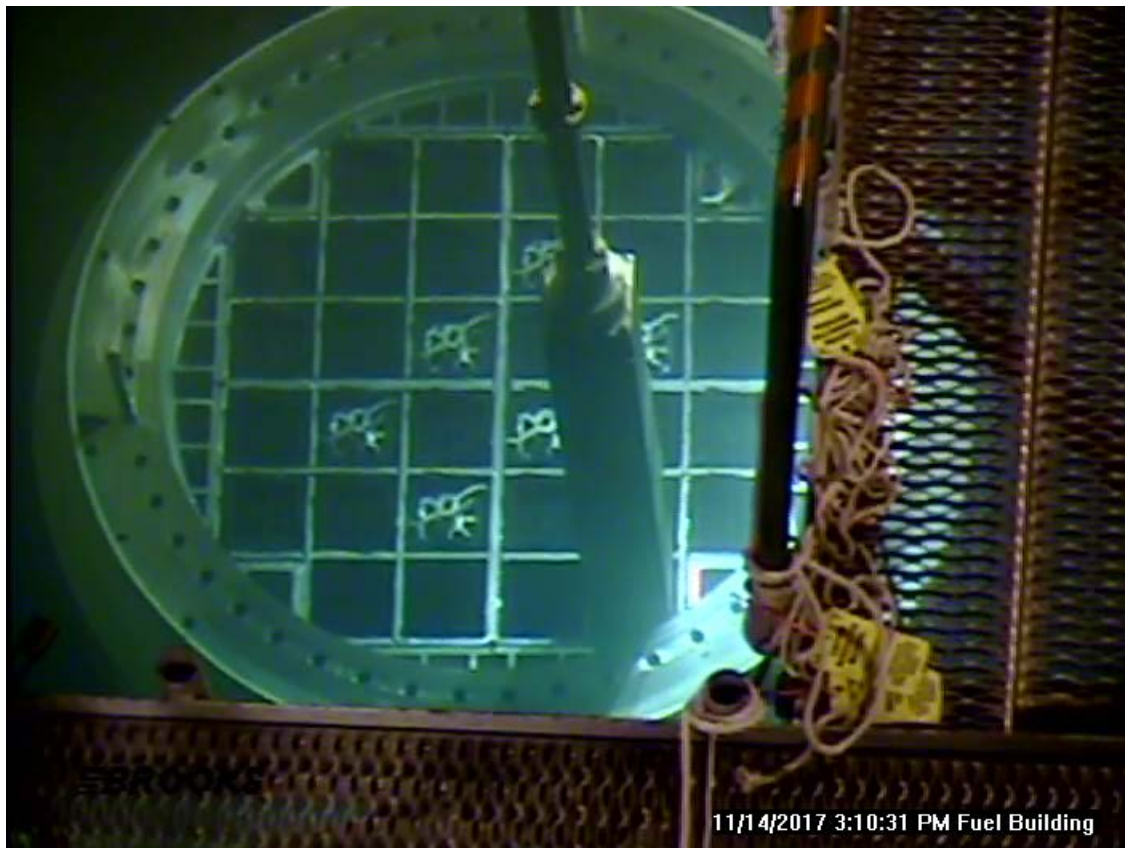


Figure A-7. Location of poison rod assemblies inserted into guide tubes in cells 8, 13, 15, 18, 20, and 23.

Thermocouple Lances: Thermocouple lances were inserted into a guide tube in the assemblies located in cells 2, 6, 14, 19, 24, 28, and 31 as indicated in Figure A-2. The specific guide tube is shown in the map in Figure A-8. Note that the rod with the PCT in the assembly may not be located near the thermocouple, which is why it is important to calculate both PCT and temperatures of the thermocouples in the guide tubes. Each lance has 9 thermocouples axially spaced according to Figure A-9 and Table A-2. The dimensions mean that the lowest thermocouple in each lance is located 9 inches above the bottom of the bottom nozzle (i.e., the inner side of the cask bottom).

TN-32B HBU Cask Thermocouple Map

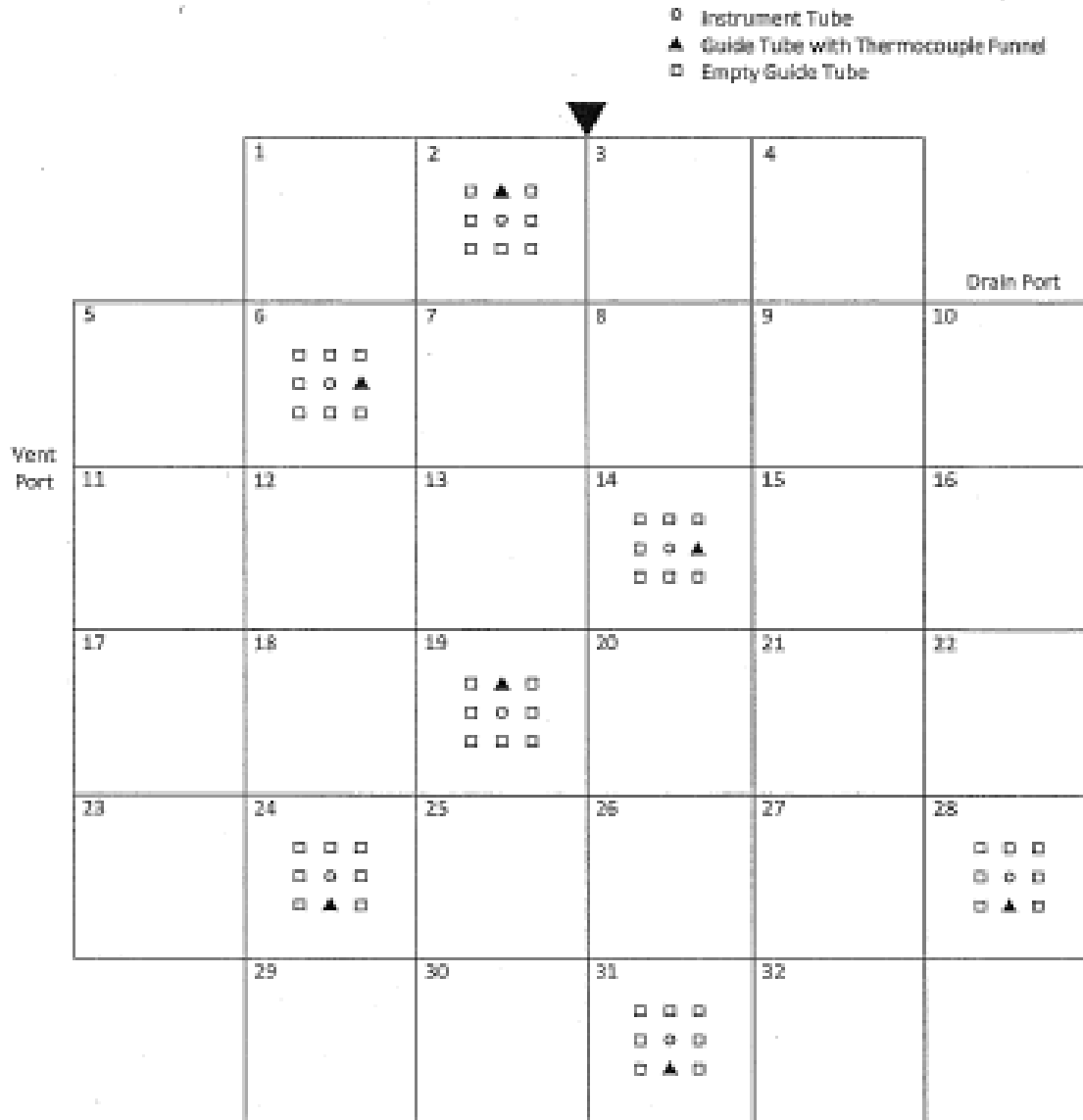


Figure A-8. Location of thermocouple lances (colored triangle) in guide tube.

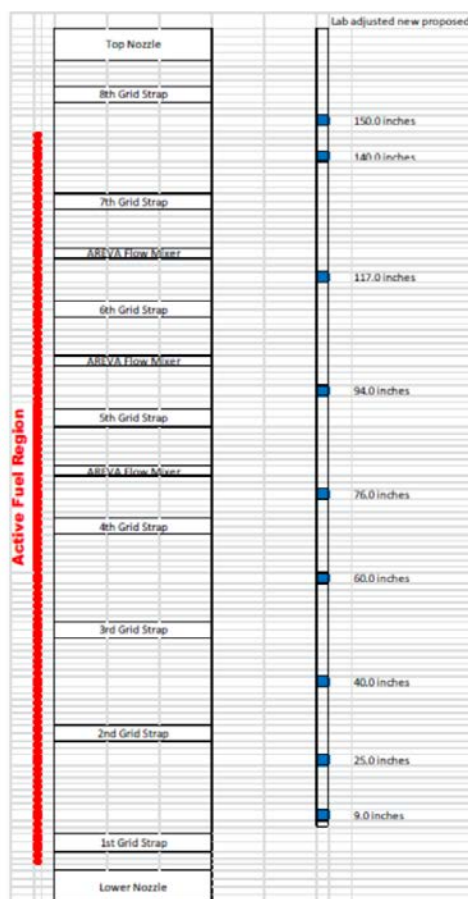


Figure A-9. Axial location of thermocouples in each lance (note that distance is from bottom of the lower nozzle, i.e., from the inner side of the cask bottom).

Table A-2. Thermocouple locations.

Label	Top Down Distance from Flange	Distance from Top of Lid (in.)	Distance from Bottom of Cavity (in.)
TC1	18.25	13.25	150
TC2	28.25	23.25	140
TC3	51.25	46.25	117
TC4	74.25	69.25	94
TC5	92.25	87.25	76
TC6	108.25	103.25	60
TC7	128.25	123.25	40
TC8	143.25	138.25	25
TC9	159.25	154.25	9

Decon Pit Dimensions: Vacuum drying and the thermal soak to get to thermal equilibrium occurred inside the decon pit. The neutron shield for the lid and the protective cover were not in place during this time. A temporary neutron shield ring was in place around the top of the cask (see Figure A-10). In addition, lead blankets were in place on top of the lid to help reduce worker dose.



Figure A-10. Temporary neutron shield ring prior to placement around cask. Note also the large roll-up door leading outside to transfer cask out to pad. The cask and work platform level are behind the camera.

From Figure A-11, it is seen that the work platform (where workers stand to tighten bolts, install the thermocouple lances, hook up for dewatering, blowdown, and vacuum drying, etc.) goes around the cask at about the level of the upper trunnions. This platform was in place prior to the vacuum drying and remained for the entire thermal soak period. The platform does not touch the cask, but the cask is not necessarily centered, and the gaps between the work platform and cask can vary between 0.5 inches and 2 inches.

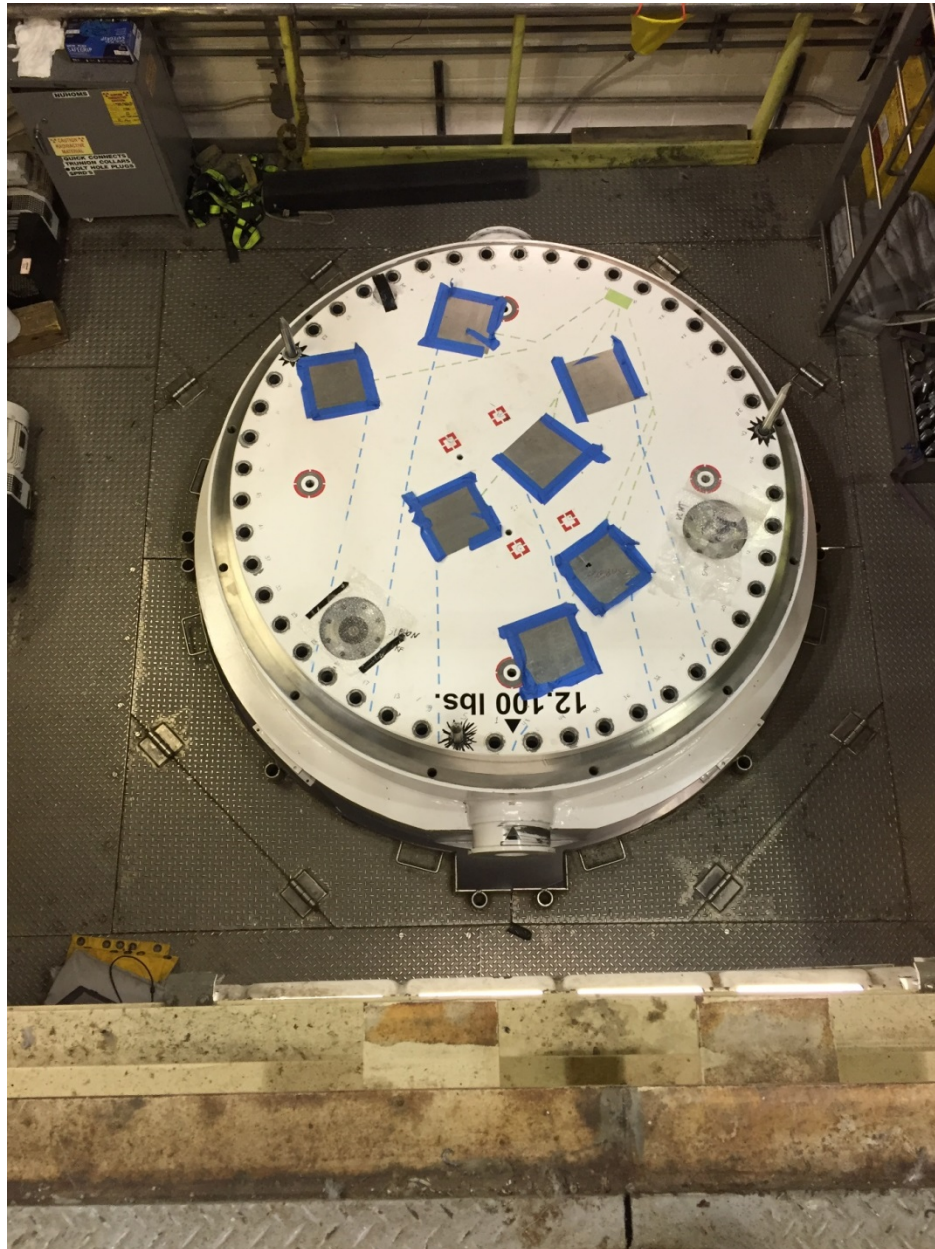


Figure A-11. Looking down on cask to see work platform in place.

From the space below the work platform, you can look up to see the platform in place in Figure A-12. The green markings are where infrared (IR) measurements of the cask surface temperature are taken.



Figure A-12. Looking from below up to work platform.

Figures A-13 and A-14 show the view of the cask (unloaded at this point) in the decontamination pit.



Figure A-13. View of cask in decon pit.

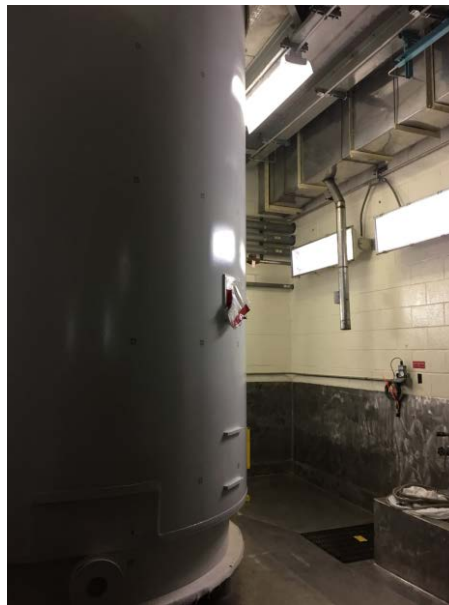


Figure A-14. View of cask in decon pit.

The cask sits on a leveling platform, not on the stainless-steel lined concrete floor, as seen in Figures A-15 and A-16. The leveling pad is approximately 1.5-inch-thick stainless steel with a thin fabric layer between the cask and the pad. The pad has seven total legs or pedestals to support it, one centered and six spaced equidistantly around the edge of the pad. There is approximately 6 inches of air space between the bottom of the leveling pad platform and the stainless-steel lined concrete floor.



Figure A-15. View of cask on leveling pad.



Figure A-16. View of cask on leveling pad.

Approximate dimensions from the cask to walls of the Decon bay are given in Figures A-17 and A-18, first from above the work platform and then below.

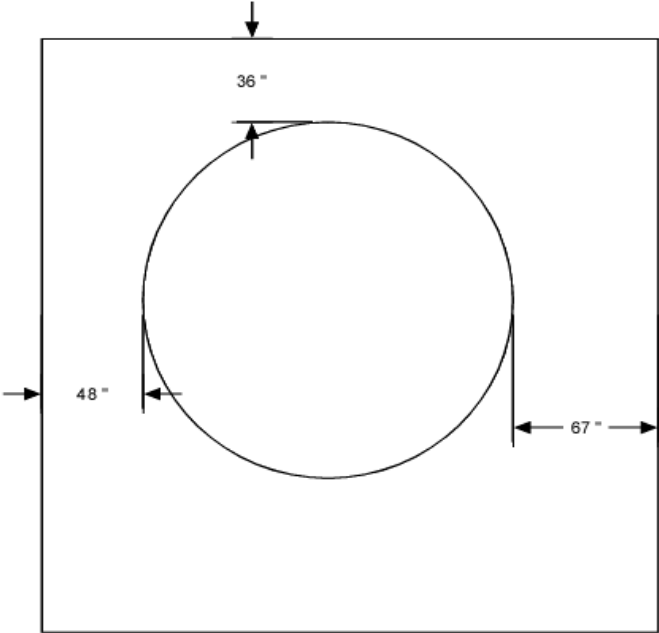


Figure A-17. Dimensions from cask to walls above the work platform.

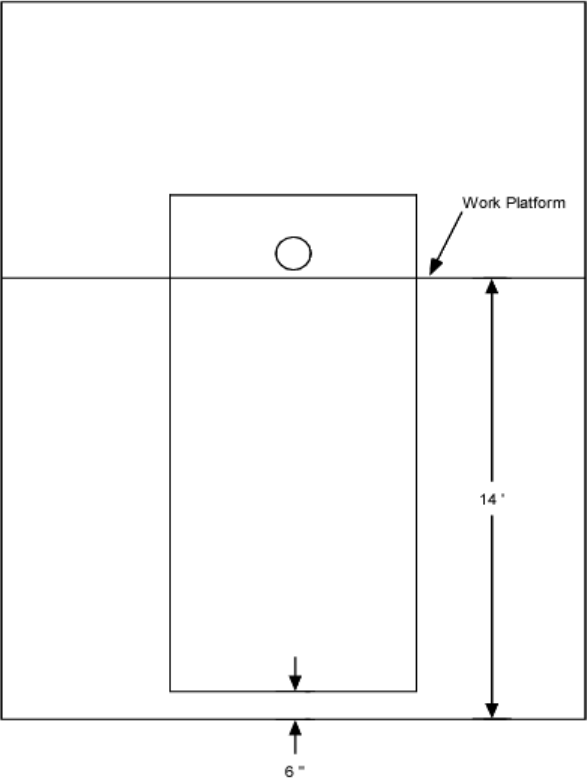


Figure A-18. Approximate dimensions below the work platform.

Ambient Temperature: The ambient temperature has a large effect on component temperatures. With the vacuum drying and thermal soak being performed in the decon pit, there is no contribution from solar insolation. A thermocouple was placed approximately 5 feet up from the bottom of the cask and hanging in air about 3 feet away from the cask, basically to the front and right of the cask in Figure A-18.

Ambient temperature was measured using this thermocouple. Ambient temperatures are also recorded on each of the two data loggers, which were located on a table about 8 feet above the work platform. With two large roll-up doors in the vicinity that lead directly outside and were opened intermittently, no active heating or cooling, and ventilation well controlled, the temperatures inside the decon pit varied with the outdoor temperature as can be seen in Figure A-19.

Corresponding temperature swings in the recorded data with the swings in ambient temperature were not observed, it is clear that the thermal mass of the system greatly dampened the effect of daily temperature variation. It is also clear that the ambient temperature measured by the Ambient TC (3 ft away from cask wall and 5 ft from the cask bottom) was strongly affected by the heat given off by the cask and is not representative of an ambient air temperature when a cask is outside on a pad where such “feedback” does not occur.

It is suggested that constant ambient temperatures of (60°F) (above the work platform, i.e., above the trunnions and for the lid) and (65°F) (below the work platform, i.e., the bulk of the cask) be used for modeling purposes for the steady state calculation for vacuum drying (started shortly after midnight the morning on 11/16/17). For the steady state temperature calculations at the end of the thermal soak, it was agreed to use constant ambient temperatures of (60°F) above the work platform and (75°F) below the work platform.

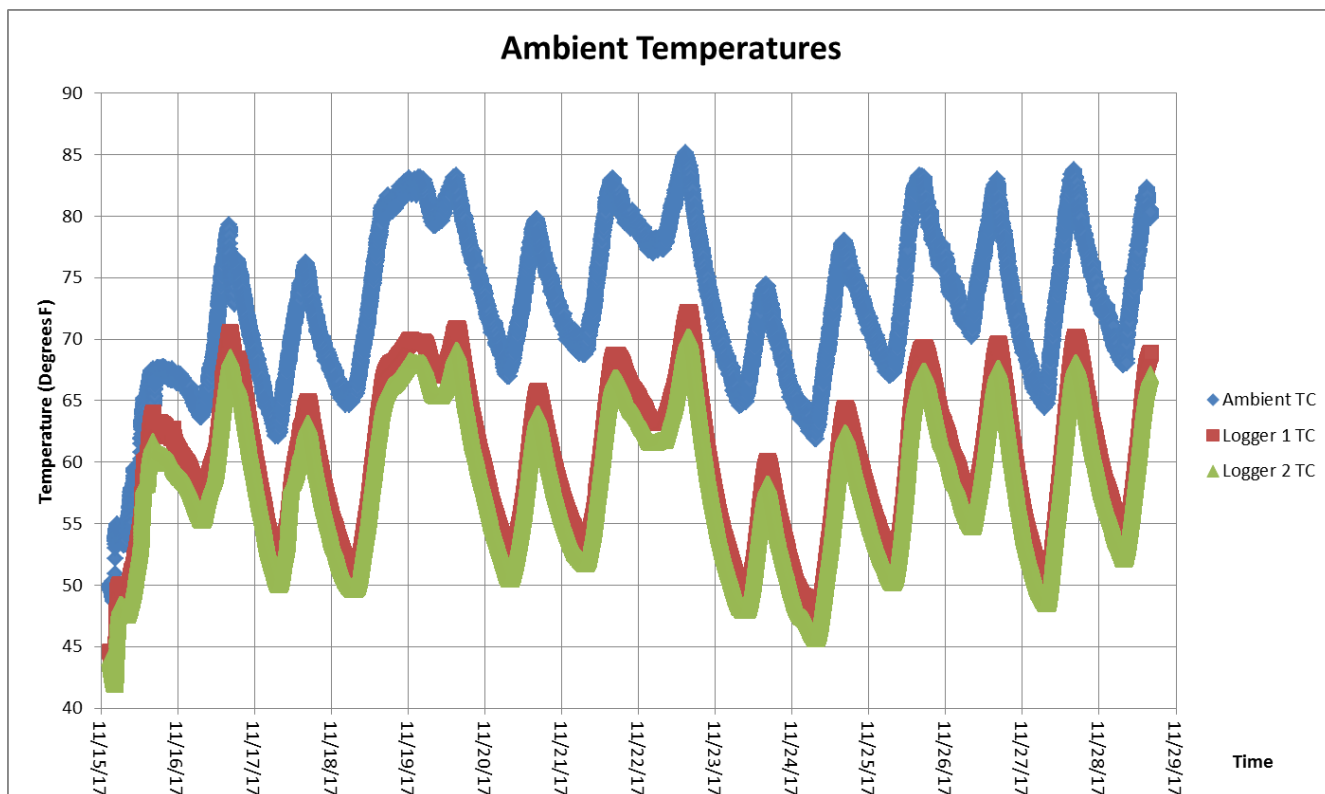


Figure A-19. Ambient temperature in the decontamination pit.

Cask Internal Pressure: The cask was backfilled with 99.999% Ultrapure He to 2200 mbar. While there were some variations between 2100 and 2300 mbar (first due to a leaking connection on the pressure gauge as well as the taking of gas samples, then a pressure increase as the internal temperatures increased, which resulted in the cask being vented on 11/20/2017 to keep the pressure within technical specifications), for the purposes of this modeling exercise, a constant absolute pressure of 2200 mbar should be used. Note that the final pressure reading on 11/28/2017, prior to everything being disconnected to move the cask out to the ISFSI, was 2330 mbar.

External Cask Wall Temperatures: For Task 2d, the temperatures at the locations shown in Figure A-20 will be provided to serve as the boundary condition. If possible, for Task 2c, temperatures at these locations should be calculated.

Lead Blankets on Cask Lid: Lead blankets, as shown in Figure A-21, were used on the lid to cut down on worker dose. They were in place for the vacuum drying and for the entire thermal soak period, though there may have been some minor movement of them during that time.

The blankets were supplied by Nuclear Power Outfitters. The Inner Material is lead wool and the outer material is Alpha Maritex (a fibrous glass coated with silicone) with two layers of Alpha Maritex (inner and outer). The weight is 30 lb/sf. The area is 1.84 sf and total weight is 55.2 lb. From Figure A-22, an OD of 80 in, an inside diameter of 48.5 in, and an angle of arc of 30 degrees was calculated. The dimensions, area, and weight were calculated from scaling a picture and are reasonable estimations but are not exact.

Attachment 1 - Test Cask Exterior Temperature Monitoring Locations

Symbols:
⊕ Exterior Temperature Monitoring Locations
○ Zero Degree (0°) Trunnions, Upper & Lower

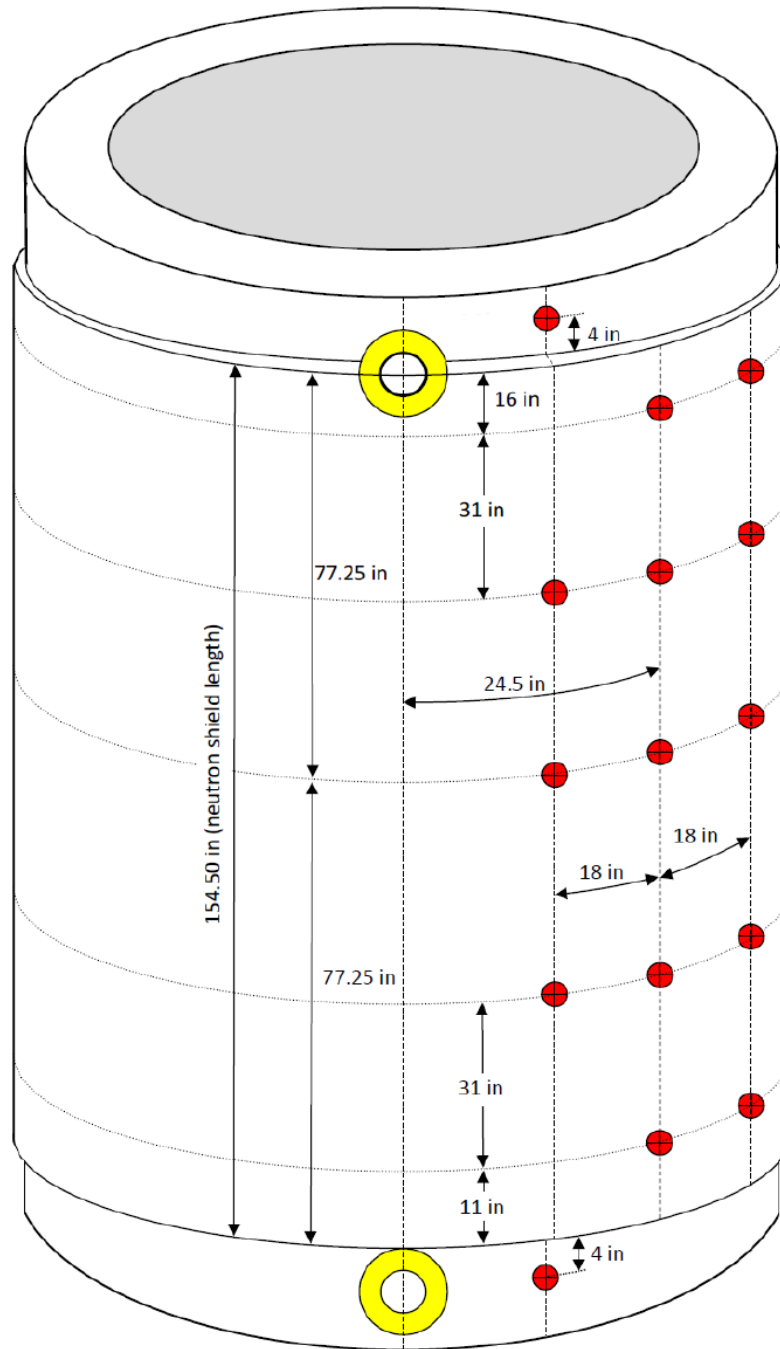


Figure A-20. Location of cask wall IR measurements.



Figure A-21. Lead blankets and temporary neutron shield ring in place.

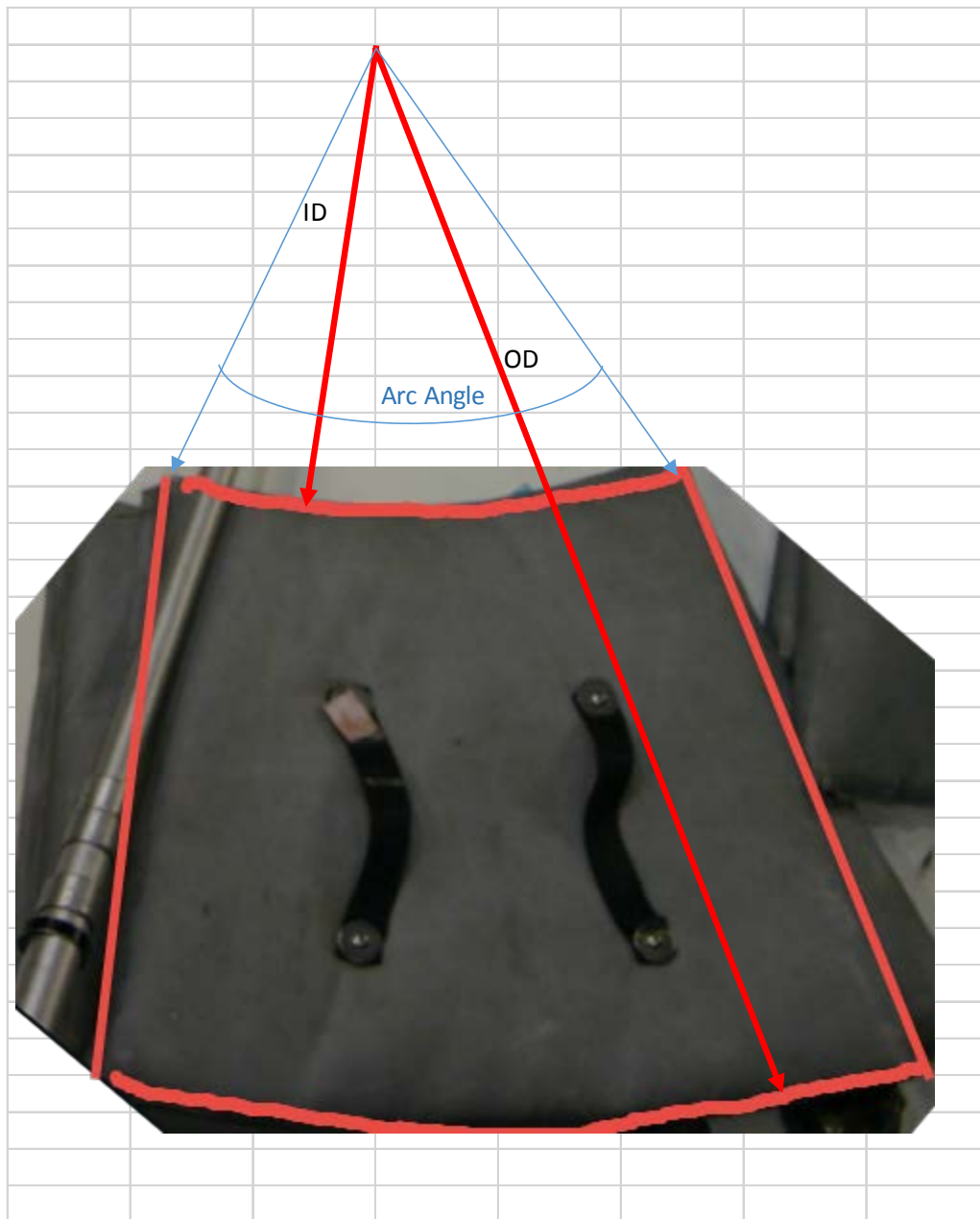


Figure A-22. Dimensions of lead blanket.

Appendix B

COMPARISONS OF BLIND MODEL PREDICTIONS WITH MEASUREMENTS AT THERMOCOUPLE POSITIONS

This page is intentionally left blank.

This appendix contains comparisons of blind model predictions with measurements at the thermocouple positions. Each plot is labeled with the basket cell number, which is defined in Figure B-1, and the assembly identification number, which is defined in Figure B-2.

	1	2	3	4	
5	6	7	8	9	10
11	12	13	14	15	16
17	18	19	20	21	22
23	24	25	26	27	28
	29	30	31	32	

Figure B-1. Basket cell numbers (orange cells denote assemblies with thermocouple lances).

	6T0	3K7	3T6	6F2	
3F6	30A	22B	20B	5K6	5D5
5D9	28B	F40	57A	30B	3K4
5K7	50B	3U9	0A4	15B	6K4
3T2	3U4	56B	54B	6V0	3U6
	4V4	5K1	5T9	4F1	

Figure B-2. Assembly identification numbers.

Blind model predictions for temperatures at thermocouple locations are compared with measured values in Figures B-3 through B-9. The model results are computed using the measured surface temperatures as the boundary condition on the outer circumference of the cask. This case is discussed in Section 5.2.2 of the report.

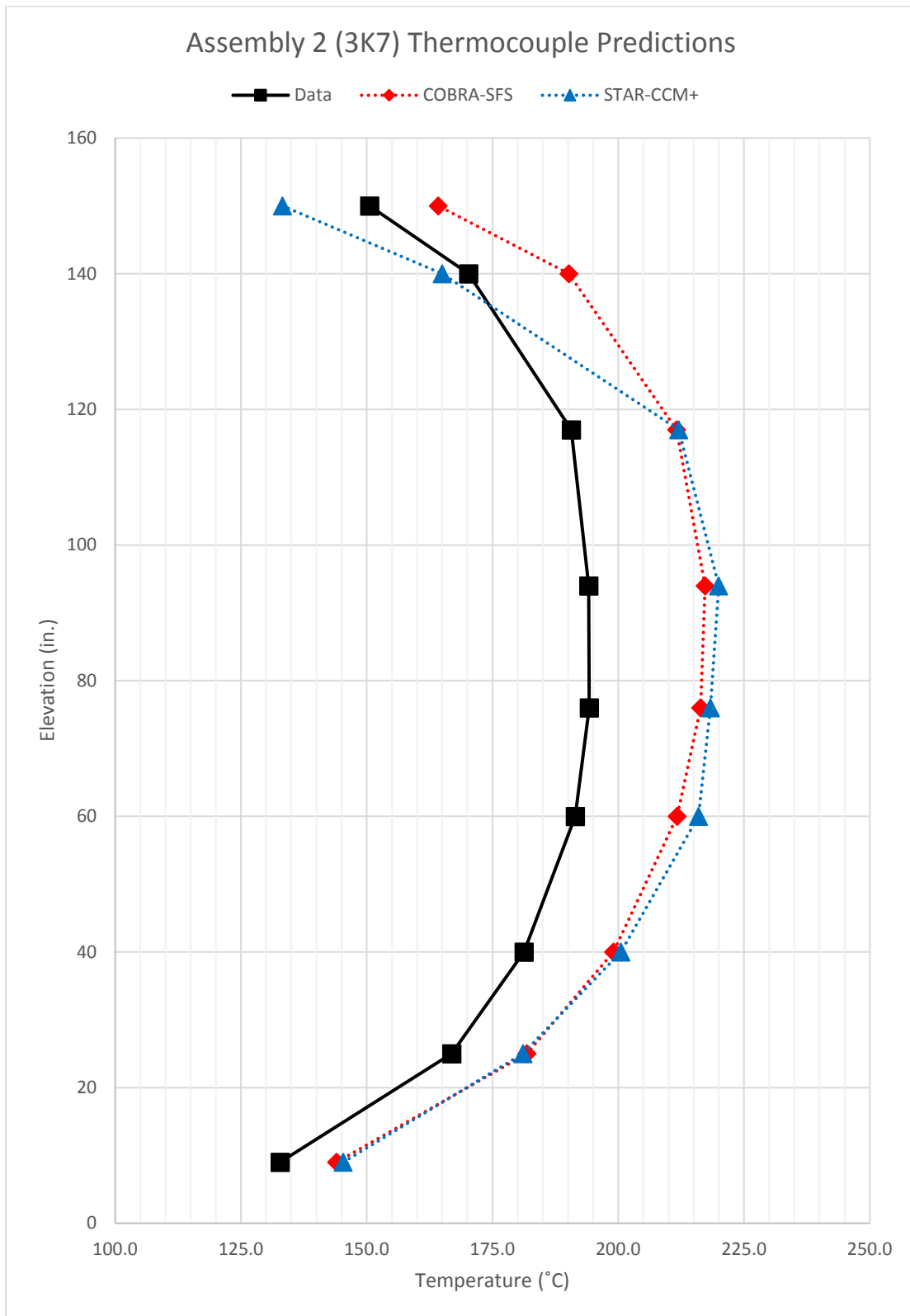


Figure B-3. Comparison of measured and predicted temperatures – Cell 2 (Assembly 3K7).

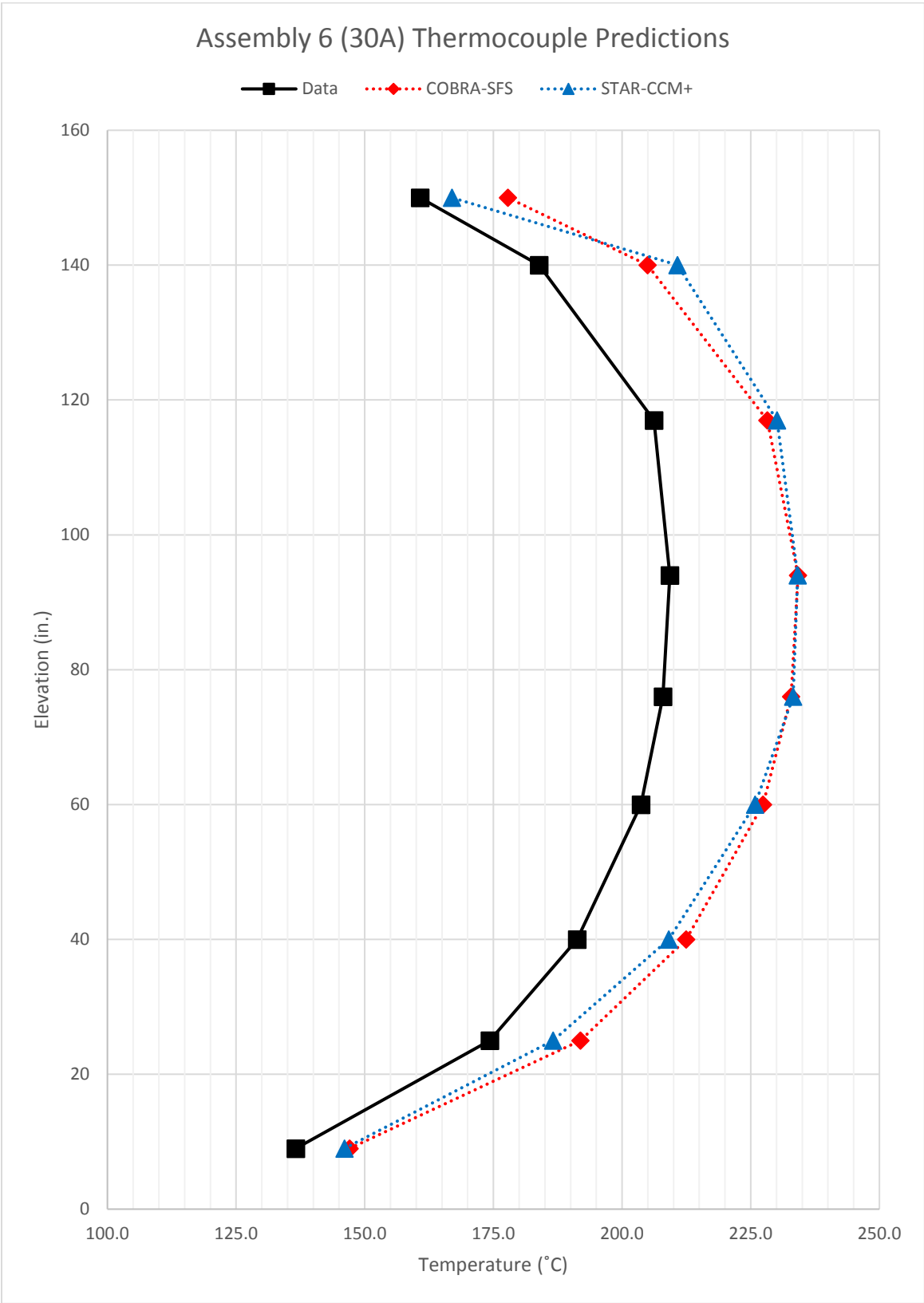


Figure B-4. Comparison of measured and predicted temperatures – Cell 6 (Assembly 30A).

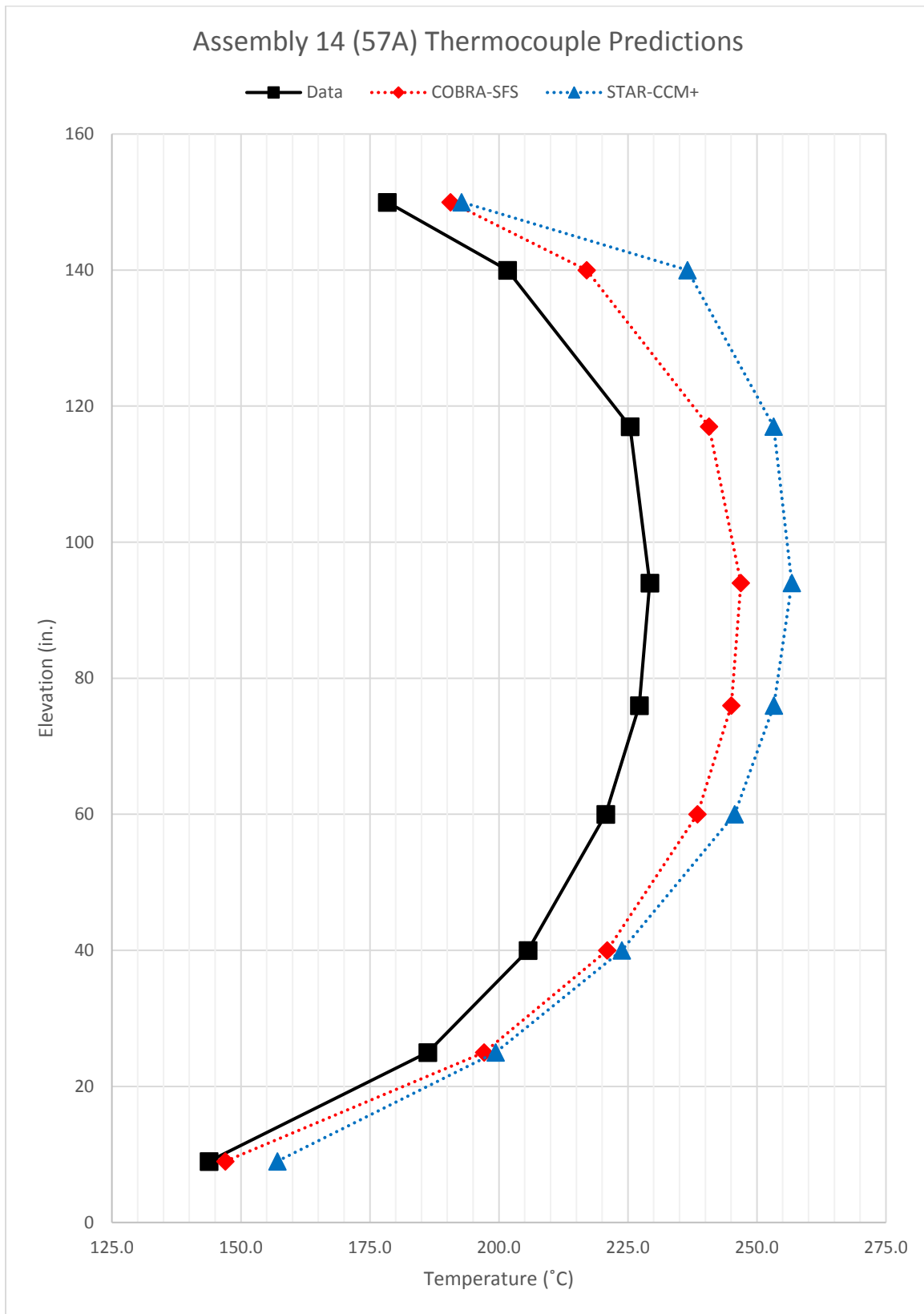


Figure B-5. Comparison of measured and predicted temperatures – Cell 14 (Assembly 57A).

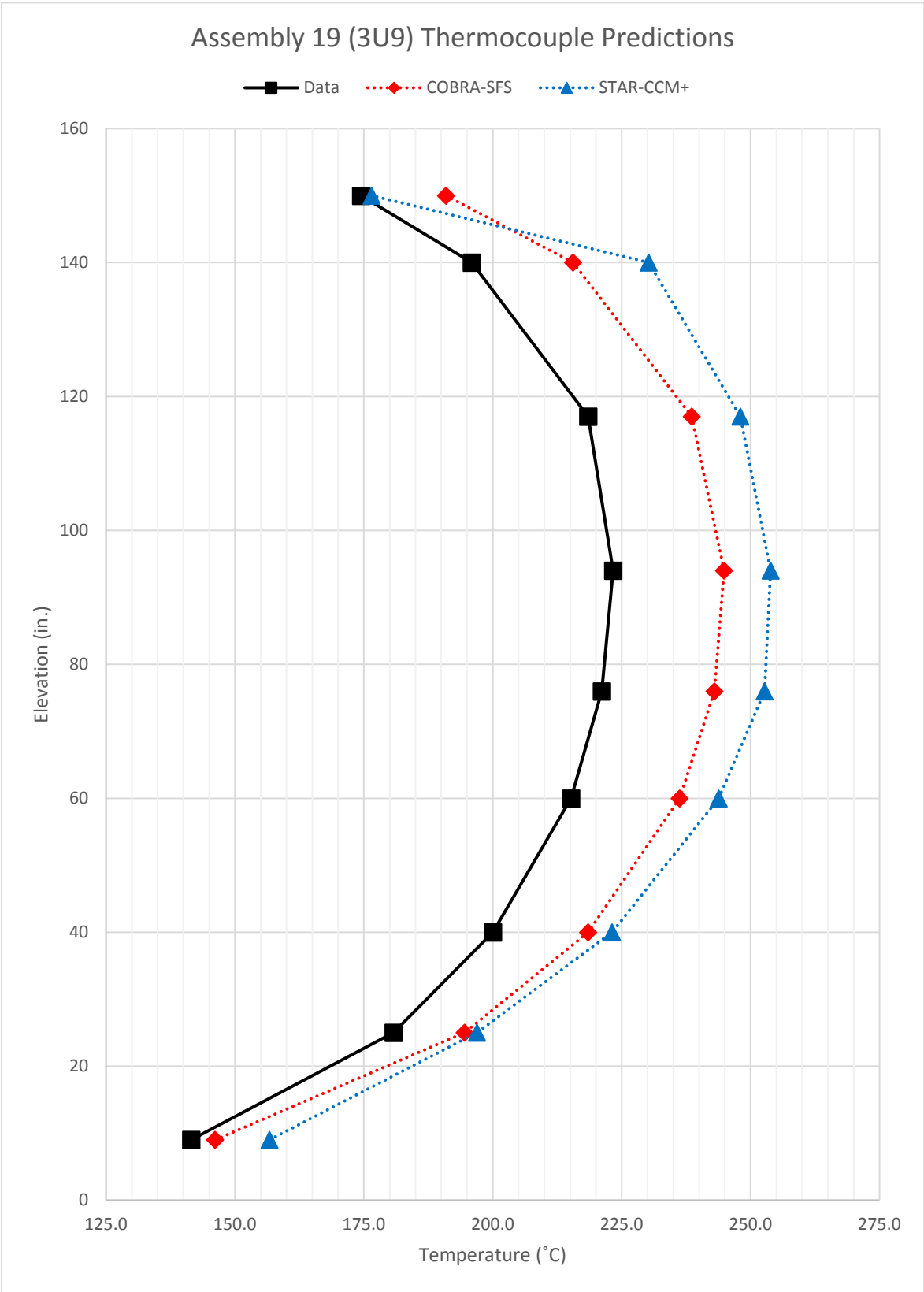


Figure B-6. Comparison of measured and predicted temperatures – Cell 19 (Assembly 3U9).

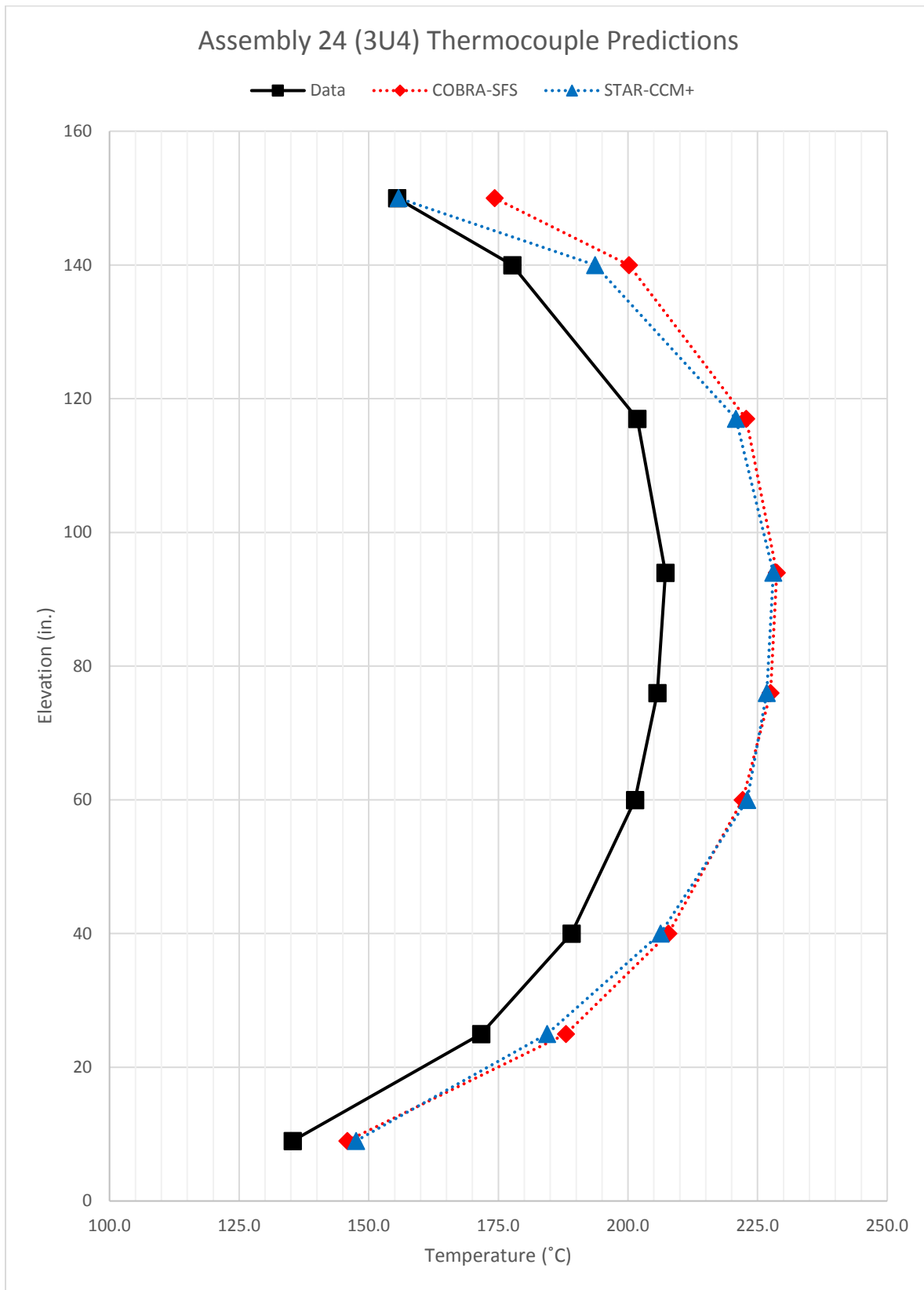


Figure B-7. Comparison of measured and predicted temperatures – Cell 24 (Assembly 3U4).

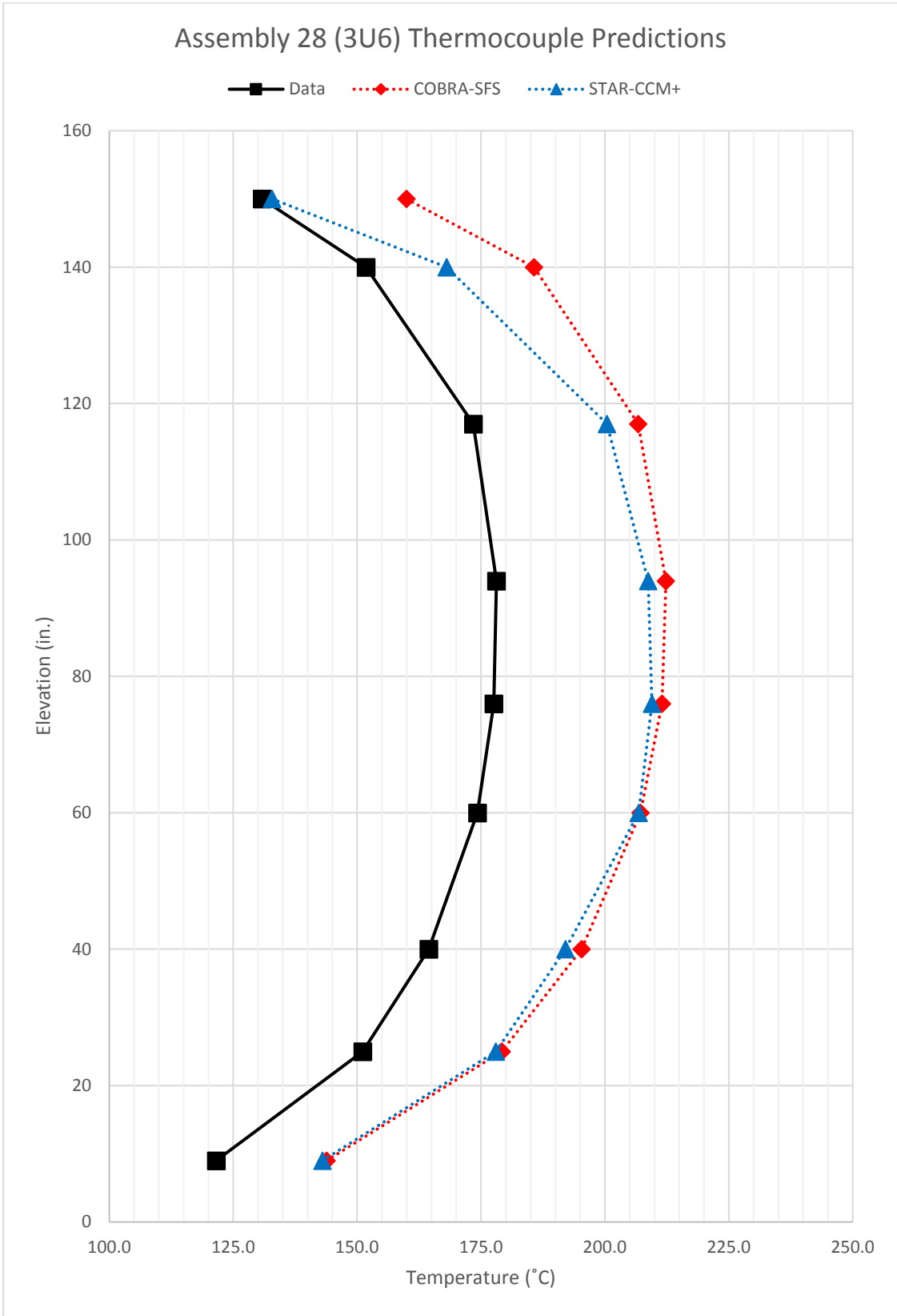


Figure B-8. Comparison of measured and predicted temperatures – Cell 28 (Assembly 3U6).

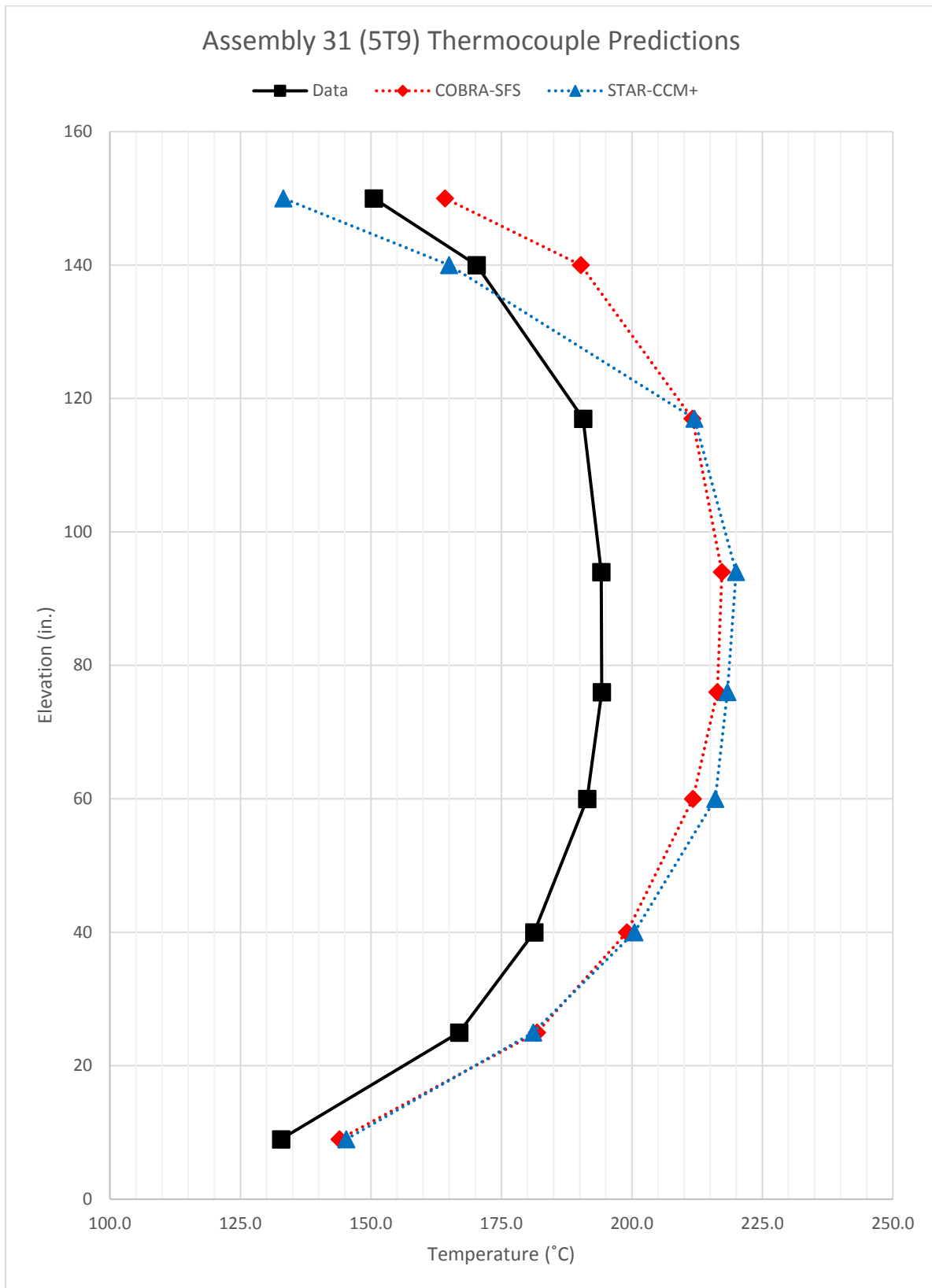


Figure B-9. Comparison of measured and predicted temperatures – Cell 31 (Assembly 5T9).